# Computer Simulations of
# Nonlinear Wave Instabilities
# Driven by Ion Temperature Anisotropy
# in Space Plasmas

Masafumi SHOJI

# Acknowledgments

# Abstract

As one of the important phenomena in the space plasmas, instabilities driven by the temperature anisotropy of ions take place. For example, the ions are heated in the perpendicular direction to the ambient magnetic field due to the adiabatic heating in the downstream of the quasi-perpendicular shock. In the inner magnetosphere, there exists the inward transportation of the energetic plasmas due to the magnetic reconnections in the magnetotail. These phenomena form anisotropic velocity distribution functions of the ions in each region. The ion temperature anisotropy in the perpendicular direction drives mirror and electromagnetic ion cyclotron (EMIC) instabilities through the wave particle interactions. The mirror mode structures and the L-mode EMIC waves, which are excited through these instabilities, have large amplitude and scale size and thus they play a significant role for the energy transportations in the different parts of the geospace plasmas. We analyzed the nonlinear evolutions of these waves and interactions with the ions in the Earth's magnetosheath and the inner magnetosphere using the hybrid simulations which treat ions and electrons as particles and fluid, respectively.

The solar winds move through the bowshock, the proton temperature anisotropy causing the mirror and EMIC instabilities arises. Spacecraft observations show that the mirror instability dominates over the L-mode EMIC instability in the magnetosheath, although the theoretical linear EMIC growth rate is higher than that of the mirror mode waves. We performed two- and three-dimensional (2D and 3D) hybrid simulations with the periodic boundary to understand the competing process between the EMIC and mirror instabilities. In the 2D model, the energy of the EMIC waves is higher at the growth phase because of its higher growth rate. In the 3D model, however, the energy of the mirror mode waves is larger than that of the EMIC waves for all times because the wavenumber spectra of mirror mode waves form torus-like structures. As the mirror mode waves relax the temperature anisotropy effectively, the linear growth rates of the EMIC waves become smaller before saturation. The EMIC waves cause heating of protons trapped by the nonlinear potentials due to coexistence of forward and backward propagating waves. They terminate the growth of EMIC waves. Because of the heating, the temperature anisotropy decreases to the threshold of the mirror instability and thus the mirror mode wave saturates. At the nonlinear stage, coalescence of the mirror mode structures takes place in both models. The quick dissipation of the EMIC waves occurs due to the heating by the nonlinear processes. On the other hand, the coalescence is a much slower process than the nonlinear processes of EMIC waves, and thus the mirror mode waves remain.

We also performed 2D and 3D hybrid simulations in open boundary models. In the open systems, because of the propagation of EMIC waves, we obtain the clearer non-

propagating mirror mode structures. We analyzed the relation between the mirror instability and the magnetic peaks and dips observed in the magnetosheath. In the 2D model with low beta ($\beta_\parallel \lesssim 1$), we obtain fine structures of the magnetic dips at the nonlinear stage. In the 3D model, on the other hand, the mirror instability makes the magnetic peaks with the same parameters. The parametric analysis indicates that the magnetic peaks also arise in both 2D and 3D high beta cases ($\beta_\parallel \gtrsim 1$) as shown by the Cluster observations. In the high beta cases, the high mobility of the protons helps continuous coalescence of the diamagnetic currents inside the magnetic dips. The coalescence makes the magnetic dips larger and shallower. Between the large and shallow magnetic dips, the magnetic peaks appear in the high beta cases. In the 3D models, because degree of freedom increases in the perpendicular direction, the continuous coalescence can take place even in the low beta cases. Thus, the magnetic peaks appear in the 3D models in both cases.

In the Earth's inner magnetosphere, due to the inward transportation, the EMIC waves are driven. They cause the different nonlinear wave particle interactions because of the existence of the Earth's eigen dipole magnetic field. In a recent observation by the Cluster spacecraft, EMIC triggered emissions were discovered in the inner magnetosphere. We further modified the hybrid code to incorporate a cylindrical geometry of magnetic field modeling the inner magnetosphere to reproduce the EMIC triggered emissions and analyze the nonlinear wave particle interactions. We assume a parabolic magnetic field to model the dipole magnetic field in the equatorial region of the inner magnetosphere. We reproduce rising tone emissions in the simulation space, finding a good agreement with the nonlinear wave growth theory. In the energetic proton velocity distribution we find formation of a proton hole, which is assumed in the theory. A substantial amount of the energetic protons are scattered into the loss cone, while some of the resonant protons are accelerated to higher pitch angles, forming a pancake velocity distribution.

Another type of EMIC wave with a constant frequency is occasionally observed below the He$^+$ cyclotron frequency after the multiple EMIC triggered emissions. In the presence of energetic protons with a sufficient density and temperature anisotropy, multiple EMIC triggered emissions are reproduced due to the nonlinear wave growth mechanism of rising-tone chorus emissions, and a constant frequency wave in the He$^+$ EMIC branch is subsequently generated. Through interaction with the multiple EMIC rising-tone emissions, the velocity distribution function of the energetic protons is strongly modified. Because of the pitch angle scattering of the protons, the gradient of the distribution in velocity phase space is enhanced along the diffusion curve of the He$^+$ branch wave, resulting in the linear growth of the EMIC wave in the He$^+$ branch.

# Contents

# List of Figures

# List of Tables

# Chapter 1

# General Introduction

## 1.1 Introduction and Overview of Macroscopic Electromagnetic Environment Surrounding the Earth

For the development of the human activity in space around the Earth in the near future, we must understand the electromagnetic environment surrounding the Earth. The space is filled with the ionized gases which are called "plasmas". The name "plasma" is firstly used by *Langmuir* [1928] to describe the ionized gas which consists of electrons and ions. The Earth has a dipole magnetic field, and it is always exposed to the solar wind, which consists of the plasmas and comes from the sun. Inside the sun, nuclear fusions take place and the temperature of the surface becomes high ($\sim$ 6000 K). The atmosphere of the sun, called "corona", has much higher temperature ($\sim$ 1 million K) than the surface. Since the corona is not in hydrostatic equilibrium, there exists steady flow named "solar wind" toward the space. The typical averaged density of the solar wind is around a few /cc. The solar wind plasma mostly consists of the electrons (e$^-$), protons (H$^+$) and a few % of the alpha particles (He$^{++}$). The usual speed of the solar wind near the Earth is $\sim$ 400 - 500 km/s, which is larger than the acoustic speed (a few tens km/s). Thus, the solar wind is the supersonic flow. It is also well known that the solar winds flow with the magnetic field of the sun (Interplanetary Magnetic Field, IMF). *Parker* [1958] has predicted the shape of the solar wind, which forms a spiral structure (Parker spiral). This spiral structures are observed and statistically investigated by *Wilcox and Ness*, [1965]. Because the solar wind forms Parker spiral, around the Earth, the IMF has the angle $\sim$ 45° with the direction toward the sun from the Earth. The IMF and the solar wind plasma pressure modify the shape of the Earth's dipole magnetic field.

Due to the interactions between the solar wind and the Earth's dipole magnetic field, the electromagnetic environment so-called "magnetosphere" [*Gold*, 1959] is deformed around the Earth. Figure 1.1 shows the schematic illustration of the Earth's magne-

tosphere and surrounding electromagnetic environment by *Eastman and Frank* [1984]. In Figure 1.1, the supersonic solar winds come from the left side and expand the Earth's magnetic field far from the Earth in anti-sunward directions. The magnetosphere is the region above the ionosphere where the magnetic field of the Earth extend out to a distance $\sim 10 R_E$, where $R_E$ is the Earth's radius. The magnetosphere consists of various regions characterized by different plasma and magnetic field parameters. Especially, in the present thesis, we focus on the following two regions called "magnetosheath" and "inner magnetosphere". In each region, the temperature anisotropies of the ions in the perpendicular direction to the ambient magnetic field are observed.
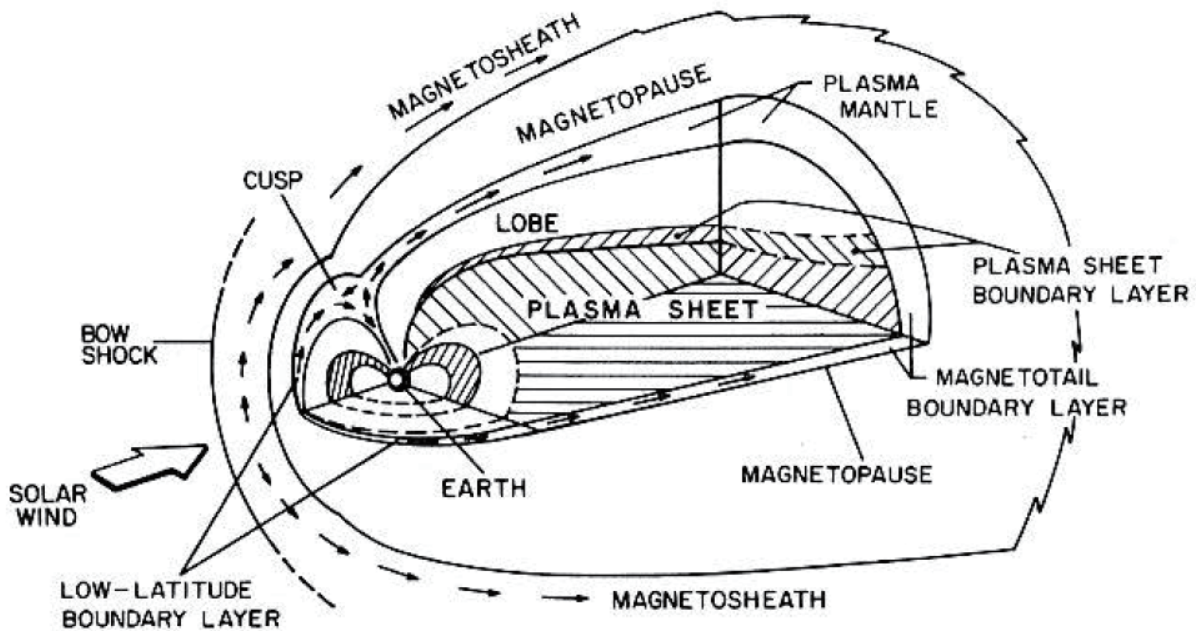


Figure 1.1: Schematic illustration of the Earth's magnetosphere [*after Eastman and Frank, 1984*]

## 1.1.1   Bowshock and magnetosheath

Because the Earth's dipole magnetic field works as a magnetic obstacle for the supersonic solar wind, the shock structure called "bowshock" are generated in the dayside of the Earth. Schematic illustration of the detailed magnetic structures around the dayside of the Earth is shown in Figure 1.2 [*Tsurutani et al.,* 1981]. As shown in Figures 1.1 and 1.2, between the bowshock and the Earth's magnetopause which are the boundary of the Earth's magnetic field, there exists the region called "magnetosheath". Inside the

magnetosheath, Because of the average spiral configuration of the IMF and the effect of solar wind convection, the upstream particle region has a strong local time asymmetry as shown in Figure 1.2, with the majority effect on the dawnside. This region of space upstream of the bow shock has been called the foreshock. In the magnetosheath, the plasmas in the solar wind becomes subsonic (the typical bulk velocity becomes $\sim 250$ km/s). The bowshock are mainly separated into "quasi-parallel" shock, where the angle between IMFs and the shock normal vector is less than 45°, and "quasi-perpendicular" shock where the angle between IMFs and the shock normal vector is larger than 45°. Generally, the solar wind plasmas are heated at the shock front. In the downstream of the quasi-perpendicular shock, which is the fast shock, the ions in the solar wind are strongly heated into the perpendicular to the background magnetic field.

## 1.1.2 Earth's inner magnetosphere

The region where the Earth's dipole magnetic field affects dominantly is called inner magnetosphere. These particles are trapped by the Earth's dipole magnetic field, which works as a mirror devise. When the solar activity is high, Coronal Mass Ejections (CMEs), which are the plasmoid with closed magnetic field from the solar corona, take place. They have higher speed than the solar wind. The CMEs with the southward magnetic field result in the magnetic storm, when they arrive at the Earth. During the magnetic storms in the inner magnetsphere, it is known that the intensity of the Earth's magnetic field becomes significantly smaller due to the diamagnetic currents which appear surrounding the Earth in the inner magnetosphere. The diamagnetic current is called "ring current". At the same time, "the radiation belt" (also called Van Allen belt), which consists of the relativistic electrons and the energetic ions, is constructed in the inner magnetosphere. Because of the existence of these high energized plasmas, the spacecrafts and their devices will be damaged. These particles in the radiation belt come from the solar wind. From the nightside of the Earth, in the magnetotail region, the high energy plasmas are transported inside the inner magnetosphere. Because of the continuous injections, the radiation belt always exists although the magnetic storm stops.

In the inner magnetosphere, there also exists "plasmasphere" around the same region as the radiation belt. In the plasmasphere, the low energy ($\sim 1$ eV) plasmas exist. The boundary of the plasmasphere, called plasmapause, can be identified by the sharp spatial structure of the decreasing plasma density [*Chappell et al.,* 1970]. The plasmapause moves due to the change of the geomagnetic disturbance. The typical distance of the plasmapause from the Earth is $\sim 4$ - $5$ $R_E$.

The loss of the ring currents generated by the magnetic storm cause the aurora in the
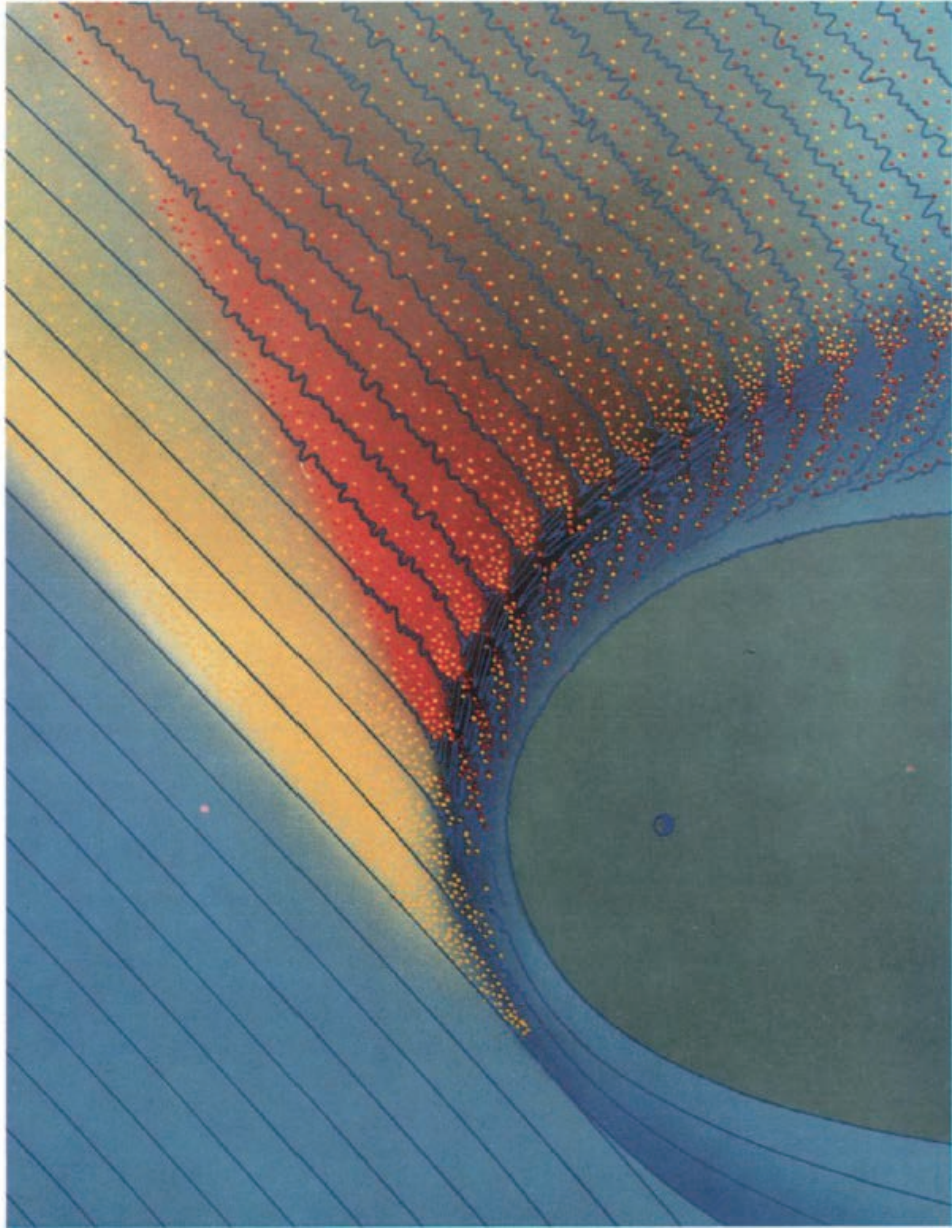
Figure 1.2: Schematic illustrations of the bowshock, magnetosheath, magnetosphere, and interplanetary magnetic fields (IMF). [*after Tsurutani et al.*, 1981]

polar regions. Some parts of the mechanism of the loss of the particles are due to the wave particle interactions. The pitch angle of the particle with the velocity $V = (V_\parallel, V_\perp)$: $\alpha = \tan^{-1}(V_\perp/V_\parallel)$ are scattered by the waves. The scattered particles become to have smaller perpendicular and larger parallel velocities. Some of them become not to be trapped by the Earth's magnetic field, resulting in the aurora around the polar regions.

## 1.2 Instabilities and Waves in Space Plasmas

### 1.2.1 Plasma waves in the magnetosheath and inner magnetosphere

Because the mean free pass of the plasma in the solar wind is $\sim 1$ Au, which is the distance between the sun and the Earth, the space plasmas can be treated as collisionless. Their kinetic energies are exchanged through interaction with the electrostatic or electromagnetic plasma waves. The characteristics of the plasma waves are different in vacuum. The waves become dispersive in the space due to the plasmas. Dispersion relations various electrostatic and electromagnetic waves, which are naturally generated in the plasmas, have been investigated [*Stix*, 1992]. On the other hand, the collisionless plasmas can generate the plasma waves through instabilities. Exchanging their kinetic energy with the waves, the unstable plasma distributions become marginal stable. Therefore, understanding the plasma wave activity directly link to the change of the plasma environment in the space.

Around the Earth's magnetosphere, we can observe many kinds of plasma waves. For example, in the foreshock region (upstream of the bowshock region), the Electrostatic Solitary Waves (ESW), which are seen as Broadband Electrostatic Noises (BEN) in the dynamic spectra, are observed by GEOTAIL spacecraft [*Matsumoto et al.*, 1994]. They are caused by the cold electron beams in the thermal plasmas. In the downstream region of the quasi-perpendicular shock, the spacecrafts, ISEE 1 and ISEE 2, have observed non-oscillatory magnetic field structures as shown in Figure 1.3 [*Tsurutani et al.,* 1982]. These quasi-periodic ($\sim 20$ s) magnetic structures are called mirror mode waves or mirror mode structures as shown in this Figure. The magnetic field angles $\theta$ and $\phi$ show little variation. The mirror mode waves are generated through the mirror instability by the ion temperature anisotropy as we discuss in later section.

In the inner magnetosphere, there exist some electromagnetic waves which affect to the configuration of the geospace plasmas. Figure 1.4 shows the spatial distribution of important waves in the inner magnetosphere [*Thorne*, 2010]. The trajectory of the ring current electrons and ions are also shown by dashed arrow. The whistler-mode chorus
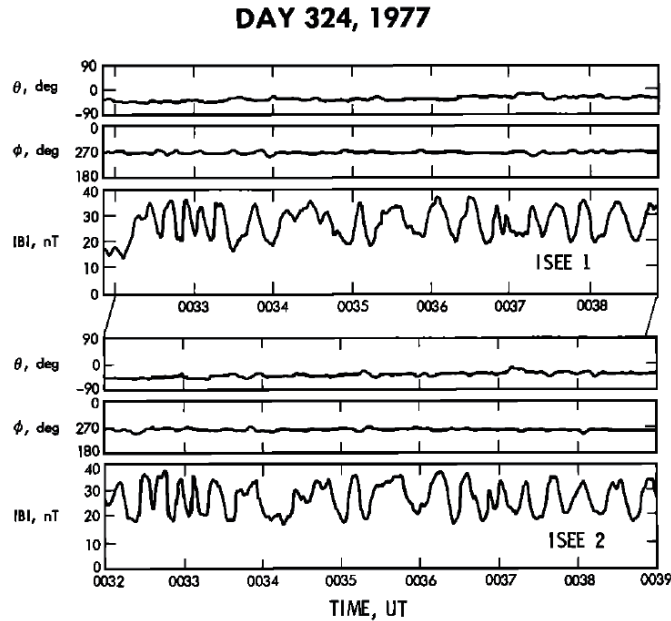
**DAY 324, 1977**



Figure 1.3: Magnetic field data by ISEE 1 (top panel) and ISEE 2 (bottom panel) for day 324, 1977. The magnetic field angles $\theta$ and $\phi$, and the amplitude $|B|$ are shown in each panel. [*after Tsurutani et al.,* 1982]

emissions can be found in the broad regions of the dayside, duskside, and nightside of the outside the plasmapause. One of a detailed dynamic spectra of the whistler-mode chorus emissions is shown in Figure 1.5. The whistler-mode waves are one of the most famous plasma waves in the inner magnetosphere. They usually generated by the electron temperature anisotropy in the perpendicular direction to the ambient magnetic field. Especially, the whistler-mode chorus emissions are observed in the inner magnetosphere. The dynamic spectra of the chorus emissions observed by Cluster spacecraft are shown in Figure 1.5 [*Santrik et al.*, 2003]. The chorus waves with the rising tones are found in Figure 1.5. The translated rising tone waves into the sound can be heard as "dawn chorus" of birds, which is the origin of the name "chorus emissions".

The electromagnetic ion cyclotron (EMIC) waves are also generated around the magnetic equatorial region. The EMIC waves are generated by the ion temperature anisotropy, which is the same energy source as the mirror mode waves. They are enhanced in the regions around the duskside of the slightly inside the plasmasphere when anisotropic energetic ring current ions are injected into the inner magnetosphere [*Jordanova et al.*, 2008]. The EMIC waves appear when the magnetic storm takes place. For more precise descriptions for the EMIC waves are shown in the next section. For other electromagnetic fluctuations in the inner magnetosphere, the magnetosonic waves and hiss are observed.
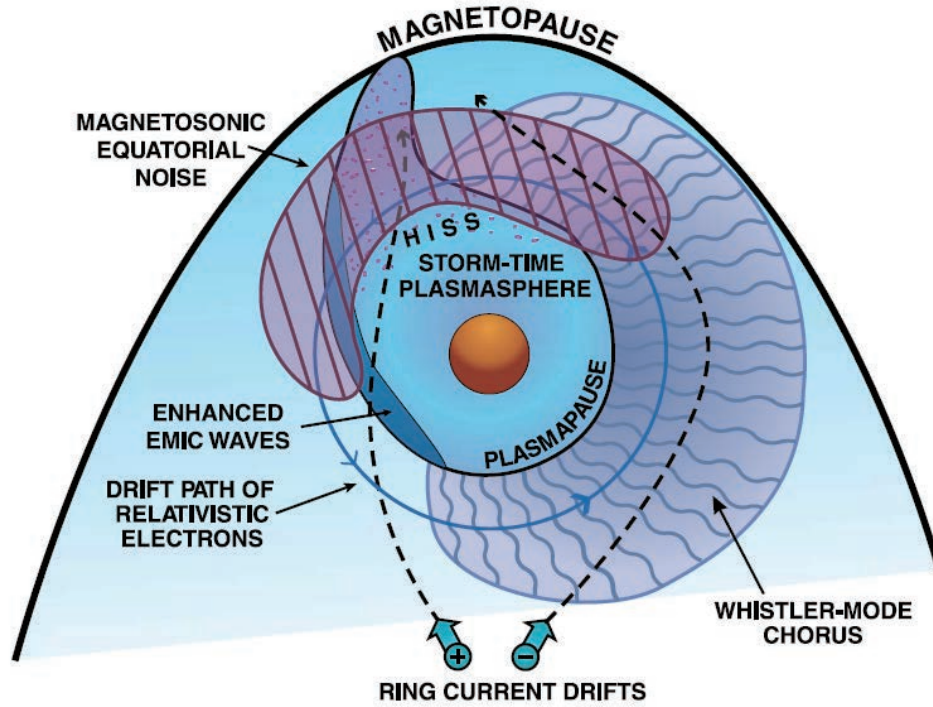
Figure 1.4: Schematic illustration of the spatial distribution of important waves in the inner magnetosphere [*after Thorne,* 2010].

## 1.2.2 Linear analyses of ion plasma instabilities driven by temperature anisotropy

The plasmas around the Earth are magnetized by the interplanetary magnetic field (IMF) or the Earth's eigen dipole magnetic field. The motion of the magnetized plasmas can be separated into parallel and perpendicular to the ambient magnetic field. In this thesis, we call these directions "the parallel direction" and "the perpendicular direction", respectively. The temperature anisotropy of ions are observed in the various regions (e.g. the solar wind [*Hellinger et al.,* 2006a], terrestrial magnetosheath [*Tsurutani et al.,* 1982], inner magnetosphere, magnetotail, and polar regions). When the temperature of the ions in the parallel direction $T_{\parallel,i}$ becomes larger than in the perpendicular direction $T_{\perp,i}$, $T_{\parallel,i}/T_{\perp,i} > 1$, the parallel and oblique fire hose instabilities are generated [*Sagdeev and Vedenov,* 1959; *Yoon,* 1990; *Quest and Shapiro,* 1996; *Hellinger and Travnicek,* 2006b]. By the parallel fire hose instability, the right-handed magnetosonic or R-mode electromagnetic ion cyclotron waves are generated. *Gary et al.* [1998] have shown that the whistler fire hose essentially a quasi-linear evolution. The oblique fire hose, on the other hand, drives the highly oblique electromagnetic waves called Alfven fire hose waves, which have
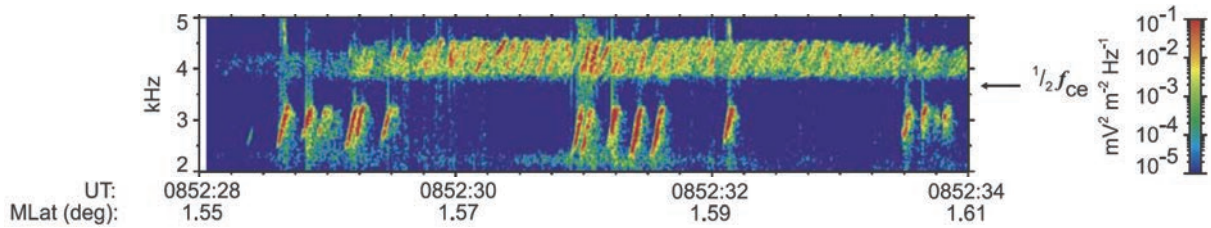
Figure 1.5: Dynamic spectra of the whistler-mode chorus emissions in the inner magnetosphere. [*after Santrik et al.*, 2003].

zero frequency [*Hellinger and Matsumoto*, 2000; 2001].

When the temperature anisotropy becomes larger in the perpendicular direction, $T_{\perp,i}/T_{\parallel,i} > 1$, there arise the L-mode EMIC and mirror instabilities. The L-mode EMIC wave, which is the dispersive mode, has the left-handed polarization and propagates mostly in the parallel direction. The linear dispersion relation of the L-mode EMIC wave [*Stix*, 1992] in the cold plasma approximation with multiple ions is given by

$$c^2 k^2 = \omega \left( \sum_s \frac{\omega_{ps}^2}{\Omega_s - \omega} - \frac{\omega_{pe}^2}{\Omega_e} \right), \tag{1.1}$$

where $c$, $\omega_{ps}$, and $\Omega_s$ are the speed of light, plasma and cyclotron frequencies of ion species $s$, respectively. The plasma and cyclotron frequencies of electrons are $\omega_{pe}$ and $\Omega_e$, respectively. We can confirm $k^2 \to \infty$ with $|\omega| \to \infty$. That means the L-mode EMIC waves are affected by the cyclotron resonance. The further characteristics of the L-mode EMIC waves are also studied by e.g. *Sagdeev and Galeev* [1969], *Terasawa and Hoshino* [1986], *Omura et al.,* [1988] and *Xiao et al.* [2007]. Especially, *Gary et al.,* [1994a] have calculated the threshold of the L-mode EMIC instability has the form

$$\frac{T_{\perp p}}{T_{\parallel p}} - 1 = \frac{S_p}{\beta_{\parallel p}^{\alpha_p}}, \tag{1.2}$$

where $S_p$ and $\alpha_p$ are fitting parameters, the former is a function of the choice of the maximum growth rate of the EMIC waves but $\alpha_p \simeq 0.4$ for a broad range of parameters. The existence of the alpha particles in the solar wind cause only weak changes in the threshold [*Gary et al.,* 1994b]. The threshold is confirmed in the solar wind by the ACE space craft observations [*Gary et al.,* 2001].

The mirror instability [*Chandrasekhar et al.,* 1958; *Hasegawa*, 1969, 1975], on the other hand, is the non-oscillatory mode which is excited in the oblique angle. Some characteristic of the mirror instability is very similar to the oblique fire hose. The characteristic of the mirror instability is the balance between the plasma pressure and the magnetic pressure

in a local point.

$$p_\perp + p_b \equiv Const., \tag{1.3}$$

where $p_\perp$ is the pressure of ions in the perpendicular direction, $p_b = B^2/(2\mu_0)$ is the pressure of the magnetic field and $\mu_0$ is the permeability in vacuum.

*Southwood and Kivelson* [1993] shows that the linear mirror instability proceeds as following. The schematic illustration for the growth of the linear mirror instability and the particle motions inside the mirror mode structures are shown in Figure 1.6. We can divide $p_\perp$ into the pressure of the bulk plasma and that of the resonant particles (which have parallel velocities close to zero). An increase or decrease in field leads to a pressure decrease or increase in the bulk of the plasma that causes a net local pressure deficit or surplus. The pressure is balanced by the resonant particle pressure in which the resonant particles respond being accelerated or decelerated by the field in the increasing or decreasing field regions thus responding in antiphase to the bulk plasma. Although some motion along the field is implicit in the field changes, this response plays no dynamic role.
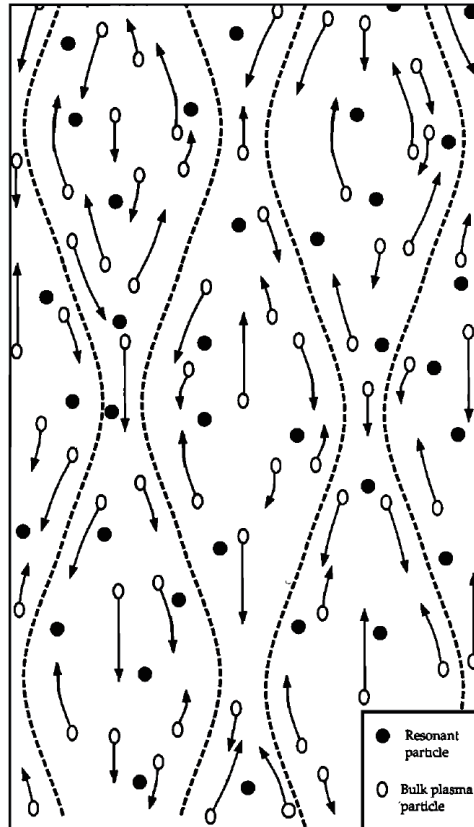


Figure 1.6: Schematic illustration of the linear mirror instability and the particles [*after Southwood et al.*, 1993].

The dispersion relation is given by (1.4), assuming the wave length of the mirror mode wave is much smaller than the ion inertial length and the phase velocity of the wave is much slower than that of ions [*Hasegawa*, 1969; *Baumjohann and Treumann*, 1997; *Hau et al.*, 2005].

$$\frac{\omega}{k_\parallel V_{th\parallel}} = -i\sqrt{\frac{2}{\pi}}\frac{\beta_\parallel}{\beta_\perp^2}\left(1+\beta_\perp - \frac{\beta_\perp^2}{\beta_\parallel} + \frac{k_\parallel^2}{k_\perp^2}\left\{1+\frac{1}{2}(\beta_\perp-\beta_\parallel)\right\}\right),\qquad(1.4)$$

where $\beta_\parallel$ and $\beta_\perp$ is the ions pressure normalized by the background magnetic field pressure in parallel and perpendicular direction, respectively and $V_{th\parallel}$ is a thermal velocity in the parallel direction. Here, we should note that the right hand side of (1.4) is purely imaginary number. Thus, the real part of the frequency is always naught whether the condition of plasma is stable or unstable. Assuming the complex frequency $\omega = \omega_r + i\omega_i$, we obtain (1.5) and (1.6).

$$\omega_r = 0 \qquad (1.5)$$

$$\omega_i = \left(\frac{2}{\pi}\right)^{\frac{1}{2}}\frac{\beta_\parallel}{\beta_\perp^2}kV_{th\parallel}\left[\left(\frac{\beta_\perp^2}{\beta_\parallel}-\beta_\perp-1\right)-\left(1+\frac{1}{2}(\beta_\perp-\beta_\parallel)\right)\cot^2\theta\right]\cos\theta \qquad (1.6)$$

From (1.5), the real part of the frequency is naught, thus we can confirm that the mirror mode waves do not propagate (the phase velocity is 0). When the linear growth rate, $\gamma = \omega_i$, is positive, the instability is caused and the waves start to grow. Therefore, we obtain the condition to cause the mirror instability from (1.6) [*Hasegawa*, 1969].

$$\frac{\beta_\perp}{\beta_\parallel} > 1 + \frac{1}{\beta_\perp}, \qquad (1.7)$$

$$\theta > \theta_c = \tan^{-1}\left[\left(\frac{1}{2}(\beta_\perp-\beta_\parallel)+1\right)\Big/\left(\frac{\beta_\perp^2}{\beta_\parallel}-\beta_\perp-1\right)\right]^{\frac{1}{2}}, \qquad (1.8)$$

where $\theta$ is angle between the wavenumber vector and the background magnetic field $\boldsymbol{B}_0$. From (1.8), we find that the mirror mode wave is excited in the oblique angle. For example, when $\beta_\parallel = 0.5$, $\beta_\perp = 2.0$, the cut off angle is $\theta_c \simeq 30.6°$. It is also noted that the growth rate is naught at $\theta = 90°$ in any case.

One of the examples of the spacecraft observation and the comparison with the linear theory have been provided by *Hellinger et al.*, [2006a]. Figure 1.7 [*after Hellinger et al.*, 2006a] shows the relative observation frequency of the proton beta value $\beta_{\parallel p} = 2\mu_0 p_\parallel/B^2$ and the temperature anisotropy of proton $T_{\perp p}/T_{\parallel p}$) in the solar wind with the velocity $V_{sw} \leqq 600$ km/s. Their observation results show that a majority of observations lies outside the regions unstable with respect to the four instabilities (for the used plasma parameters). It also indicate two possible constraints for the higher $\beta_{\parallel p}$: one for $T_{\perp p}/T_{\parallel p} <$
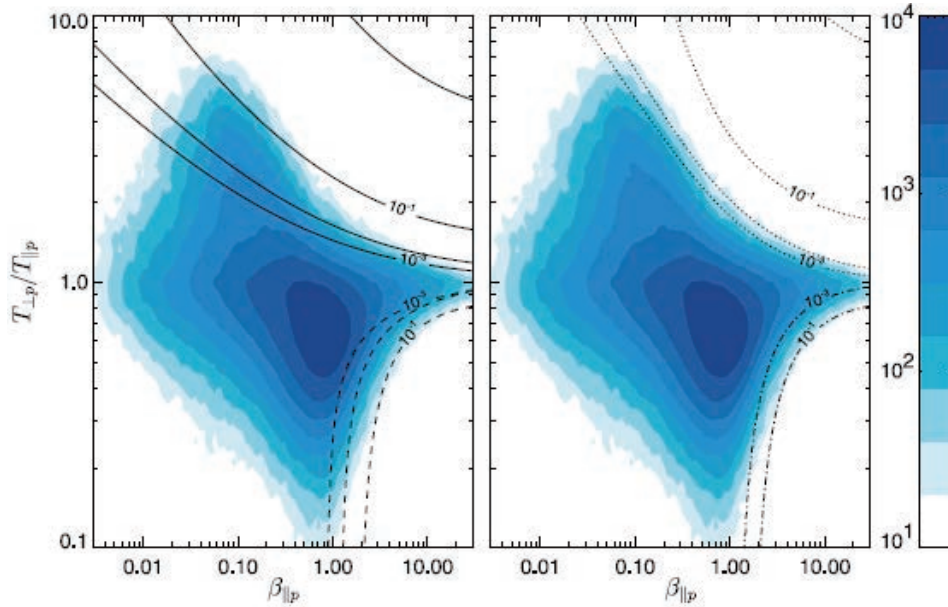
Figure 1.7: A color scale plot of the relative frequency of $(\beta_{\|p},\ T_{\perp p}/T_{\|p})$ in the solar wind with speed $V_{sw} \leqq 600$ km/s by WIND/SWE data (1995-2001). The black curves show the maximum growth rate $\gamma_M/\Omega_H$ (left) for the L-mode EMIC (solid curves), the parallel fire hose (dashed curves) instabilities, (right) for the mirror (dotted curves) and the oblique fire hose (dash-dotted curves) instabilities. [*after Hellinger et al.,* 2006a]

1 and another for $T_{\perp p}/T_{\|p} > 1$ [c.f. *Kasper et al.,* 2002]. For $T_{\perp p} > T_{\|p}$ the apparent constraint is compatible with the threshold condition for the mirror instability. The linear predictions for the L-mode EMIC instability does not seem to constrain the observations. For $T_{\perp p} < T_{\|p}$ the constraint seems to be more compatible with the oblique fire hose than with the parallel one, at least for $\beta_{\|}$. Near the Earth, the solar winds are heated in the perpendicular directions when they go through the bowshock. The L-mode EMIC and mirror instabilities take place in the magnetosheath even though the majority of the solar wind are outside the unstable regions.

## 1.3 Significance of Computer Simulations

For studies on the space plasma environments, there mainly exist three approaches: ground and spacecraft observations, theoretical analyses, and computer simulations. Many kinds of plasma waves around the Earth, other planets, and in the solar wind have been found by the spacecraft and ground observations. The ground observations have also found the auroras and the magnetic field disturbance. Through the statistical analyses of the observations, some parts of the physical characters of the plasma waves have been

clarified. For example, the waveform analyses clarifies that the BEN is the set of the ESWs. Moreover, in the recent development of the devices, the wave particle interactions become to be calculated inside the spacecraft. However, since observations obtain only limited data at a point or several points, we cannot understand the spatial evolutions of the waves and plasmas.

To explain the observed plasma wave phenomena, theoretical approaches have been investigated. By linear approximations, which neglect second or higher fluctuations in the Maxwell's equations and the momentum equations of the particles, we obtain the linear dispersion relations of the plasma waves [e.g. *Stix*, 1992]. The growth rate of the waves, and the linear and quasi-linear scattering of the particles have been investigated [*Gendrin*, 1968]. However, the treatment of the waves and the plasmas are limited in the theoretical approach. It is quite difficult to solve the evolution of the distribution functions $f$ of the plasmas, which is given by Vlasov equation. The limitation of the theory also arises in the difficulty for solving nonlinear equations when large amplitude electromagnetic waves are assumed.

As the third approach, computer experiments, starts to be investigated for the space plasmas. We must solve Maxwell's equations and equations for the plasma dynamics. The Finite Difference Time Domain (FDTD) method, which solves the differentiated Maxwell's equations, [*Taflove*, 1995] is easy to combine with various numerical plasma models, which have been developed in the field of plasma simulations [*Matsumoto and Omura*, 1993]. There exist two treatments for the space plasmas to solve their behavior self-consistently. We can treat the plasmas as "fluid" or "particles". If we assume that the plasmas are the fluid, the velocity distribution function is assumed as Maxwellian distribution. The fluid plasma simulations solve the Maxwell's equations and the fluid equations of the plasmas. In the fluid equations, since the plasmas have the Maxwellian distribution function, the kinetic effects of the plasmas are neglected. Thus, the method can solve problems in huge regions such as the global and planetary magnetosphere. Magneto-Hydro-Dynamic (MHD) model is widely used as one of the fluid models. In the MHD model, the electron and ions are treated as one fluid.

To solve the kinetic effects, we should consider the cyclotron motion of the electrons and ions. To treat the evolution of the distribution function $f$ of the electrons and ions, There are two methods: (1) Particle-In-Cell (PIC) simulations [e.g. *Dawson*, 1983; *Birdsall and Langdon*, 1985] and (2) Vlasov simulations [e.g. *Yabe et al.*, 2001; *Umeda* 2008]. Both of them include the kinetic effect of the plasmas.

The PIC simulations have been developed in 1980's [e.g. *Dawson*, 1983; *Birdsall and Langdon*, 1985]. The basic equations for the PIC simulations are the Maxwell's equations

and the momentum equations, and the solving methods have been established. These equations are solved with each other. The superparticles are assumed in the simulation space. The superparticles in the Lagrangian frame are tracked in continuous space. On the other hand, their moments such as the charge and current densities, and electromagnetic field components defined as Eulerian variables are computed simultaneously on computational mesh points [*Birdsall and Langdon*, 1985]. Because the number of the particles and the sizes of the superparticles in the PIC simulation are limited by the resource of the computers, the numerical noise arises by the lack of the particles. The plasma simulations using the PIC approach is categorized into two groups: a full-particle scheme in which all the species in plasmas are treated as particles, and a hybrid scheme in which electrons and ions are generally treated as fluid and particles, respectively.

Vlasov simulations, on the other hand, treat Vlasov equation which is the collisionless Boltzman equation. Solving the equation, we obtain the time evolution of the distribution function in the phase space. It can also describe kinetic effects of the plasmas. The Vlasov simulation is much noise-less method rather than the PIC simulations. However, since the dimension of the distribution function in the phase space is six, huge memory space is needed in the supercomputers. Due to the lack of the resources of the computers, it is quite difficult to solve the multi-dimensional wave particle interactions in the ion scale by Vlasov equations. Therefore, in the present thesis, we use the PIC simulations.

## 1.4 Contribution of the Present Study

The motivation of our present study is to understand the source mechanisms responsible for the electromagnetic wave activity in the terrestrial magnetosheath and in the inner magnetosphere. In this thesis, we investigate the plasma wave instabilities, the L-mode EMIC and mirror instabilities, driven by the temperature anisotropy of the ions in the perpendicular directions. The present thesis describes the nonlinear characteristics of these instabilities by self-consistent computer simulations, comparing with the spacecraft observations. Especially, we focus on the problems in the Earth's magnetosheath and in the Earth's inner magnetosphere, where these instabilities take place dominantly. This thesis consists of seven chapters.

In Chapter 2, we explain numerical techniques and models of hybrid simulation methods which are used in the present study. We explain the basic equations and algorithm of the hybrid simulation. The three different models, multi-dimensional periodic boundary model, multi-dimensional open boundary model, and 1D model with cylindrical geometry, are developed. We briefly explain the open boundary using the masking method. We

further developed the hybrid simulation model assuming a cylindrical magnetic geometry. We explain the numerical treatment of the parabolic magnetic field modeling the equatorial region of the inner magnetosphere and the initial particle distributions in the nonuniform cylindrical magnetic geometry.

In Chapter 3, we investigate the competing processes between the L-mode EMIC and mirror instabilities in the Earth's magnetosheath. The spacecraft observation results indicate that the non-oscillatory magnetic structures are usually observed in the downstream of the quasi-perpendicular shock. However, the linear analyses show that the L-mode EMIC instability have larger growth rate than that of the mirror instability. We explain how this contradiction between observations and theory appears by performing the one-, two- and three-dimensional (1D, 2D, and 3D) simulations with the periodic boundary. In Section 3.3, we compare wave energy growth rates of both the mirror and EMIC modes in linear stage. The results exhibit a principal difference between 2D and 3D approaches and show that the free energy flows mostly into the mirror mode in linear stage. The effect of the existence of the multiple ions is also estimated. In Section 3.4, we analyze the nonlinear evolution of these instabilities. In Section 3.5, we investigate the heating of protons by the nonlinear evolution of the L-mode EMIC waves.

In Chapter 4, we further study the nonlinear evolutions of the mirror mode structures. From the recent observations [*Soucek et al.*, 2008], the magnetic structures, which are called magnetic peak and magnetic dip, are found in the magnetosheath. As one of the generation mechanisms for the magnetic peak and dip, the nonlinear evolution of the mirror mode structures are studied. To obtain the fine structures of the non-oscillatory mirror mode, we perform the multi-dimensional hybrid simulations with open boundaries. We compare the 2D and 3D simulations and find the difference of the magnetic structures. In Section 4.3, we also confirm the ion beta dependency of the magnetic structures that is predicted by the observations and show how the magnetic peaks and dips are generated from the mirror mode structures in different initial conditions and models. We find that continuous coalescence of the magnetic structures generates the magnetic peaks. The coalescence takes place due to the attractive force between the diamagnetic current loops forming the magnetic dips.

In Chapter 5, the rising-tone emissions in the ULF frequency range, which are called EMIC triggered emissions [*Pickett et al.,* 2010; *Omura et al.,* 2010], in the Earth's inner magnetosphere are investigated. A hybrid simulation model with a cylindrical magnetic geometry is used. In Section 5.2, the EMIC triggered emissions are reproduced around the equatorial region with realistic simulation parameters. We compare the simulation results with Cluster observation results and the nonlinear wave growth theory [*Omura et*

*al.,* 2010]. In Section 5.3 we show the existence of the proton holes, which are predicted in the nonlinear wave growth theory [*Omura et al.,* 2010] in the velocity phase space. The amount of the energetic protons which are scattered by the triggered emissions in the equatorial region and go into the loss cone are estimated. We also performed parametric analyses for the triggered emissions to find the critical range of the amplitude of the triggering waves in Section 5.4. Moreover, in Sections 5.5 and 5.6, we find the EMIC triggered emissions in the lower branch of the dispersion relation and natural EMIC triggered emissions, which have not been observed yet.

In Chapter 6, we show another type of the EMIC wave emissions below $He^+$ cyclotron frequency induced by the EMIC triggered emissions by both spacecraft observation and simulation results. In Section 6.2, we show the observation results of the EMIC waves and the energetic particles in the inner magnetosphere. We find the $He^+$ branch EMIC waves after the multiple EMIC triggered emissions. We also find the pitch angle scattering of the protons by the triggered and the $He^+$ branch waves. In Section 6.3, we reproduce multiple EMIC triggered emissions. We show how the EMIC waves in the $He^+$ branch are generated through the nonlinear wave particle interactions due to the EMIC triggered emissions by reproducing these emissions in the cylindrical parabolic magnetic field model, which are also used in Chapter 5.

In Chapter 7, we will summarize the present study and give conclusions obtained in the present computer simulations. We also present suggestions for future studies.

# Chapter 2

# Hybrid Codes for Computer Experiments

## 2.1  Introduction: Hybrid Simulation

The plasmas consist of the electrons and the ions. Because of the mass ratio $m_i/m_e = 1836$, the characteristic length and time of electron are much longer and shorter than those of ions, respectively. The full particle-in-cell simulation [e.g. *Birdsall and Langdon*, 1981], which assumes both the electrons and the ions as particles, is a famous method to solve the interactions between the space plasmas and the electromagnetic fields. Hybrid simulation is developed to solve the wave particle interactions which occurs in the ion spatial and time scales. The hybrid simulation were originally developed for and extensively applied to dynamical studies of high density pinch experiments [*Chodura*, 1975; *Sgro and Nielson*, 1976; *Hamasaki et al.*, 1977]. In the hybrid simulation code, the ions are treated as particles and the electron is a mass-less fluid to satisfy the charge quasi-neutrality instantaneously in each local point. With this assumption, the kinetic effects of the electrons are neglected. Using this code, we can calculate the ion scale physics saving the computer resources.

In this chapter, we describe the numerical techniques which are commonly used in the computer simulations in the present thesis. In sections from 2.2 to 2.3, we briefly explain the basic equations, and the algorithm and the models. In section 2.4, the open boundary models in the multi-dimensional hybrid simulation is described. In section 2.5, the hybrid code is modified to contain the cylindrical geometry modeling the Earth's inner magnetosphere.

## 2.2   Basic Equations

The basic equations of the hybrid simulation code used in our present studies [*Shoji et al.,* 2009; *Shoji and Omura,* 2011; *Shoji et al.,* 2011; *Shoji et al., submitted*] are given as follows.

$$\nabla \times \boldsymbol{E} = -\frac{\partial \boldsymbol{B}}{\partial t} \tag{2.1}$$

$$\nabla \times \boldsymbol{B} = \mu_0 \boldsymbol{J} \tag{2.2}$$

$$-en_e \boldsymbol{E} + \boldsymbol{J}_e \times \boldsymbol{B} - \nabla p_e = 0 \tag{2.3}$$

$$\frac{d\boldsymbol{v}_s}{dt} = \frac{q_s}{m_s}(\boldsymbol{E} + \boldsymbol{v}_s \times \boldsymbol{B}) \tag{2.4}$$

where $\boldsymbol{E}$ is the electric field, $\boldsymbol{B}$ is the magnetic field, $\mu_0$ is the magnetic permeability in vacuum, and $\boldsymbol{J}$ is the current density. We have neglected the displacement current.

Equation (2.3) shows the momentum equation of the electron fluid, in which the inertia of the electron fluid has been neglected. The value $-e$ is the charge of an electron and $\boldsymbol{J}_e$ and $p_e$ are the current and pressure of electrons, respectively. The current of the electron fluid is given by

$$\boldsymbol{J}_e = \boldsymbol{J} - \sum_s q_s n_s \boldsymbol{v}_s. \tag{2.5}$$

We assume adiabatic variation of $p_e$ as the electron pressure.

$$p_e = p_{e0}(n_e/n_0)^\gamma \tag{2.6}$$

where, $p_{e0}$ and $n_0$ are the initial pressure and density of electrons, respectively and $\gamma$ is the ratio of specific heat. The charge density of electrons is given by the quasi-neutrality condition.

Equation (2.4) shows the equation of motion of ions, where $v_s$, $q_s$, $m_s$ are the velocity, charge, and mass of ions. The subscript "s" indicates species of ions.

By the electron fluid, a charge neutrality is satisfied as shown in (2.7).

$$-en_e + \sum_s q_s n_s = 0 \tag{2.7}$$

In this hybrid code, the electric field is calculated sequentially. From (2.3) and (2.7), we obtain

$$\boldsymbol{E} = -\frac{\boldsymbol{J}_i \times \boldsymbol{B}}{\rho_i} + \frac{(\nabla \times \boldsymbol{B}) \times \boldsymbol{B}}{\mu_0 \rho_i} - \frac{\nabla p_e}{\rho_i}, \tag{2.8}$$

where, $\boldsymbol{J}_i$, and $\rho_i$ are the ion current density and the ion charge density, respectively.

## 2.3   Algorithm of the Hybrid Code

In this hybrid code, the Current Advance Method and the Cyclic Leapfrog (CAM-CL) modified by Buneman-Boris method[*Matsumoto and Omura.*, 1993] are used to calculate the equation of motion of ions. To computing the ion current in each grid, we used the "area sharing method" to improve the accuracy. The basic algorithm of the hybrid code is shown below, and the time chart of the algorithm is shown in Figure 2.1.

1. At the initial time, each physical value is calculated as shown in the follow equations with given $\boldsymbol{x^0}$, $\boldsymbol{v^0}$, and $\boldsymbol{B^0}$.

$$\rho_i^0 = \sum_s \sum_{x^0 \in R} q_s \tag{2.9}$$

$$\boldsymbol{J}_i^0 = \sum_s \sum_{x^0 \in R} q_s \boldsymbol{v}_s \tag{2.10}$$

$$\boldsymbol{x}_s^{\frac{\Delta t}{2}} = \boldsymbol{x}_s^0 + \frac{\Delta t}{2} \boldsymbol{v}^0 \tag{2.11}$$

$$\rho_i^{\frac{\Delta t}{2}} = \sum_s \sum_{\boldsymbol{x}^{\frac{\Delta t}{2}} \in R} q_s \tag{2.12}$$

$$\boldsymbol{v}_s^{\frac{\Delta t}{2}} = \boldsymbol{v}_s^0 + \frac{\Delta t}{2} \frac{q}{m} \left( \boldsymbol{E}^0 + \boldsymbol{v}_s^0 \times \boldsymbol{B}^0 \right) \tag{2.13}$$

2. $\boldsymbol{B}^{t+\frac{\Delta t}{2}}$, and $\boldsymbol{E}^{t+\frac{\Delta t}{2}}$ are calculated as

$$\boldsymbol{B}^{t+\frac{\Delta t}{2}} = \boldsymbol{B}^t - \int_t^{t+\frac{\Delta t}{2}} \nabla \times \boldsymbol{E} \left( \rho_i^t, \boldsymbol{J}_i^t, B^{t_{sub}}, p_e^t \right) dt_{sub} \tag{2.14}$$

$$\boldsymbol{E}^{t+\frac{\Delta t}{2}} = \boldsymbol{E} \left( \rho_i^{t+\frac{\Delta t}{2}}, \boldsymbol{J}_i^{t+\frac{\Delta t}{2}}, \boldsymbol{B}^{t+\frac{\Delta t}{2}}, p_e^{t+\frac{\Delta t}{2}} \right). \tag{2.15}$$

3. The equation of motion of ions is solved by Buneman-Boris method.

$$\boldsymbol{v}_s^{t+\Delta t} = \boldsymbol{v}_s^t + \Delta t \frac{q_s}{m_s} \left( \boldsymbol{E}^{t+\frac{\Delta t}{2}} + \boldsymbol{v}_s^{t+\frac{\Delta t}{2}} \times \boldsymbol{B}^{t+\frac{\Delta t}{2}} \right) \tag{2.16}$$

$$x_s^{t+\frac{3}{2}\Delta t} = x_s^{t+\frac{\Delta t}{2}} + \Delta t \boldsymbol{v}_s^{t+\Delta t} \tag{2.17}$$

4. The ion current density at $t+\Delta t$ and the ion charge density at $t+\frac{3}{2}\Delta t$ are calculated, and we obtain the ion charge density at $t+\Delta t$ by the charge density at $t+\frac{3}{2}\Delta t$ and $t+\frac{\Delta t}{2}$.

$$\boldsymbol{J}_i^{t+\Delta t} = \sum_s \sum_{\boldsymbol{x}^{t+\Delta t} \in R} q_s \boldsymbol{v}_s^{t+\Delta t} \tag{2.18}$$

$$\rho_i^{t+\frac{3}{2}\Delta t} = \sum_s \sum_{\boldsymbol{x}_s^{t+\frac{3}{2}\Delta t} \in R} q_s \tag{2.19}$$

$$\rho_i^{t+\Delta t} = 0.5 \times \left( \rho_i^{t+\frac{\Delta t}{2}} + \rho_i^{t+\frac{3}{2}\Delta t} \right) \tag{2.20}$$

5. We obtain the electromagnetic field at $t + \Delta t$.

$$\boldsymbol{B}^{t+\Delta t} = \boldsymbol{B}^t - \int_{t+\frac{\Delta t}{2}}^{t+\Delta t} \nabla \times \boldsymbol{E}\left(\rho_i^{t+\Delta t}, \boldsymbol{J}_i^{t+\Delta t}, B^{t_{sub}}, p_e^{t+\Delta t}\right) dt_{sub} \tag{2.21}$$

$$\boldsymbol{E}^{t+\Delta t} = \boldsymbol{E}\left(\rho_i^{t+\Delta t}, \boldsymbol{J}_i^{t+\Delta t}, \boldsymbol{B}^{t+\Delta t}, p_e^{t+\Delta t}\right) \tag{2.22}$$

6. The ion current density at $t + \frac{3}{2}\Delta t$ is calculated, and the electric field is updated at $t + \frac{3}{2}\Delta t$.

7. Back to No. 2.

The time step for the electromagnetic field which is restricted by Courant condition[*Matsumoto and Omura*, 1993] is smaller than that for the particles. Thus, when we advance the magnetic field for the half time step $\frac{\Delta t}{2}$, we take smaller time step and use it to solve the magnetic field. The time step for the electromagnetic field is defined as $\Delta t_{sub} = \Delta t/16$ during the particles advances from $t$ to $t + \frac{\Delta t}{2}$.
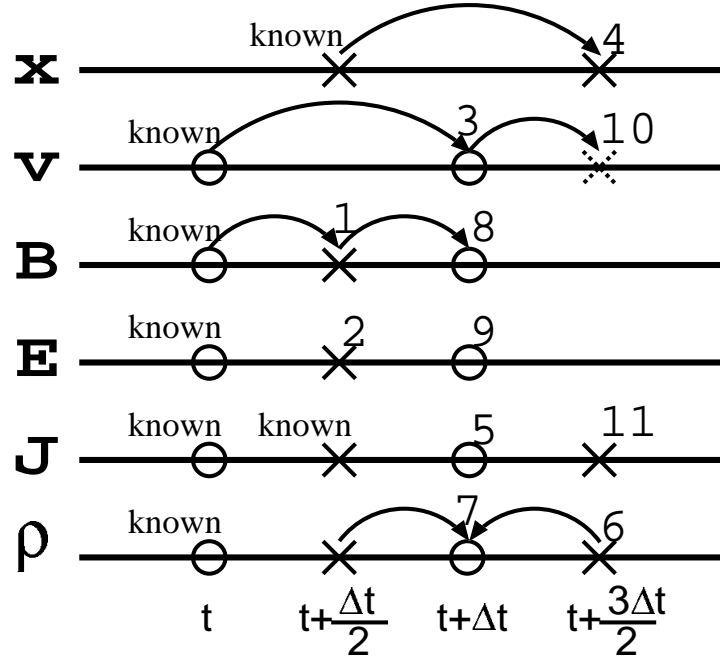


Figure 2.1: Time chart of the algorithm of the hybrid code

All values in the simulation code is normalized as Table 2.1, where $V_{\mathrm{A}}$ is Alfven velocity of the proton, $\Omega_{\mathrm{H}}$ is cyclotron frequency of the proton, $B_0$ is the ambient magnetic field along to $x$ direction, $m_0$ is the mass of the proton, $\rho_0$ is the density of the proton. and the normalized value is shown as $\tilde{X}$ for a physical value $X$.

| physical value $X$ | normalized value $\tilde{X}$ |
|:---:|:---:|
| velocity $V$ | $\tilde{V}V_{\mathrm{A}}$ |
| time $T$ | $T = \tilde{T}/\Omega_{\mathrm{H}}$ |
| length $L$ | $\tilde{L}V_{\mathrm{A}}/\Omega_{\mathrm{H}}$ |
| magnetic field $B$ | $\tilde{B}B_0$ |
| electric field $E$ | $\tilde{E}V_{\mathrm{A}}B_0$ |
| ion charge $q$ | $\tilde{q}e$ |
| ion mass $m$ | $\tilde{m}m_0$ |
| density $\rho$ | $\tilde{\rho}\rho_0$ |
| beta $\beta$ | $\frac{B_0^2}{2\mu_0}\tilde{\beta}$ |

Table 2.1: The normalization of the physical values in the simulation code.

Figure 2.2 shows the simulation model of the hybrid code with the periodic boundaries. The bi-maxwellian particles, which are shown in (2.23), are uniformly distributed in the simulation space.

$$f(v_\parallel,\ v_\perp) = \frac{n_h}{(2\pi)^{3/2}V_{th\parallel}V_{th\perp}^2}\exp\left(-\frac{v_\parallel^2}{2V_{th\parallel}} - \frac{v_\perp^2}{2V_{th\perp}}\right) \tag{2.23}$$

where $n_h$, $V_{th\parallel}$, and $V_{th\perp}$ are the density, thermal velocities in the parallel and perpendicular directions of energetic protons, respectively. When we assume 1D simulation, the simulation space is along to the background magnetic field vector. In the 2D model, The axis parallel to the ambient field and one of the axis perpendicular to the ambient magnetic field are assumed as shown in Figure 2.2.

## 2.4 Open Boundary Simulation Model

When we assume the open boundary condition in the hybrid simulations, the musking method [*Tajima and Lee,* 1981] is used to dump the waves which go out from the simulation space. The masking method is modified by *Umeda et al.,* [2001]. Dumping layers are attached at both ends of the physical region as shown in Figure 2.3. The transverse wave magnetic fields are dumped as

$$B_{dump}(x) = f_M(x)B(x) \tag{2.24}$$

at each time step, where $f_M(x)$ is the masking function. The masking function $f_M(x)$ is defined as

$$f_M(x) = \begin{cases} 1 & (|x| \leq X/2) \\ 1 - r_D\dfrac{(|x| - X/2)^2}{L_D^2} & (|x| > X/2), \end{cases} \tag{2.25}$$
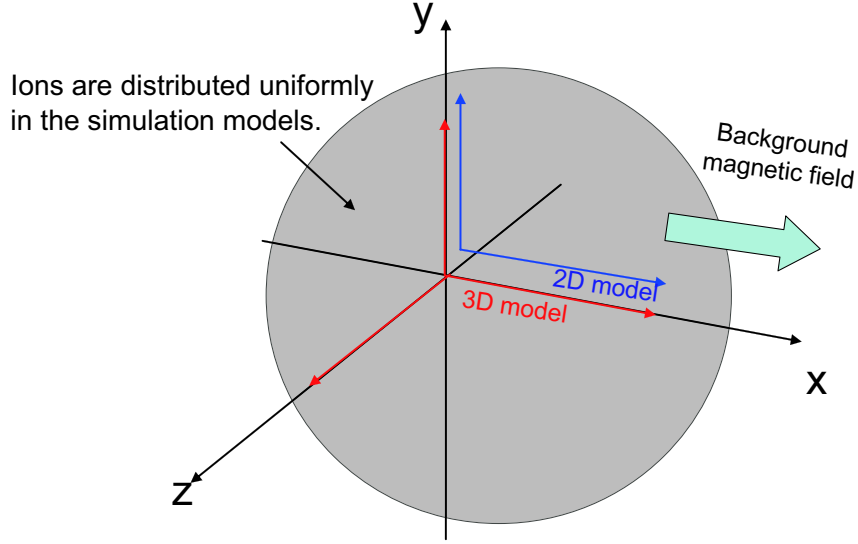
Figure 2.2: The models of three dimensional hybrid simulation.

where $X$ is the size of the simulation space, $L_D$ is the length of the damping region in each direction and $r_D = 0.0129$ is a coefficient for the best dumping effect given by the experimental equation [*Umeda et al.*, 2001]. The coefficient $r_D$ is expressed as the following optimized condition obtained by the previous parameter runs of the particle-in-cell simulations:

$$\frac{N_D r_D^2}{3v_g(\Delta t/\Delta x)} \simeq 3.3, \tag{2.26}$$

where $v_g$ is the group velocity of the waves. Because the hybrid simulations treat only the low frequency waves, the single masking for the magnetic field $\boldsymbol{B}$ is used to damp the waves effectively.

The test simulations for the open boundary is performed with the number of grids nx= 1024, the grid spacing $dx = 0.1$, the number of grids in the dumping layer rnx= 128, and $dt = 0.004$. Only the cold ion, of which the thermal velocity is neglected, is assumed in the simulation. The time evolution of the wave amplitude $B_\perp$ is shown in Figure 2.4. At $x = 0$, we set the current source and generate the waves during one cycle of the proton gyro motion. We can find the excitation of both R-mode and L-mode waves, which are the solution of the dispersion relation in the ion plasmas. Figure 2.4 indicates that these waves propagate away from the center, and they are absorbed at each boundary.
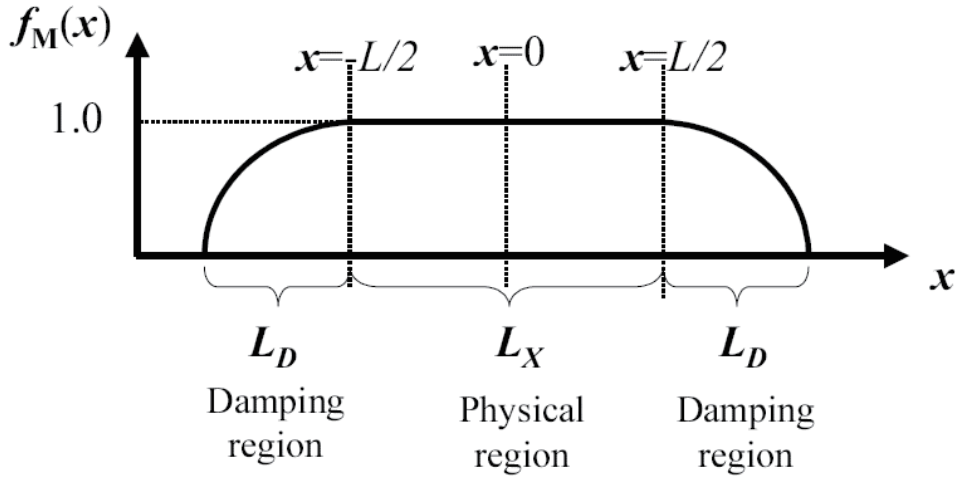
Figure 2.3: The masking method for the open boundary model [*Umeda et al.*, 2001].

## 2.5 Hybrid Code with Cylindrical Geometry

### 2.5.1 Nonuniform parabolic background magnetic field with cylindrical geometry

For the realistic simulations in the Earth's inner magnetosphere, we have further modified a self-consistent one-dimensional (1D) hybrid model along the background magnetic field in the $x$ direction. The algorithm of the hybrid code is described in Section 2.2. In the hybrid simulation the displacement current and the electron inertia are neglected, and these assumptions are consistent with the nonlinear wave growth theory [*Omura et al.*, 2010]. A schematic illustration of the simulation model is shown in Figure 2.5. While the field equations are solved as the 1D system taken along the $x$ axis, the background magnetic field has a cylindrical geometry around the $x$ axis, and ions are assumed to gyrate around the magnetic field with finite cyclotron radii. The magnetic equator is assumed at the center of the model ($x = 0$), and the $x$ component of the background magnetic field is defined by a parabolic function as an approximation of the dipole magnetic field of the Earth.

$$B_{0x}(x) = B_{0eq}(1 + ax^2), \tag{2.27}$$

where $B_{0eq}$ is the value at the equator, $a = 4.5/(LR_E)$, $L = 4.3$ and the Earth's radius $R_E = 6,387$ km. To satisfy the condition $\nabla \cdot \boldsymbol{B} = 0$, we assume the radial component of
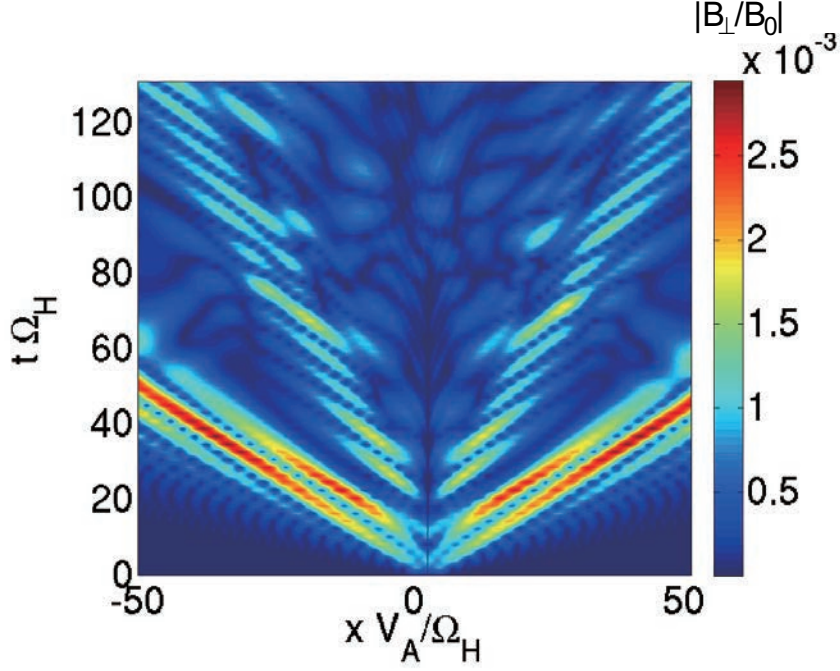
Figure 2.4: The amplitude of the magnetic field in the perpendicular direction in $x$ - $t$ diagram.

the ambient magnetic field as

$$B_{0r} = -\frac{r_{Li}}{2}\frac{\partial B_{0x}}{\partial x} \tag{2.28}$$

$$= -a r_{Li} B_{0eq} x \tag{2.29}$$

where $r_{Li} = v_\perp/\Omega_{ci}$ is the Larmor radius of ions, and $\Omega_{ci}$ is the local cyclotron frequency of ions of species $i$. The same cylindrical geometry is assumed in recent simulation studies of whistler-mode chorus emissions [*Katoh et al.*, 2007; *Omura et al.*, 2008; *Hikishima et al.*, 2009a, 2009b, 2010]. The radial component of the background magnetic field $\boldsymbol{B}_{0r}$ is always perpendicular to the velocity in the perpendicular direction $\boldsymbol{v}_\perp = (v_y,\ v_z)$. Thus, the component of $\boldsymbol{B}_{0r}$ is calculated as

$$\boldsymbol{B}_{0r} = \begin{bmatrix} -\dfrac{v_z}{|v_\perp|}B_r \\ \dfrac{v_y}{|v_\perp|}B_r \end{bmatrix}. \tag{2.30}$$

Substituting (2.29) into (2.30), these components are expressed as follows

$$\boldsymbol{B}_{0r} = \begin{bmatrix} \dfrac{v_z}{\Omega_{ci}}a B_{0eq} x \\ -\dfrac{v_y}{\Omega_{ci}}a B_{0eq} x \end{bmatrix}. \tag{2.31}$$

To include this nonuniform magnetic field, we modified Buneman-Boris method using in the hybrid code shown in (2.16) and (2.17). The modified method to update the velocity is shown as following. The magnetic field at $x$ should be calculated after 1. because the direction of $\boldsymbol{v}$ is changed by $\boldsymbol{E}$ before calculating the Lorentz force in Buneman-Boris method.

1. Calculating $v_s^-$ by half time step.

$$\boldsymbol{v}_s^- = \boldsymbol{v}_s^t + \frac{\Delta t}{2}\frac{q_s}{m_s}\boldsymbol{E}^{t+\frac{\Delta t}{2}} \tag{2.32}$$

2. Calculating $B_{0x}(x)$ and $\boldsymbol{B}_{r0}(x,\ \boldsymbol{v}_\perp)$ using $\boldsymbol{v}^-$ by (2.27) and (2.31). The fluctuation of the magnetic field $\delta\boldsymbol{B}$ at $x^{t+\frac{\Delta t}{2}}$ is also interporated. The magnetic field is $\boldsymbol{B}^{t+\frac{\Delta t}{2}} = \boldsymbol{B}_0(x,\boldsymbol{v}_\perp) + \delta\boldsymbol{B}$.

3. Calculating $\boldsymbol{v}_s^o$ and $\boldsymbol{v}_s^+$

$$\boldsymbol{v}_s^o = \boldsymbol{v}_s^- + \boldsymbol{v}_s^- \times \frac{q_s}{m_s}\boldsymbol{B}^{t+\frac{\Delta t}{2}}\frac{\Delta t}{2} \tag{2.33}$$

$$\boldsymbol{v}_s^+ = \boldsymbol{v}^- + \frac{2}{1 + ((q_s/m_s)B^{t+\frac{\Delta t}{2}}\Delta t/2)^2}\boldsymbol{v}^o \times \boldsymbol{B}^{t+\frac{\Delta t}{2}}\frac{\Delta t}{2} \tag{2.34}$$

4. We obtain $\boldsymbol{v}^{t+\frac{\Delta t}{2}}$

$$\boldsymbol{v}^{t+\frac{\Delta t}{2}} = \boldsymbol{v}_s^+ + \frac{q_s}{m_s}\boldsymbol{E}^{t+\frac{\Delta t}{2}} \tag{2.35}$$

## 2.5.2   Initial particle distribution functions

For the particles in the simulation model, energetic $H^+$ ions with temperature anisotropy are introduced as resonant particles with EMIC waves, forming a loss cone distribution function expressed by

$$f(v_\parallel,\ v_\perp) = \frac{n_h}{(2\pi)^{3/2}V_{th\parallel}V_{th\perp}^2}\exp\left(-\frac{v_\parallel^2}{2V_{th\parallel}}\right)g(v_\perp), \tag{2.36}$$

The function $g(v_\perp)$ is defined as

$$g(v_\perp) = \frac{1}{1-\beta}\left\{\exp\left(-\frac{v_\perp^2}{2V_{th\perp}^2}\right) - \exp\left(-\frac{v_\perp^2}{2\beta V_{th\perp}^2}\right)\right\}, \tag{2.37}$$

where $\beta = 0.1$. The quiet start [*Birdsall and Langdon*, 1985] is used to reduce the initial thermal fluctuations. The quiet start requires pairs of particles with the same positions and parallel velocities. The particles of each pair have opposite perpendicular velocities with the same magnitude forming no current in the transverse plane initially. The energetic protons are initialized to form a spatial distribution that is stable in time with adiabatic motion in the parabolic magnetic field.
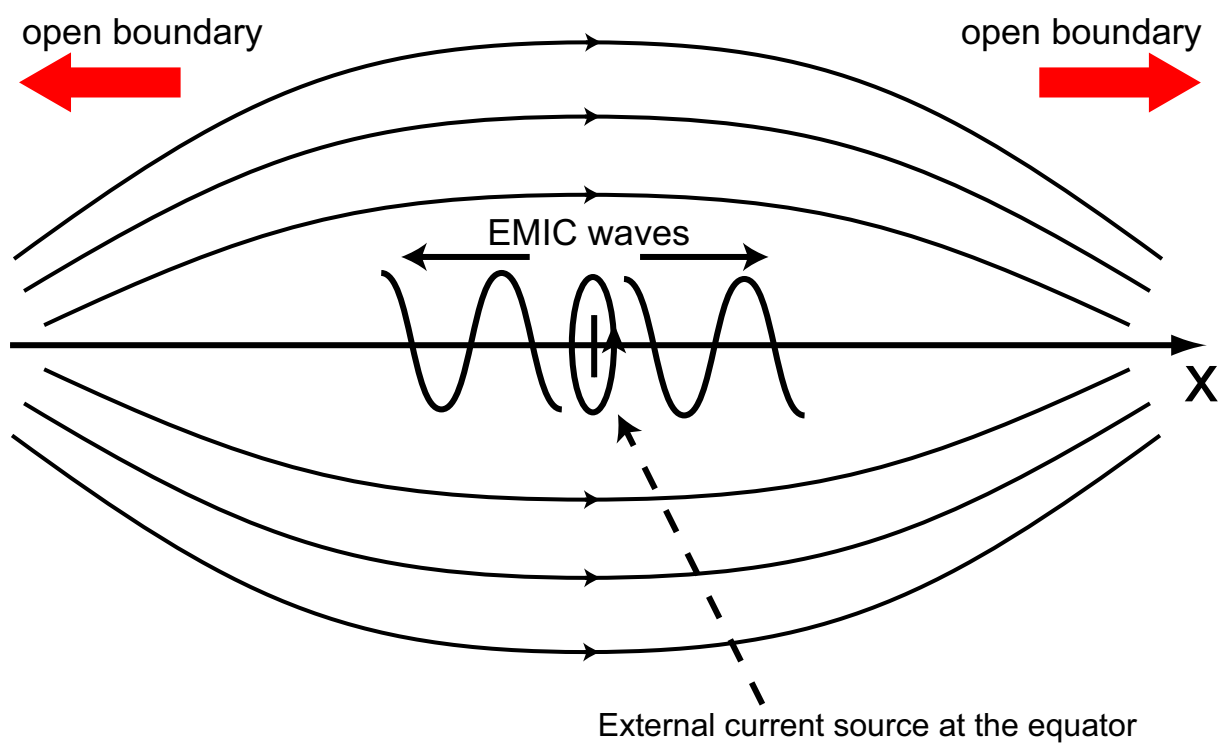
Figure 2.5: Schematic illustration of the 1D hybrid simulation model with the cylindrical geometry.

### 2.5.3   Test simulations

The energetic particles cause the mirror motion in the parabolic magnetic field. We performed the test simulation for the mirror motion of a particle. We set the center of the simulation model, where the magnetic field is minimum, at $x = 102.4 V_A/\Omega_H$. Figure 2.6a show the time evolution of the trajectory of the particle in the cylindrical parabolic background magnetic field. We can confirm the mirror motion of the particle of which the center is $x = 102.4 V_A/\Omega_H$. When the particles moves in the magnetic field which is not change in time, the magnetic momentum

$$\mu = \frac{mv_\perp^2/2}{B} \tag{2.38}$$

is constant. The time evolution of the value of $\mu$ is shown in Figure 2.6b. We can confirm that the magnetic momentum do not change in the simulation model.

We assume the wave excitation at the equator ($x = 0$) for the test simulation of the wave propagation. Only cold ions, $H^+$, $He^+$, and $O^+$, are assumed. When a linearly polarized current source with a fixed frequency is used, both R-mode and L-mode EMIC waves are excited as shown in Figure 2.7a. The R-mode (right-handed polarized) wave has a smaller wavelength than that of the L-mode wave, and thus we can find these waves separately in Figure 2.7a. Since the R-mode wave has a larger group velocity than that of the L-mode EMIC wave, the simulation space is filled with the R-mode wave, which induces thermal fluctuations of energetic particles, disturbing the subsequent L-mode wave. To obtain a coherent monochromatic L-mode EMIC wave without the R-mode wave, we need to use a left-handed polarized current source. The current source is modeled by five grid points around the equatorial region and we specify both frequency and wavenumber of the triggering waves. To suppress an initial response of the magnetic field to the source current, we increase the magnitude of the current gradually in time. As shown in Figure 2.7b, monochromatic L-mode EMIC waves propagate away from the source current without foregoing R-mode waves.
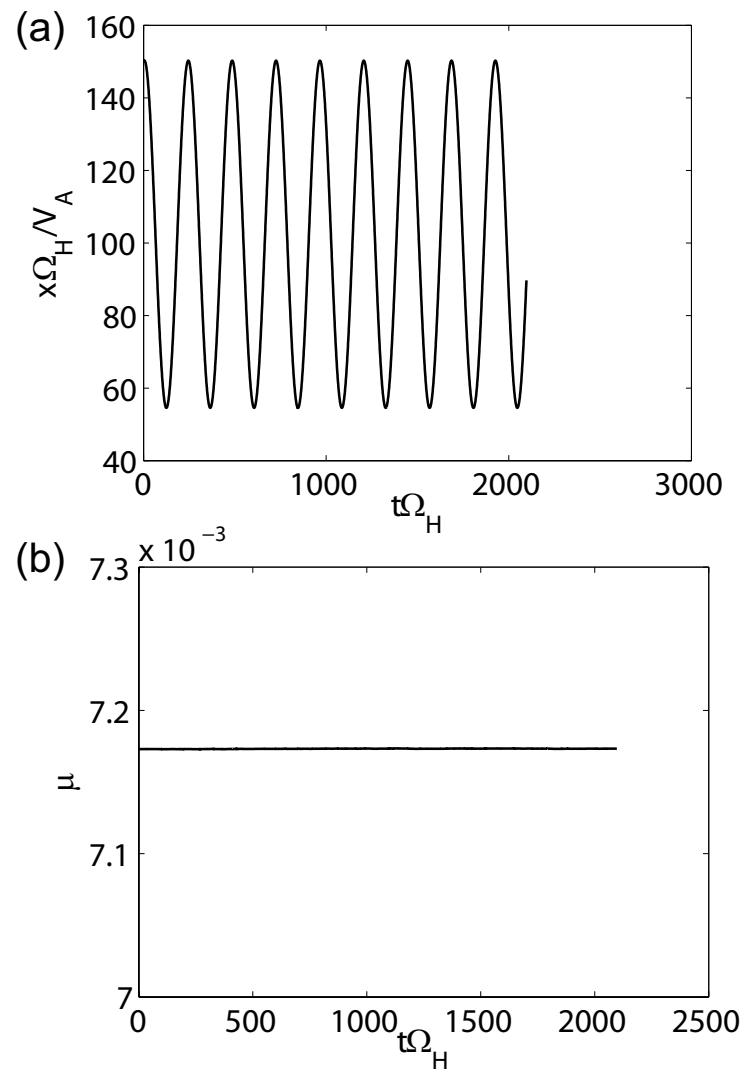
Figure 2.6: (a) Trajectory $x$ of a particle in the cylindrical parabolic background magnetic field. (b) Time evolution of the magnetic momentum $\mu$ of the particle.
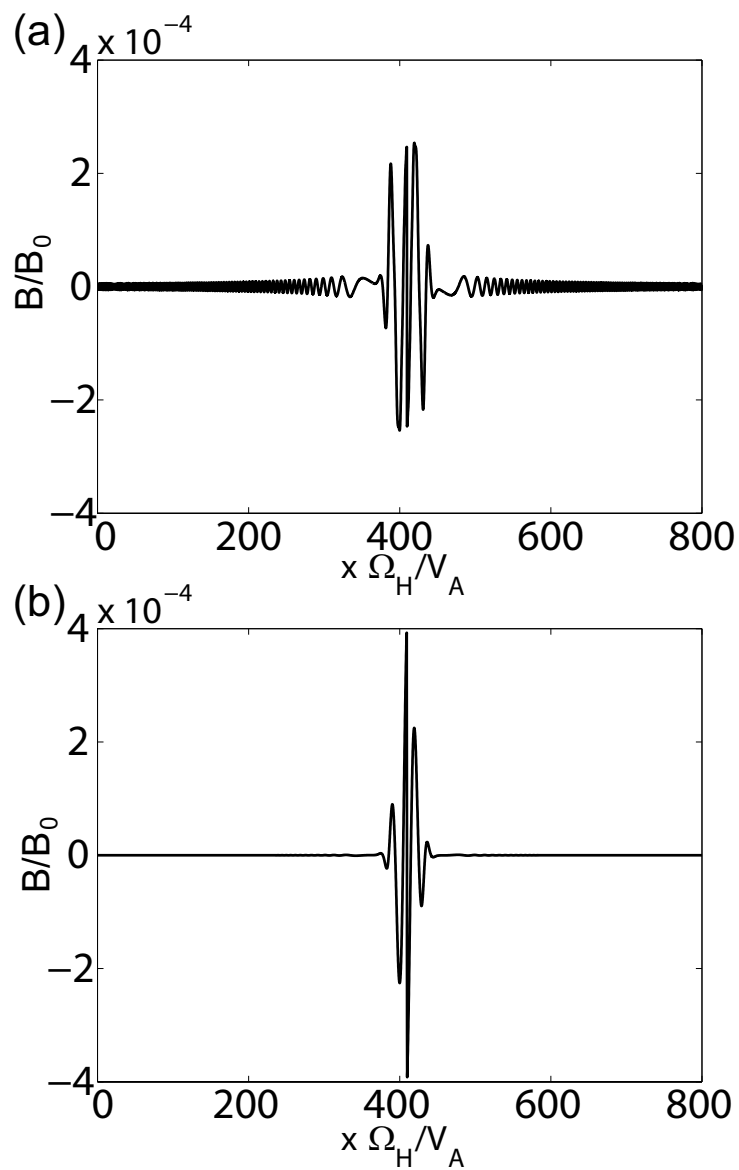
Figure 2.7: Waveforms of the test simulations with (a) a linear polarized current source and (b) a left-handed polarized current source.

# Chapter 3

# Competing Processes between Mirror and EMIC Instabilities in the Earth's Magnetosheath

## 3.1 Introduction

Large perpendicular-to-parallel ion temperature anisotropy ratios ($T_\perp/T_\parallel > 1$) can be expected at two regions in planetary magnetosheaths: downstream of the quasi-perpendicular portion of the bow shocks (see Figure 3.1) and close to the magnetopause where field-line draping effects are important [*Midgeley and Davis*, 1963; *Zwan and Wolf*, 1976]. In the former region, preferential plasma heating in $T_\perp$ takes place due to shock compression [*Kennel et al.*, 1985], and in the second region the anisotropy is caused by flow of plasma with high $V_\parallel$ out the ends of the magnetic flux tubes.

As we introduced in Chapter 1, these ion anisotropies can lead to two different instabilities, the mirror mode [*Chandrasekhar et al.*, 1958; *Hasegawa*, 1969, 1975] and the EMIC instability [*Kennel and Petschek*, 1966]. Of the two instabilities, the L-mode EMIC instability is dominant for low ion betas whereas the mirror mode is dominant for high ion betas [*Lacombe and Belmont*, 1995]. With ISEE-1 and -2 magnetic field and plasma data, *Tsurutani et al.* [1982] first established the existence of the mirror mode in the magnetosheath of the Earth, and with Pioneer 10 and 11 magnetic field data, in the magnetosheaths of Jupiter and Saturn.

Since the initial confirmation of the existence of mirror modes in the Earth's magnetosheath, they have been detected throughout the heliosphere. They have been detected at comets Giacobini-Zinner [*Tsurutani et al.*, 1999] and Halley [*Russell et al.*, 1989; *Glassmeier et al.*, 2003] as well as in interplanetary space proper [*Tsurutani et al.*, 1992]. More recent confirmatory magnetosheath observations at Earth are found in *Tsurutani et al.* [1984], *Hubert* [1994], *Phan et al.* [1994], and *Lacombe and Belmont* [1995], at Jupiter
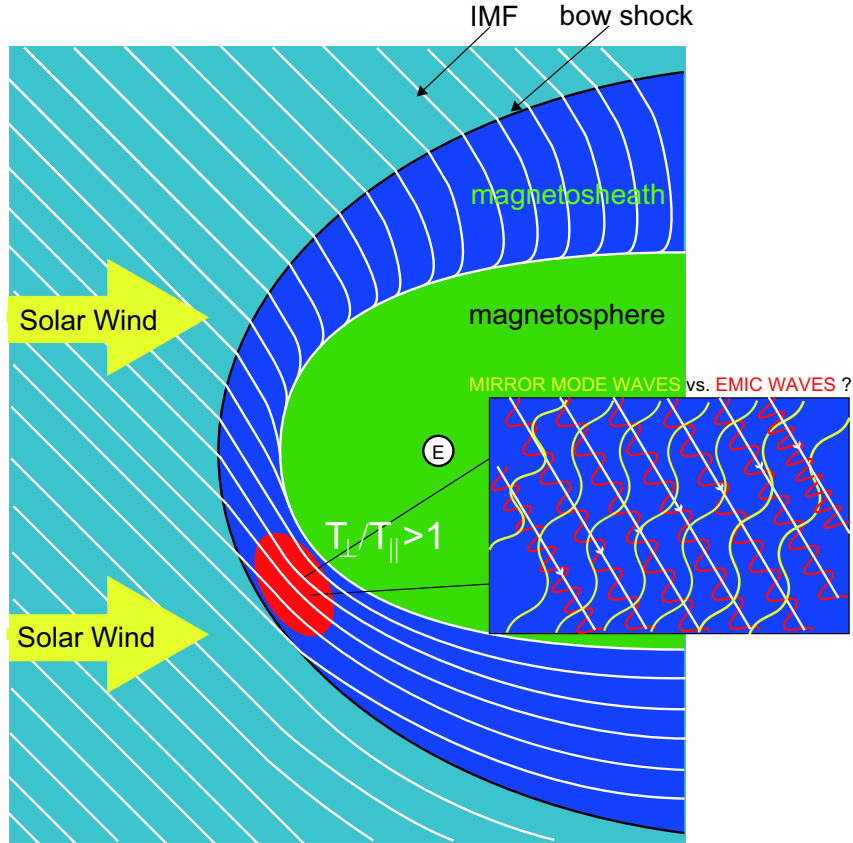
Figure 3.1: The schematic illustration of the magnetosphere of the Earth. The white lines show the interplanetary magnetic field (IMF).

and Saturn are in *Tsurutani et al.* [1993], *Bavassano et al.* [1998], *Violante et al.* [1995], *Erdos and Balogh* [1996], and *Joy et al.,* [2006]. These observations that mirror modes are often dominant coherent magnetic structures in planetary magnetosheaths even for low betas is a long-standing puzzle in space plasmas.

The presence of $He^{++}$ tends to increase the EMIC threshold [*Price et al.*, 1986]. On the other hand, the mirror mode growth is less affected by the presence of $He^{++}$ ions [*Brinca and Tsurutani*, 1989]. Thus *Gary* [1992] and *Gary et al.* [1993] have argued that this mechanism of lowering the EMIC linear growth rate is a possible cause of mirror mode formation and domination in planetary magnetosheaths.

The purpose of this chapter is to try another approach to the problem. In section 3.2, we perform linear analyses of the linear growth rate of each instability. We show that the linear growth rate of the EMIC modes is indeed higher than that of the mirror mode, in agreement with previously published results. In section 3.3, using 2D and 3D hybrid codes, we compare wave energy growth rates of both the mirror and EMIC modes

in the growth phase. In both cases, only a hydrogen plasma is assumed, removing any possible ambiguities associated with multiple ion effects. The results indicate a principal difference between 2D and 3D approaches and show that the free energy flows mostly into the mirror mode. In section 3.4, we discuss the long time evolutions of the L-mode EMIC waves and the mirror mode waves. The difference of the evolution of each wave also makes the mirror instability dominant. In section 3.5, the heating mechanism of the ions in the model is analyzed. Finally, in section 3.6, we conclude this chapter.

# 3.2 Linear Analyses
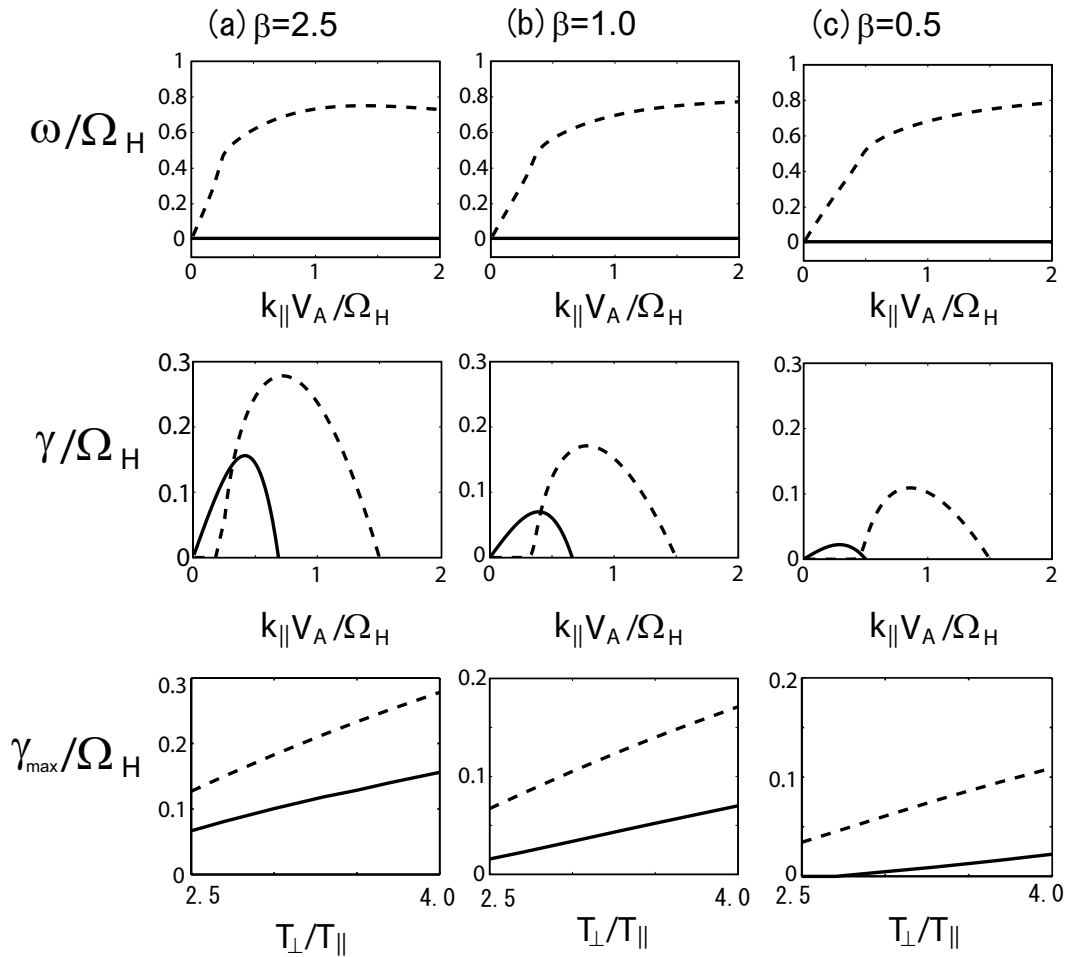


Figure 3.2: The linear analysis of each mode. The upper panels show the $\omega$-$k$ diagram of the L-mode EMIC waves (dashed line) and the mirror mode waves (solid line) for different ion $\beta$. The center panels show the growth rate of each mode. The temperature anisotropy of ions in these panels is 3.3. The lower panels show the maximum growth rate of each mode as a function of the temperature anisotropy for a constant value $\beta$.

We calculate theoretical growth rates of instabilities by solving the kinetic plasma dispersion relation $H(\boldsymbol{k}, \omega) = 0$, that is,

$$
\begin{vmatrix}
k_x^2 - k^2 + \dfrac{\omega^2}{c^2} - i\mu_0\omega\sigma_{xx} & k_xk_y - i\mu_0\omega\sigma_{xy} & k_zk_x - i\mu_0\omega\sigma_{xz} \\[2mm]
k_yk_x - i\mu_0\omega\sigma_{yx} & k_y^2 - k^2 + \dfrac{\omega^2}{c^2} - i\mu_0\omega\sigma_{yy} & k_yk_z - i\mu_0\omega\sigma_{yz} \\[2mm]
k_zk_x - i\mu_0\omega\sigma_{zx} & k_yk_z - i\mu_0\omega\sigma_{zy} & k_z^2 - k_x^2 + \dfrac{\omega^2}{c^2} - i\mu_0\omega\sigma_{zz}
\end{vmatrix} = 0, \quad (3.1)
$$

where $\boldsymbol{k} = (k_x, k_y, k_z)$ is a wavenumber vector consisting of orthogonal components $k_\parallel, k_\perp$, (parallel and perpendicular), $\omega$ is a complex frequency of each mode and $[\sigma_{jk}]$ ($j, k = x, y, z$) is the conductivity tensor. The imaginary part of $\omega$ is the linear growth rate. We assume bi-Maxwellian velocity distributions as functions of $v_\parallel$ and $v_\perp$, parallel and perpendicular to the static magnetic field, respectively, for $H^+$ defined by

$$
f_H(v_\parallel, v_\perp) = \frac{n_H}{(2\pi)^{3/2}V_{\parallel H}V_{\perp H}^2} \exp\left(-\frac{v_\parallel^2}{2V_{\parallel H}^2} - \frac{v_\perp^2}{2V_{\perp H}^2}\right), \tag{3.2}
$$

where $n_H$ is the density of proton, $v_\parallel$ and $v_\perp$ are velocities parallel and perpendicular to the static magnetic field, respectively. The thermal velocities of ions are given by $V_{\parallel H} = \sqrt{T_{\parallel H}/m}$, $V_{\perp H} = \sqrt{T_{\perp H}/m_H}$, where $T_{\parallel H}$ and $T_{\perp H}$ are temperatures of the protons in the parallel and perpendicular directions, respectively, and $m_H$ is the mass of proton. The plasma frequency of proton is $\omega_{pH} = 300\Omega_H$, where $\Omega_H$ is the cyclotron frequency of protons. The temperature anisotropy of ions are varied over the range of $2.5 \leqq T_{\perp H}/T_{\parallel H} \leqq 4.0$ and the different ion beta values of protons are 0.5, 1.0 or 2.5. We assume the electron beta value $\beta e = 1.0$.

The upper panels of Figure 3.2 show the $\omega$-$k_\parallel$ diagrams of the L-mode EMIC waves (dashed line) and the mirror mode waves (solid line) for different ion $\beta$ values (2.5, 1.0 and 0.5). The middle panels show the growth rate of each mode for a temperature anisotropy of ions $T_\perp/T_\parallel = 4.0$. The bottom panels show the maximum growth rate of each mode for various temperature anisotropies. In all cases, the maximum growth rate of L-mode EMIC waves is higher than that of mirror mode wave. Therefore, the fastest growing mode of the EMIC instability can initially grow faster than that of the mirror instability driven by the temperature anisotropy. We note that, however, the growth rate does not correspond directly to the increase of the total energy of each mode.

## 3.3 Comparison Between Multi-Dimensional Simulation Results

### 3.3.1 Simulation parameters

The bi-maxwellian protons are uniformly distributed in the simulation space. The number of the superparticles in the simulation is $N_p = 2^{31}$, the charge to mass ratio is $q_\mathrm{s}/m_\mathrm{s} = 1.0$, the plasma frequency of proton is $\omega_\mathrm{pH}/\Omega_\mathrm{H} = 300$. The thermal speeds of protons in the parallel and perpendicular directions are $V_{\parallel\mathrm{H}}/V_\mathrm{A} = 0.7070$ and $V_{\perp\mathrm{H}}/V_\mathrm{A} = 1.4140$, respectively, where $V_A$ is the Alfven velocity of protons. Thus, the temperature anisotropy is $T_\perp/T_\parallel = 4.0$ and the ion beta in the parallel direction is

$$\beta_{\parallel\mathrm{H}} = \frac{nmV_{\parallel\mathrm{H}}^2/2}{B_0^2/(2\mu_0)} = 0.5, \tag{3.3}$$

where $\mu_0$ is the permeability in vacuum. The maximum growth rate of the L-mode EMIC instability and the mirror instability is then 0.28 and 0.16 as shown in Figure 5.3, respectively. These ion parameters are the same in the three different simulation models. In the Earth's magnetosheath, the temperature anisotropy and beta value of ions are inversely correlated in the range of $1.2 \leqq T_\perp/T_\parallel \leqq 5.0$ and $0.01 \leqq \beta_\parallel \leqq 10.0$ because of the regulation of the EMIC instability [*Fuselier et al.*, 1994]. These observations represents the results of the instability. In this study, we analyze the instabilities driven by the flesh injection of the anisotropic protons. Thus we initially assume a strong temperature anisotropy and a high beta value in a possible range of observation to drive both L-mode EMIC and mirror instabilities.

The simulation models have been introduced in Figure 2.2. A constant background magnetic field $\boldsymbol{B}_0$ is assumed in the $x$ direction. The electron beta is $\beta_\mathrm{e} = 1.0$. The grid spacing $\Delta x$ is $1.0V_\mathrm{A}/\Omega_\mathrm{H}$. The numbers of grid points $(n_x \times n_y \times n_z)$ are 512×512×512, 512×512×1, and 512×1×1 in the 3D, 2D, and 1D models respectively. The number of time steps is 3200 with $\Delta t = 0.04/\Omega_\mathrm{H}$. Periodic boundary is used in each dimension.

### 3.3.2 Competing process in the linear stage

Figures 3.3a and 3.3b show the time histories of the L-mode EMIC waves and the mirror mode waves at $m_x = 41$, $m_y = 1$, $m_z = 1$ and $m_x = 33$, $m_y = 40$, $m_z = 1$, respectively, where $m_j$ $(j = x,\ y,\ z)$ is the mode number in each direction. The growth rates of each wave have good agreement with those given by the kinetic linear theories (dashed lines) in the simulation models. The L-mode EMIC waves initially grow faster than the mirror mode waves.
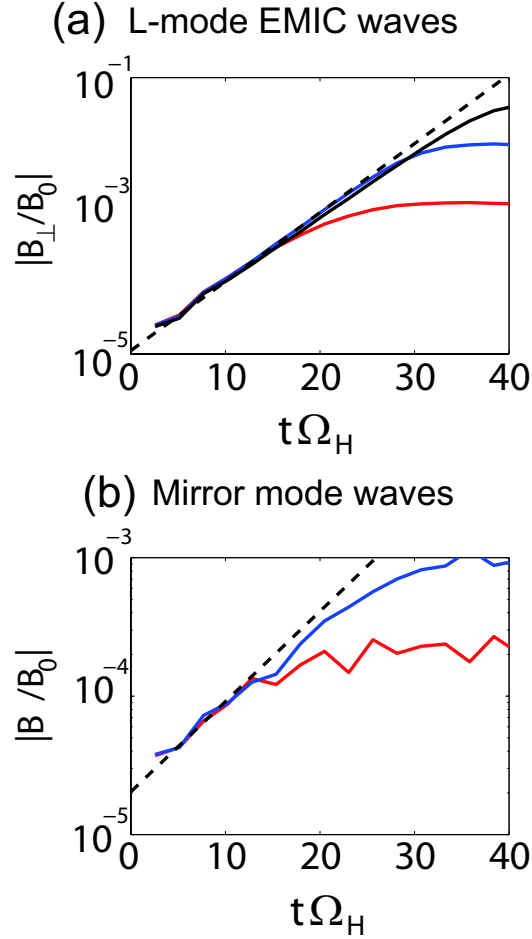
Figure 3.3: (a) The effect of mirror instability on the saturation levels of the L-mode EMIC waves at $m_x = 41$, $m_y = 1$, $m_z = 1$. (b) The saturation levels of the mirror mode waves at $m_x = 33$, $m_y = 40$, $m_z = 1$. In each panel, the black, blue, and red lines show the saturation level in the 1D, 2D, and 3D models, respectively, and the dashed black lines show the theoretical growth rate of each mode at the initial phase.

In Figure 3.3a, the effect of the mirror mode waves on the saturation levels of the L-mode EMIC waves is also shown. The initial linear growth rates of the L-mode EMIC waves are the same in all simulation models. As we discuss later in section 3.6, the growth of the mirror mode waves relaxes the temperature anisotropy of protons more effectively in the 3D model than in the 2D model. As the spatial dimension increases, the available free energy for the L-mode EMIC instability are lost faster to the mirror mode waves, and the growth time becomes shorter. Therefore, the saturation levels of the L-mode EMIC waves are very different in these two simulation models. Indeed, in the 3D model, the mirror mode and L-mode EMIC waves have similar amplitudes for these parameters, whereas in 1D or 2D the L-mode EMIC waves dominate the mirror mode by over one

order of magnitude in amplitude.
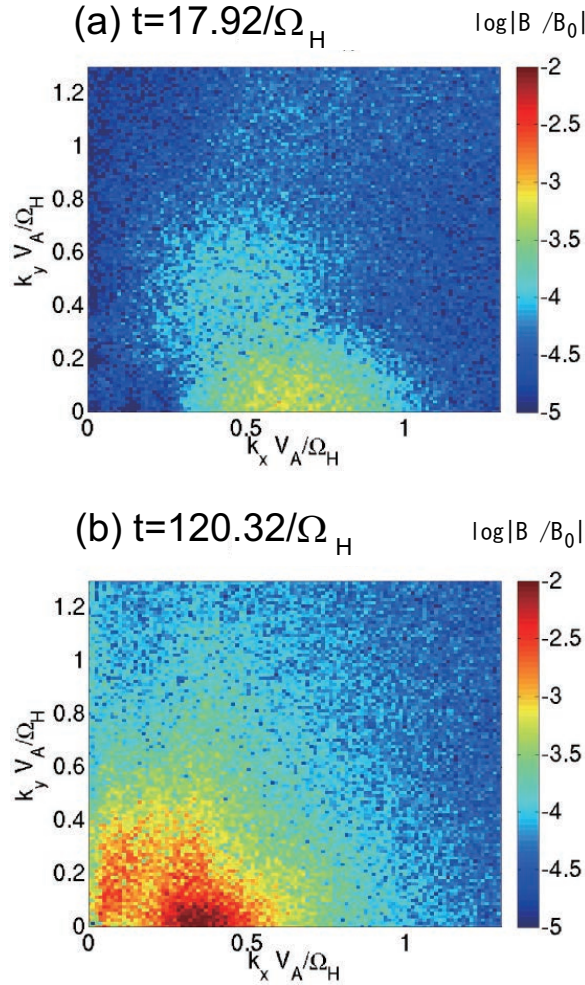


Figure 3.4: The spectrum of $B/B_0$ in the log scale in the 2D model. (a) $t = 17.92/\Omega_H$ in the linear stage. (b) $t = 120.32/\Omega_H$ in the nonlinear stage.

The spectrum of $|\boldsymbol{B}/B_0|$ in the log scale in the 2D and 3D models at $t = t_1 = 17.92/\Omega_H$ are shown in Figures 3.4a and 3.5a, respectively. In Figure 3.5, the left and center panels are the spectrum for $m_z = 1$ and $m_x = 26$ (which correspond to $k_z = 0V_A/\Omega_H$ and $k_x = 0.30V_A/\Omega_H$) planes, respectively. The right panel is a schematic drawing of the spectrum in the 3D wavenumber space. In the wavenumber vector space of both models, note the mirror mode waves excited at oblique angles and the L-mode EMIC waves excited mostly in the direction parallel to $\boldsymbol{B}_0$. In Figures 3.4a and the left panel of 3.5a, the L-mode EMIC waves are excited faster than the mirror mode waves. The spectrum of L-mode EMIC waves is much stronger than that of mirror mode waves, especially in 2D model. This is because the growth rate of the L-mode EMIC wave is higher than that of
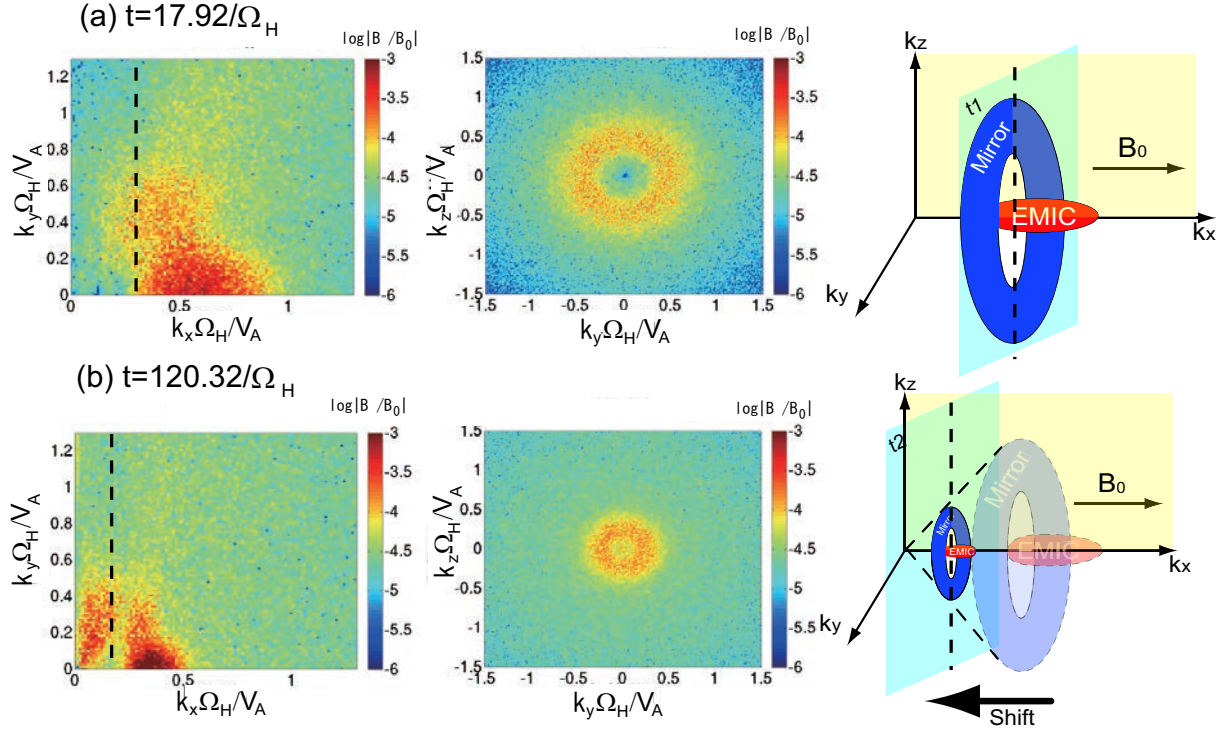
Figure 3.5: The spectrum of $B/B_0$ in the log scale in the 3D model with a schematic drawing. (a) $t = 17.92/\Omega_H$ in the linear stage. (b) $t = 120.32/\Omega_H$ in the nonlinear stage.

the mirror mode wave. The mirror mode waves, on the other hand, grow slowly in oblique directions in both models. Because of symmetry, the spectrum of the mirror mode waves spreads in all perpendicular direction as shown in the center panel of Figure 3.5a. All of the cross sections of the wavenumber space including $x$-axis are the same. Therefore, the mirror mode waves in the wavenumber space form a torus-like structure shown in the right panel of Figure 3.5a. In this panel, the center structure is the L-mode EMIC waves and the surrounding structures are the mirror mode waves.

We identify the magnetic energy density of each wave by the following method and plot its time history in Figure 3.6. Examination of the wave spectra shows that the L-mode EMIC waves and mirror mode waves are separated by the angle $\theta = 30°$ between the wavenumber vector $\boldsymbol{k}$ and $\boldsymbol{B}_0$. Accordingly, we define the "L-mode EMIC wave range" to be $0° \leqq \theta \leqq 30°$, and the "mirror mode wave range" to be $30° < \theta \leqq 80°$. We divide the spectra of the magnetic field into these two ranges of the wavenumber vector space, and integrate the value of $|\boldsymbol{B}(\boldsymbol{k})/B_0|^2/2$ in each range. Figures 3.6a and 3.6b show results of the 2D and 3D simulations, respectively.

We find a clear difference in the saturation levels of the L-mode EMIC and mirror instabilities in the 2D and 3D models. In the 2D model, shown in Figure 3.6a, the

magnetic energy density of the L-mode EMIC waves attains a larger value than that of the mirror mode waves. This is caused by the L-mode linear growth rate being larger than that of the mirror mode waves. In the 3D model shown in Figure 3.6b, however, the mirror mode waves gains larger free energy than the L-mode EMIC wave. In the oblique direction region the mirror mode waves can exist over a wider range of the wavenumbers because the degree of freedom of the wavenumber vector space increases because of another perpendicular direction $k_z$. In the 2D model, the structures are uniform in the $k_z$ direction, while in the 3D model the wavenumber vectors of the mirror mode waves form the torus-like structure shown in the right panel of Figure 3.5a. As a result, the mirror mode waves gain more free energy than L-mode EMIC wave, even thought the linear growth rate is still smaller than that for the L-mode EMIC wave.
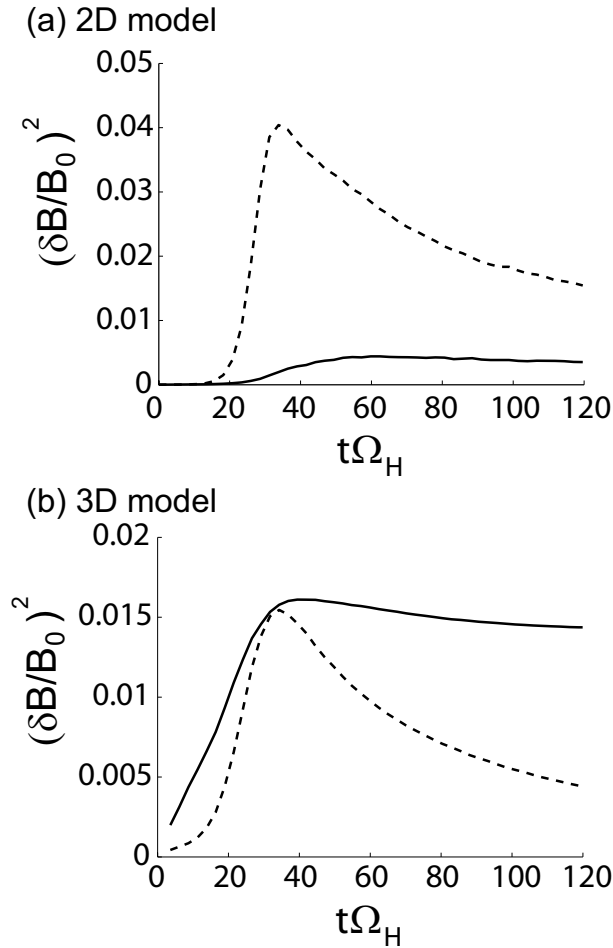


Figure 3.6: Time evolution of the magnetic energy density of the L-mode EMIC waves and the mirror mode waves in the (a) 2D and (b) 3D model. The dashed line shows the energy of the L-mode EMIC waves, and the solid line shows that of the mirror mode waves.

### 3.3.3 Dependency on initial fluctuations

There is a possibility that the L-mode EMIC instability becomes dominant although the mirror instability obtains the geometrical 3D advantage, as we have explained in the previous section. In much lower initial thermal noise case, the growth time of the L-mode EMIC waves becomes longer. As a result, the amplitude of the L-mode EMIC waves becomes larger than that in the higher noise case. In such extreme cases, the mirror instability will not dominate over the L-mode EMIC instability. We will calculate the each wave energy density and estimate the effect of initial thermal fluctuation on the competition below.

Calculating the Inverse Fourier Transform of (3.7), we obtain the wave form in the real space:

$$B_{\mathrm{M}\|}(\boldsymbol{x},\ t) = \frac{B_{\mathrm{M0}}}{(2\pi)^3} \int \delta(k_\| - k_{\|\mathrm{M}}) e^{ik_\| x} dk_\| \iint \delta(k_\perp - k_{\perp\mathrm{M}}) e^{i(yk_y + zk_z)} dk_y dk_z e^{\gamma_\mathrm{M} t}$$

$$= \frac{B_{\mathrm{M0}}}{(2\pi)^3} e^{ik_{\|\mathrm{M}} x + \gamma_\mathrm{M} t} \iint \delta(k_\perp - k_{\perp\mathrm{M}}) e^{i(yk_y + zk_z)} dk_y dk_z. \qquad (3.4)$$

We change the orthogonal coordinates to the polar coordinates, $(k_y,\ k_z) \mapsto (k_\perp,\ \phi)$, and then (3.4) is calculated as

$$B_{\mathrm{M}\|}(\boldsymbol{x},\ t) = \frac{B_{\mathrm{M0}}}{(2\pi)^3} e^{ik_{\|\mathrm{M}} x + \gamma_\mathrm{M} t} \iint \delta(k_\perp - k_{\perp\mathrm{M}}) e^{i(yk_\perp \cos\phi + zk_\perp \sin\phi)} k_\perp dk_\perp d\phi$$

$$= \frac{k_{\perp\mathrm{M}} B_{\mathrm{M0}}}{(2\pi)^3} e^{ik_{\|\mathrm{M}} x + \gamma_\mathrm{M} t} \int_0^{2\pi} e^{ik_{\perp\mathrm{M}}(y \cos\phi + z \sin\phi)} d\phi. \qquad (3.5)$$

The phase part in the integrated function is calculated as $y \cos\phi + z \sin\phi = \sqrt{y^2 + z^2} \cos(\phi + \phi_0)$, where $\phi_0 = \tan^{-1}(z/y)$ ($\tan^{-1} x$ is arctangent function). Therefore we obtain $B_{M\|}(\boldsymbol{x},\ t)$ in the 3D model as

$$B_{\mathrm{M}\|}(\boldsymbol{x},\ t) = \frac{k_{\perp\mathrm{M}} B_{\mathrm{M0}}}{(2\pi)^3} e^{ik_{\perp\mathrm{M}} x + \gamma_\mathrm{M} t} \int_0^{2\pi} e^{ik_{\perp\mathrm{M}} \sqrt{y^2 + z^2} \cos(\phi + \phi_0)} d\phi$$

$$= \frac{k_{\perp\mathrm{M}} B_{\mathrm{M0}}}{(2\pi)^2} J_0(k_{\perp\mathrm{M}} \sqrt{y^2 + z^2}) e^{\gamma_\mathrm{M} t + ik_{\|\mathrm{M}} x}, \qquad (3.6)$$

where $J_0(x)$ is the 0th order Bessel's function. The value of $\phi_0$ can be neglected because of the periodicity of the integrated function.

Since the time scale of the mirror instability is much slower than the cyclotron motion of protons, this phenomenon is gyrotropic and the spectrum in the wavenumber space becomes symmetric in the perpendicular plane. This is verified by the simulation result shown in Figure 3.5a. We assume a mirror mode wave which has only specified wavenumbers $(k_\|,\ k_\perp) = (k_{\|\mathrm{M}},\ k_{\perp\mathrm{M}})$; this forms a "ring" in the 3D wavenumber space. The parallel

component of the mirror mode wave is given by

$$B_{\mathrm{M}\|}(\boldsymbol{k},\ t) = B_{\mathrm{M}0}\delta(k_\| - k_{\|\mathrm{M}})\delta(k_\perp - k_{\perp\mathrm{M}})e^{\gamma_{\mathrm{M}}t}, \tag{3.7}$$

where $B_{\mathrm{M}0}$ is the initial thermal noise for the mirror mode wave, $k_\perp = \left(\sqrt{k_y^2 + k_z^2}\right)$ is the wavenumber in the perpendicular direction and $\delta(x)$ is Dirac's delta function.

By inverse Fourier transform, we obtain the wave amplitude in the real space:

$$B_{\mathrm{M}\|}(\boldsymbol{x},\ t) = \frac{k_{\perp\mathrm{M}}B_{\mathrm{M}0}}{(2\pi)^2}J_0(k_{\perp\mathrm{M}}\sqrt{y^2 + z^2})e^{ik_{\|\mathrm{M}}x + \gamma_{\mathrm{M}}t}, \tag{3.8}$$

where $J_0(x)$ is the 0th order Bessel's function. From $\boldsymbol{\nabla}\cdot\boldsymbol{B} = 0$, we obtain the perpendicular component of the mirror mode wave, $B_{\mathrm{M}\perp}$:

$$B_{\mathrm{M}\perp} = -\frac{k_{\|\mathrm{M}}}{k_{\perp\mathrm{M}}}B_{\mathrm{M}\|}. \tag{3.9}$$

We also obtain one of the transverse components of the L-mode EMIC wave at $(k_\|,\ k_\perp) = (k_{\|\mathrm{L}},\ 0)$ in the same manner:

$$B_{\mathrm{L}\perp}(\boldsymbol{x},\ t) = \frac{B_{\mathrm{L}0}}{(2\pi)^3}e^{i(k_{\|\mathrm{L}}x - \omega_{\mathrm{L}}t) + \gamma_{\mathrm{L}}t}, \tag{3.10}$$

where $B_{\mathrm{L}0}$ is the initial thermal noise for the L-mode EMIC wave.

We calculate variation of wave energy densities over the time period $\tau_g$ during which the both wave modes growth according to the linear growth rates. Since the total amplitude of the mirror mode wave $B_{\mathrm{M}}$ can be expressed by $B_{\mathrm{M}\|}$ as $B_{\mathrm{M}}^2 = B_{\mathrm{M}\perp}^2 + B_{\mathrm{M}\|}^2 = \left(1 + k_{\|\mathrm{M}}^2/k_{\perp\mathrm{M}}^2\right)B_{\mathrm{M}\|}^2$, we obtain the wave energy variation of the mirror mode wave:

$$\Delta\mathcal{E}_{\mathrm{M}} = \left\langle |B_{\mathrm{M}}(\boldsymbol{x},\ \tau_g)|^2 - |B_{\mathrm{M}}(\boldsymbol{x},\ 0)|^2 \right\rangle = \frac{B_{\mathrm{M}0}^2}{16\pi^3}(e^{2\gamma_{\mathrm{M}}\tau_g} - 1)\left(1 + \frac{k_{\|\mathrm{M}}^2}{k_{\perp\mathrm{M}}^2}\right)\int_0^{2\pi}J_0^2(p)p\,dp, \tag{3.11}$$

where $<x>$ shows the ensemble mean value of $x$ in the volume. On the other hand, the L-mode EMIC wave has two perpendicular components since it has the left-handed circular polarization. Thus, the total amplitude of the L-mode EMIC wave $B_{\mathrm{L}}$ can be expressed by $B_{\mathrm{L}\perp}$ as $B_{\mathrm{L}}^2 = B_{\mathrm{L}y}^2 + B_{\mathrm{L}z}^2 = 2B_{\mathrm{L}\perp}^2$. From (3.10), we calculate the wave energy of the L-mode EMIC wave:

$$\Delta\mathcal{E}_{\mathrm{L}} = \left\langle |B_{\mathrm{L}}(\boldsymbol{x},\ \tau_g)|^2 - |B_{\mathrm{L}}(\boldsymbol{x},\ 0)|^2 \right\rangle = \frac{B_{\mathrm{L}0}^2}{(2\pi)^6}(e^{2\gamma_{\mathrm{L}}\tau_g} - 1). \tag{3.12}$$

In the present simulation, at the end of the linear growing stage, we find that the energy of the mirror mode waves is larger than that of the L-mode EMIC waves. This is expressed

as $\Delta\mathcal{E}_M/\Delta\mathcal{E}_L > 1$. Substituting (3.11) and (3.12) into the inequality, we obtain the condition of the initial thermal fluctuations for the dominance of the mirror instability:

$$\left(\frac{B_{L0}}{B_{M0}}\right)^2 < 4\pi^3 \frac{e^{2\gamma_M\tau_g}-1}{e^{2\gamma_L\tau_g}-1}\left(1+\frac{k_{\parallel M}^2}{k_{\perp M}^2}\right)\int_0^{2\pi}J_0^2(p)pdp$$

$$\simeq 23.2\frac{e^{2\gamma_M\tau_g}-1}{e^{2\gamma_L\tau_g}-1}\left(1+\frac{k_{\parallel M}^2}{k_{\perp M}^2}\right). \tag{3.13}$$

Assuming $B_{M0} = B_{L0}$ and $e^{2\gamma t} \gg 1$, the value of $\tau_g$ should satisfy the condition (3.14):

$$\tau_g < \frac{\log(1+k_{\parallel M}^2/k_{\perp M}^2)+3.14}{2(\gamma_L-\gamma_M)}. \tag{3.14}$$

Substituting the simulation parameters, $\gamma_M = 0.16\Omega_H$, $\gamma_L = 0.28\Omega_H$, $k_{\perp M}/k_{\parallel M} = \tan 50°$, into (3.14), we obtain the condition for the dominance of the mirror instability:

$$\tau_g < 16.8/\Omega_H. \tag{3.15}$$

From Figure 3.3, we confirm that the value of $\tau_g$ in the simulation satisfies this condition. Assuming $\tau_g\Omega_H \gg 1$, we rewrite (3.13) as

$$\frac{B_{L0}}{B_{M0}} < 7.49e^{-(\gamma_L-\gamma_M)\tau_g}. \tag{3.16}$$

If the initial fluctuations can satisfy this condition, the mirror mode wave can gain more free energy than the L-mode EMIC wave, even though $\gamma_L$ is larger than $\gamma_M$. In an extreme case that $B_{L0}$ is much larger than $B_{M0}$, the L-mode EMIC instability will dominate over the mirror instability. However, the realistic conditions $B_{M0} \sim B_{L0}$ and $(\gamma_L - \gamma_M)\tau_g < 2$ result in the dominance of the mirror mode wave.

### 3.3.4   Effect of alpha particles

In the solar wind, the helium ions $He^{++}$ are also included. Although the amount of the alpha particles is only few %, they also play an important role in the competing process. We perform the 3D simulation which includes the $He^{++}$ ions to show the contribution of the alpha particles. The same parameters for the protons, and the simulation space are used. In this model, we assume the $He^{++}$ ions with the density $n_{He}/n_H = 0.04$. The number of $He^{++}$ particles in a cell is 16. The temperature in each direction of $He^{++}$ are the same as the protons. The charge-to-mass ratio is $(q/m)_{He} = 0.5$, and thus the thermal velocities in the parallel and perpendicular directions are $V_\parallel = 0.707V_A$ and $V_\perp = 0.3535V_A$, respectively.

Figure 3.7 shows the averaged magnetic field energy density in the simulation space. We show the result in this model in which the alpha particles are assumed by the red
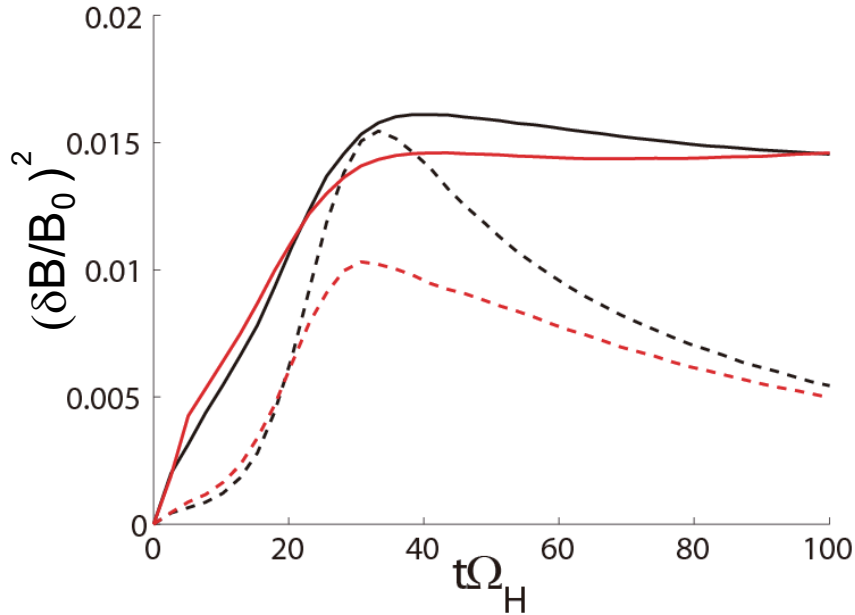
Figure 3.7: The time evolutions of the energy density of the magnetic field of each wave. The solid lines show the energy density of the mirror mode waves, and the dashed lines show that of the L-mode EMIC waves. The red lines show the results in the models that the heliums are included model, and the black lines show the results in the proton model (same as Figure 3.6).

lines. Comparing with the previous result (black lines), in which we only assumed the protons, we find that the L-mode EMIC waves saturate at lower levels than that in the previous model (shown by the black lines in Figure 3.7). This is due to the increase of the threshold of the L-mode EMIC instability [*Price et al.*, 1986]. The heating of heavy ions also takes place by the nonlinear potentials generated by the forward and backward propagating waves [*Omura et al.,* 1988], which we discuss in later section, the linear growth stops at earlier time. On the other hand, the mirror instability is also affected by the alpha particles. The saturation level becomes slightly lower, due to the trapping of the heavy ions which have smaller thermal velocity in the parallel direction. Therefore, as the previous studies [*Gary*, 1992; *Gary et al.*, 1993] have argued, the mechanism of lowering the EMIC linear growth rate can be also cause of mirror mode formation and domination in planetary magnetosheaths.

## 3.4 Long Time Evolutions of Each Wave

When the amplitude of the waves exceed a certain level, we should consider the nonlinear term of the Lorentz force. Thus, we define the nonlinear evolution stage as the time when

the nonlinear term dominates over the linear term. At this stage, the wave amplitude saturates at a certain level. In this section, we analyze the nonlinear evolution of the L-mode EMIC (section 3.4.1) and mirror (section 3.4.2) instabilities.

## 3.4.1 Long time evolution of the L-mode EMIC waves

The mirror mode instability in the 3D model effectively diffuse the temperature anisotropy as we discuss in section 3.6. It makes the linear growth rates and wavenumbers of L-mode EMIC waves smaller than those in the 2D model before the end of the growth phase. The L-mode EMIC waves still grow as we can see in Figure 3.3a (around $20/\Omega_H < t < 30/\Omega_H$). When the amplitude of the L-mode EMIC waves reaches a sufficient level, the forward and backward propagating waves form a nonlinear static potential $\Phi$ which is produced by the $\boldsymbol{v}_\perp \times \boldsymbol{B}_\perp$ term [*Omura et al.*, 1988; *Omura*, 1991]. It can be expressed as

$$\Phi = \frac{m}{q}\left(\frac{\Omega_H}{k}\frac{B_{L\perp}}{B_0}\right)^2 \frac{\omega}{\Omega_H - \omega}\cos(2kx + \theta_0), \tag{3.17}$$

where, $\theta_0$ is the phase at $x = 0$. Because of particle trapping by this nonlinear potentials, the energy of the L-mode EMIC waves is transferred to the protons kinetic energy. Figure 3.8 shows the velocity distribution function of the protons at the initial time and the saturation time. We find heating of the whole proton distribution function which is caused by the nonlinear trapping.

We also note that there is another nonlinear effect of the L-mode EMIC waves. As we can see in Figure 3.4b and the left panel of Figure 3.5b, which show the spectra at $t = t_2 = 120.32/\Omega_H$, the spectrum of the L-mode EMIC waves in the 2D and 3D models shifts to lower wavenumbers. This transfer of the energy from higher wavenumbers to lower wavenumbers is due to a nonlinear effect. To show details of the nonlinear evolution of the L-mode EMIC waves, we focused on the spectra of the electric and magnetic fields at $k_y = k_z = 0$. Figure 3.9 shows $\log|B_\perp(k_x, t)/B_0|$ and $\log|E_\parallel/(V_A B_0)|$ in the 1D, 2D and 3D models. The $B_\perp(k_x,t)$ component and $E_\parallel(k_x,t)$ component include only the L-mode EMIC wave and acoustic wave, respectively. In the initial stage the L-mode EMIC waves are excited and there is no $E_\parallel(k_x,t)$ component because the L-mode EMIC wave is a purely transverse wave. After linear growth, the spectrum of the dominant L-mode EMIC waves starts to shift to lower wavenumber vectors, and the acoustic wave is generated at higher wavenumbers than the $B_\perp(k_x,t)$ component, and it also shifts to the lower wavenumbers. Although the growth rate of the EMIC instability decreases, the EMIC waves still grow to a sufficient amplitude that induces the parallel heating of resonant protons by the nonlinear potentials and the inverse cascading process. These nonlinear processes terminate the growth of the EMIC waves.
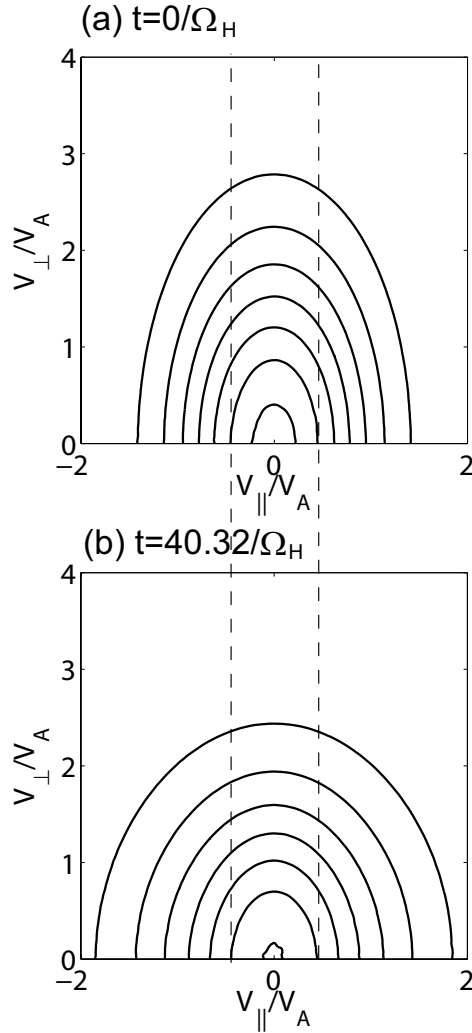
Figure 3.8: Velocity distribution function of protons in the 3D model (a) at $t = 0$ and (b) at $t = 40.32/\Omega_{\mathrm{H}}$. The dashed lines show the resonance velocity of protons for the fastest growing mode of EMIC waves.

Figures 3.10a and 3.10b show the dispersion relations ($\omega$-$k_x$ diagram) of the L-mode EMIC waves during $0 < t < 25.6/\Omega_{\mathrm{H}}$ and the ion acoustic waves during $25.6/\Omega_{\mathrm{H}} < t < 51.2/\Omega_{\mathrm{H}}$, respectively. The white curve in Figure 3.10a is the dispersion relation that we obtained by linear analysis (See section 2). Because we use a Fourier transform for a short time interval, the spectrum obtained by the simulation is broad in frequency. There are forward and backward propagating L-mode EMIC waves present. We choose one each of the forward and backward propagating waves, and show them by red arrows. These two waves and the parallel propagating ion acoustic waves (which are shown by the yellow arrow), satisfy momentum and energy conservation relations (3.18) and (3.19) in *Sagdeev*
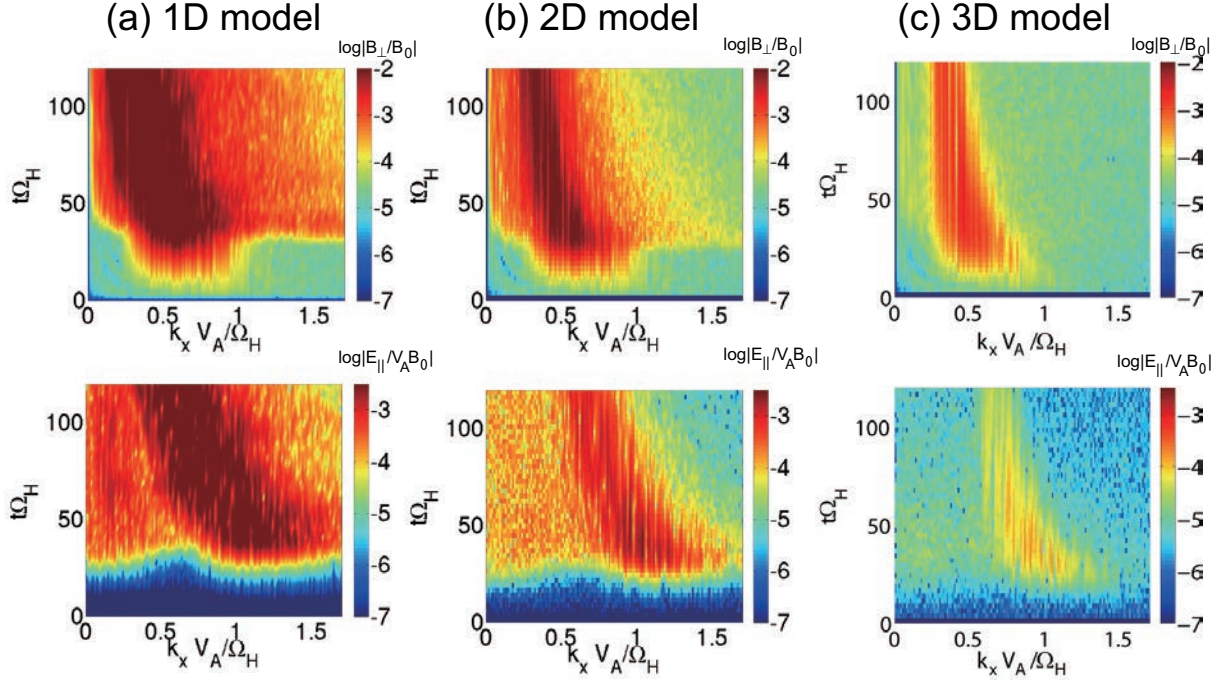
Figure 3.9: The spectra of $\boldsymbol{B}_\perp(k_x,\ t)/B_0$ (EMIC wave) and $\boldsymbol{E}_\parallel(k_x,\ t)/(B_0 V_A)$ (acoustic wave) in the log scale in the (a) 1D, (b) 2D, and (c) 3D models.

and Galeev [1969] and Terasawa and Hoshino [1986].

$$k_f = -k_b + k_{ia} \tag{3.18}$$

$$\omega_f = -\omega_b + \omega_{ia} \tag{3.19}$$

In the above $(k_f,\ \omega_f)$ and $(k_b,\ \omega_b)$ are sets of the wavenumber and the frequency for the forward and backward propagating L-mode EMIC wave, respectively, and $(k_{ia},\ \omega_{ia})$ is the same for the ion acoustic wave. These three points and the origin $(0,\ 0)$ form a parallelogram in the $\omega$-$k_x$ diagram. In this three-wave coupling process, the energy of the forward propagating mode is converted to the backward propagating mode and the ion acoustic mode. Because of the symmetry of the simulation space, the same nonlinear process takes place in the opposite direction. This means that we have another parallelogram with the backward propagating mode. The phase velocity of the ion acoustic wave is given as

$$\frac{\omega_{ia}}{k_{ia}} = \frac{\omega_f - \omega_b}{k_f + k_b} \simeq 0.1 \ll V_{\parallel H}, \tag{3.20}$$

and thus the energy of the ion acoustic mode is effectively used to heat the protons. The L-mode EMIC waves lose their energy and their spectra cascade to lower wavenumbers. Figure 3.10c shows the dispersion relation computed in the range of $25.6/\Omega_H < t <$

$51.2/\Omega_{\mathrm{H}}$. The red arrows in this panel indicates the forward and the generated backward propagating waves.

Figure 3.11 shows further evidence for the nonlinear effect on the L-mode EMIC waves. Red lines and blue lines show the amplitude of the L-mode EMIC waves at the higher and lower wavenumber, respectively. Initially, the higher modes grows linearly in each model. In the 2D model, after the higher modes stop growing, they start to decrease and the lower modes start to grow. Therefore, shift of the spectrum of L-mode EMIC waves are mainly caused by the nonlinear effect in the 2D model. On the other hand, in the 3D model, one of the lower modes ($m_x = 21$) initially grows slowly in the initial time and another one starts to grow after the higher modes saturate. This means the linear effect and the nonlinear effect coexist in the 3D model. The shift of the spectrum is caused by these factors. The magnetic field energy of L-mode EMIC waves takes the maximum value and subsequently decreases to a constant level in both 2D and 3D models.

## 3.4.2   Long time evolution of the mirror mode structures

Since protons are heated in the parallel direction by the nonlinear evolutions of the L-mode EMIC waves, the temperature anisotropy reaches the threshold of the mirror instability, and thus the mirror mode waves stop growing. In Figures 3.4b and the left panel of Figure 3.5b, we can find that the wavenumbers of the excited mirror mode waves also change in wavenumber space in both models. The energy of the magnetic field that exists in the large wavenumber modes is transferred to smaller wavenumber modes. In the 3D model, this means the torus-like structure in the wavenumber space changes its form to the smaller one in the lower wavenunber as shown in the right panel of Figure 3.5b.

In Figure 3.12, which shows the time evolution of $B_{\parallel}$ at $t\Omega_{\mathrm{H}} = 17.92$, 30.72, 43.52, and 120.32, we find clear formation of magnetic structures of the mirror mode waves in both 2D and 3D models. In these panels, the color bar is tuned to show the clear structures. The actual maximum values of the amplitude are 0.31 and 0.63 in the 2D and 3D models, respectively. It is noted that the L-mode EMIC waves do not have the parallel component of the magnetic field. Since there are no $k_z$ component of the wavenumber vector in the 2D model, stripes of magnetic structures are formed. In the 3D model, the mirror mode structures are different from those in the 2D model because of the third dimension. In both 2D and 3D models, the mirror mode waves remain as larger structures at the end of the simulations ($t = t_2$).

As we can see in Figure 3.6b, the energy of the mirror mode waves does not decrease as much as in the case of the L-mode EMIC waves. This means coalescence of the mirror mode waves does not contribute to the heating of protons in the nonlinear stage. Then,
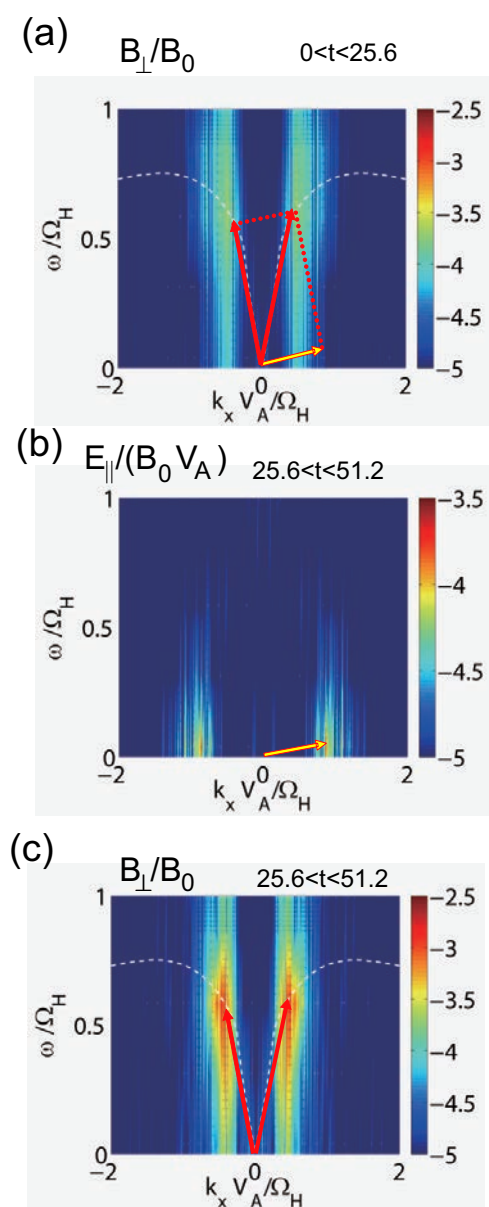
Figure 3.10: The dispersion relation ($\omega$-$k_\parallel$ diagram) of the L-mode EMIC waves. at (a) $0 < t\Omega_{\mathrm{H}} < 25.6$ and at (c) $25.6 < t\Omega_{\mathrm{H}} < 51.2$, and that of the ion acoustic waves at (b) $25.6 < t\Omega_{\mathrm{H}} < 51.2$. The red arrows show forward and backward propagating L-mode EMIC waves, respectively. The yellow arrow indicates a forward propagating ion acoustic wave.
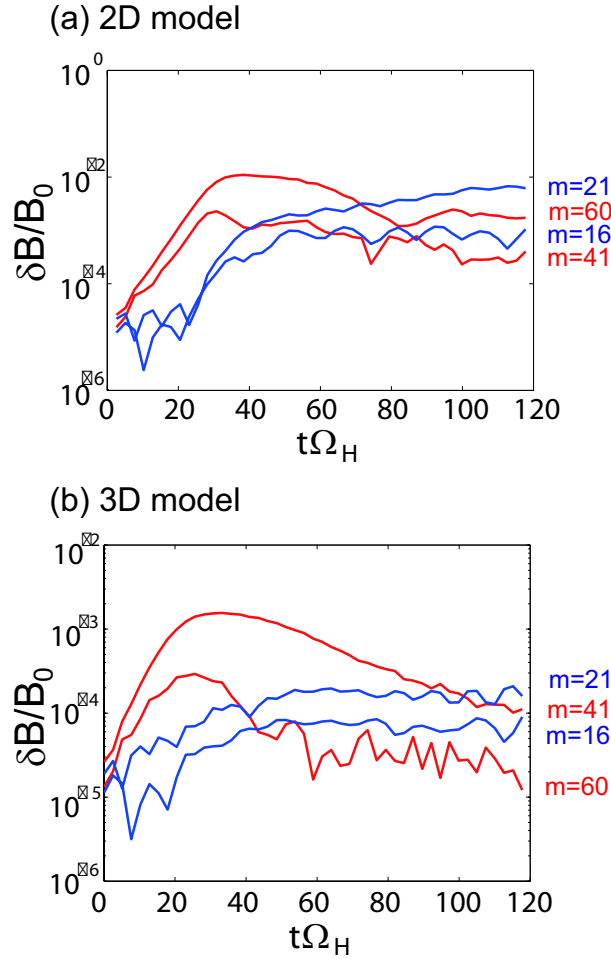
Figure 3.11: The amplitude of the L-mode EMIC wave for the various mode numbers ($m = 60$, 41 with red line and $m = 21$, 16 with blue line) in the (a) 2D and (b) 3D models.

the nonlinear evolution is dominated by the inverse cascading of the L-mode EMIC waves. This is another reason why the mirror instability is dominant in the magnetosheath.

## 3.5 Heating of Ions

Figure 3.13a shows the difference of the relaxation of the temperature anisotropy in the three different simulation models. Since there is no mirror mode wave in the 1D model, the L-mode EMIC instability consumes all of the free energy of the temperature anisotropy. In the 2D model, the L-mode EMIC waves are affected by the mirror instability, but the amplitude at the linear growth stage still becomes much larger than that of the mirror instability. In the linear stage, because of the dominance of the mirror instability, the temperature anisotropy in the 3D model decreases more quickly than that in the 1D and
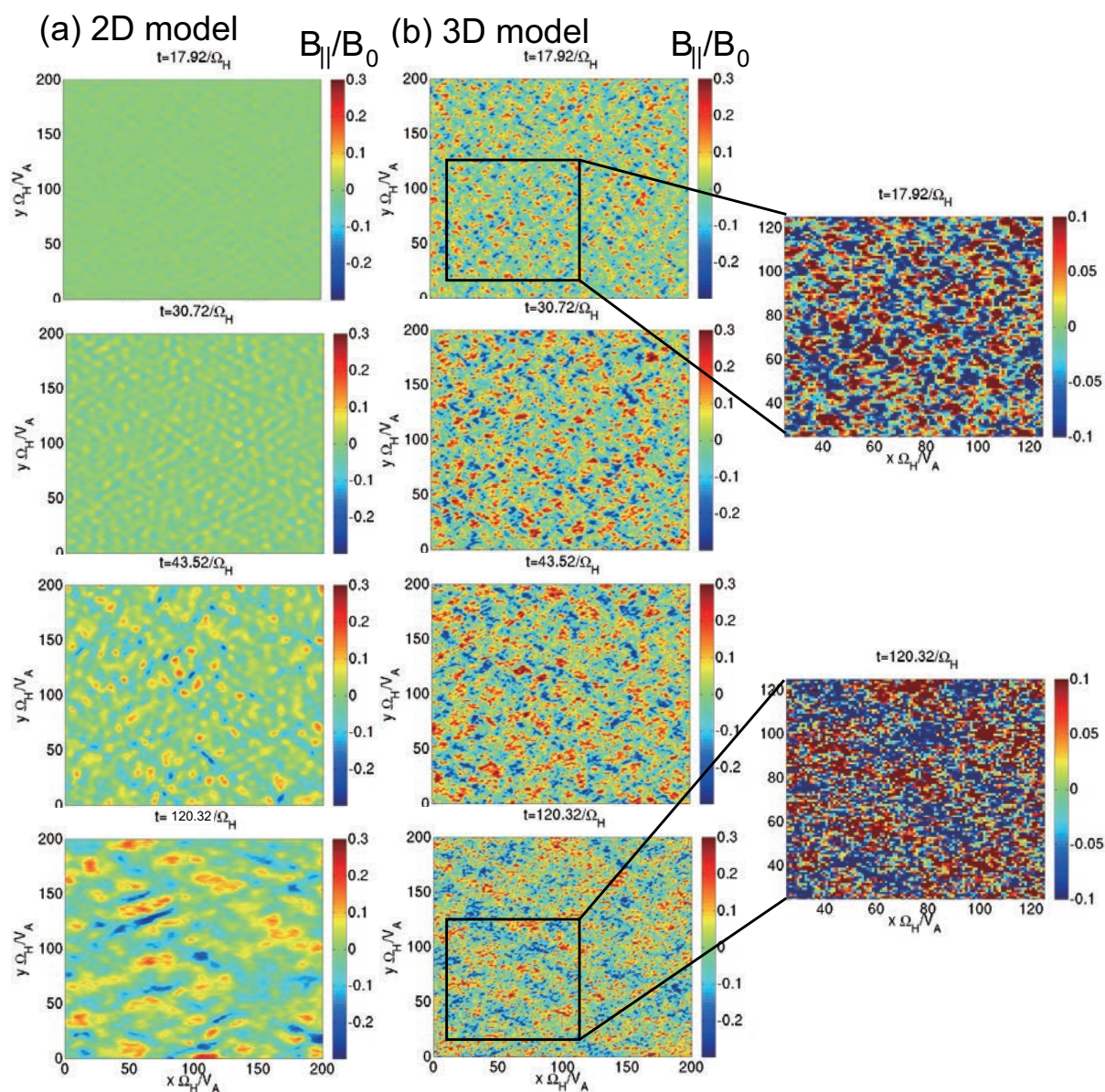
Figure 3.12: The time evolution of $\boldsymbol{B}_{\parallel}/B_0$ in the $x$-$y$ plane in the (a) 2D and (b) 3D models.
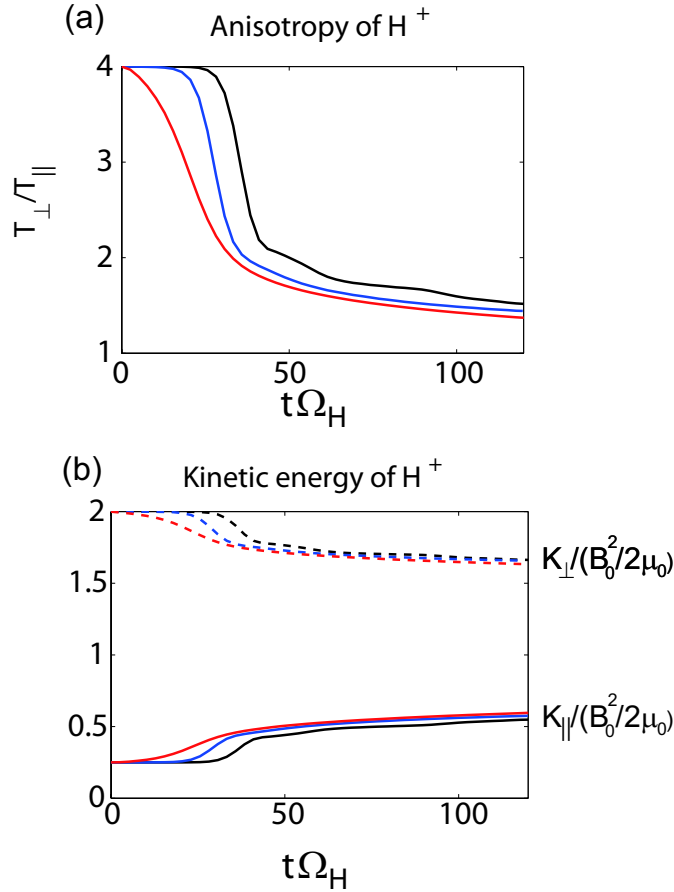
Figure 3.13: (a) The relaxation of the temperature anisotropy of protons. The black line shows the result in the 1D model, the blue line shows that in the 2D model, and the red line shows that in the 3D model. (b) The kinetic energy of H$^+$ in each direction. The solid line shows the kinetic energy in the parallel direction and the dashed line shows that in the perpendicular direction in each model.

2D models. The spreading of the energy spectrum of the mirror mode waves in the 3D model causes the effective consumption of the free energy of the temperature anisotropy.

After the energy density of each wave saturates, the anisotropy of protons is relaxed slower than that before saturation. Because of the heating by the nonlinear potential and the inverse cascading process, the L-mode EMIC waves lose their energy to thermalize the background protons, and therefore the system is dominated by the mirror mode waves in the nonlinear stage. In the later time, the temperature anisotropy in each model is almost the same. The nonlinear evolution of the L-mode EMIC instability is almost in the parallel direction in each model, the protons are heated by the nonlinear potential and the parallel propagating ion acoustic waves at the nonlinear stage. This heating is less dependent on the difference of the spatial dimension. Then the particle should be

heated to almost the same level among the three models. Figure 3.13b shows the kinetic energy density of protons in each model. We can find that the kinetic energies in the parallel and perpendicular directions are almost the same among the three models.

Figure 3.14 shows the time evolution of the energy in the 3D model up to $t = t_2 = 120.32/\Omega_{\mathrm{H}}$. Figure 3.14a shows the magnetic energy density of each wave. The solid black line shows $|\boldsymbol{B}/B_0|^2$ of the mirror mode waves, and the dashed black line shows $|\boldsymbol{B}/B_0|^2$ of the L-mode EMIC waves. In the nonlinear stage, the energy of the L-mode EMIC waves decreases and the kinetic energy of protons in the parallel direction increases. As the simulation space is the uniform model with the periodic boundary, the initially given total energy should be conserved. Then, the magnetic energy which decreases at the nonlinear stage should go into kinetic energy of protons.

Figure 3.14b shows the value of $\boldsymbol{J_i} \cdot \boldsymbol{E}/(B_0^2 \Omega_{\mathrm{H}}/\mu_0)$, where $\boldsymbol{J_i}$ is the ion current. Note that when $\boldsymbol{J_i} \cdot \boldsymbol{E} > 0$, the energy of electromagnetic waves goes to particles and vice versa. The time scale of the interaction between the ion acoustic waves and protons is much faster than that of the change of the mirror mode structure. The effect of the induced electric field due to the slow time variation of the magnetic field is much smaller than that of the ion acoustic waves. Thus the energy of the mirror mode waves does not go to protons. Figure 3.14c shows that the energy of the mirror mode waves goes to protons through $\boldsymbol{J_i} \cdot \boldsymbol{E}$.

For a further analysis, we separate $\boldsymbol{E}$ and $\boldsymbol{J}_i$ into the component of the L-mode EMIC waves and the mirror mode waves in the wavenumber space by the same method that we have used in section 3.3, respectively. We obtain the values of $\boldsymbol{J}_i \cdot \boldsymbol{E}$ of these waves and show the time evolution of them in Figure 3.15. The dash-dotted line shows the time when the $\boldsymbol{J}_i \cdot \boldsymbol{E}$ of the mirror mode waves becomes zero. At the linear stage, the value of $\boldsymbol{J}_i \cdot \boldsymbol{E}$ of the L-mode EMIC waves as shown in Figure 3.15a becomes naught faster than that of the mirror mode waves as shown in Figure 3.15b. Moreover, at the nonlinear stage, we can find that $\boldsymbol{J}_i \cdot \boldsymbol{E}$ of the L-mode EMIC waves turns to positive. The value of $\boldsymbol{J}_i \cdot \boldsymbol{E}$ of the mirror mode waves, on the other hand, is still almost zero. Therefore, this is also the evidence that the nonlinear evolution of the L-mode EMIC instability is a dominant factor for the heating of protons.

The implication of the conversation between kinetic and magnetic energy can be discussed by the sign of $\boldsymbol{J} \cdot \boldsymbol{E}$. From the Ampere's law shown in (2.2), we obtain

$$\boldsymbol{J} \cdot \boldsymbol{E} = (\boldsymbol{\nabla} \times \boldsymbol{B}) \cdot \boldsymbol{E}/\mu_0, \tag{3.21}$$

Using the vector identity

$$\boldsymbol{\nabla} \cdot (\boldsymbol{E} \times \boldsymbol{B}) = \boldsymbol{B} \cdot (\boldsymbol{\nabla} \times \boldsymbol{E}) - \boldsymbol{E} \cdot \boldsymbol{\nabla} \times \boldsymbol{B} \tag{3.22}$$
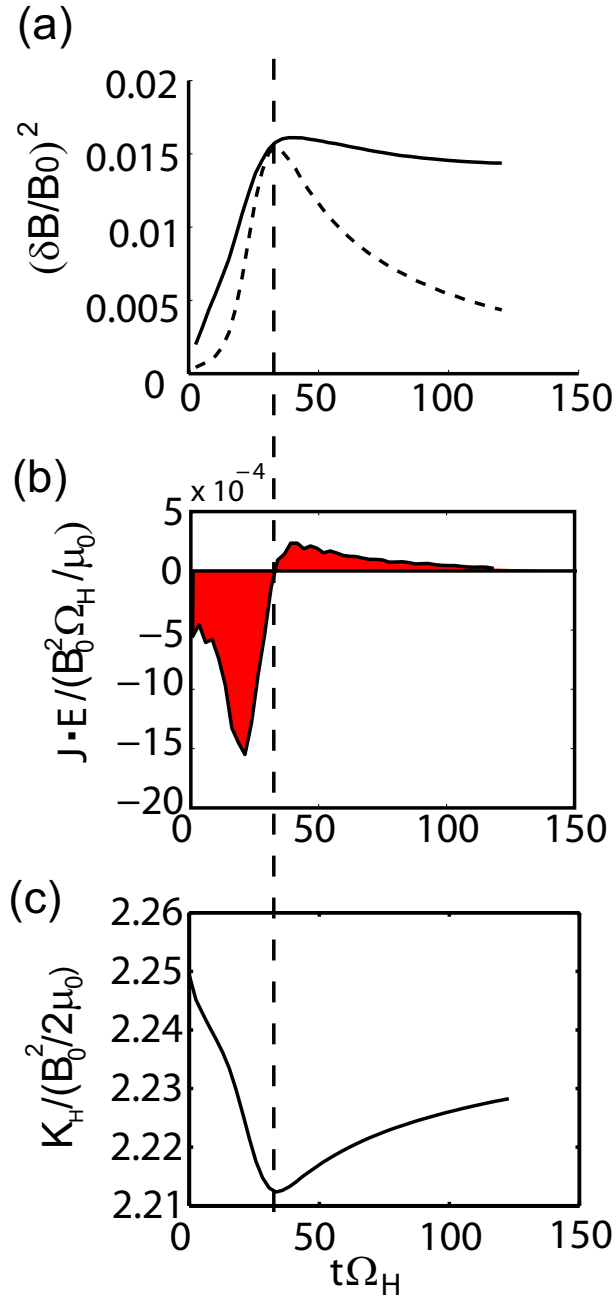
Figure 3.14: The time evolution of kinetic and magnetic energy in the 3D model. (a) The magnetic energy density of each mode. (b) The integrated value of $\boldsymbol{J} \cdot \boldsymbol{E}/(B_0^2 \Omega_{\mathrm{H}}/\mu_0)$ in the simulation space. (c) The kinetic energy density of protons $K_{\mathrm{H}}/(B_0^2/2\mu_0)$ in the 3D model.
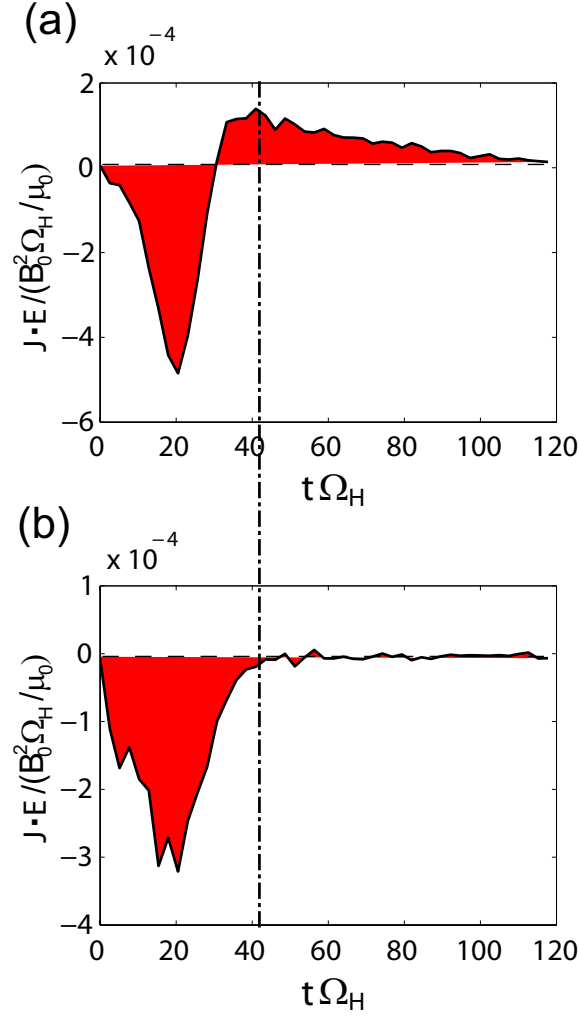
Figure 3.15: The value of $\boldsymbol{J}_i \cdot \boldsymbol{E}$ of each instability. (a) the L-mode EMIC instability, (b) the mirror instability.

and Faraday's law (shown in (2.1)) to (3.21), we obtain

$$\boldsymbol{J} \cdot \boldsymbol{E} = - \left( \boldsymbol{\nabla} \cdot (\boldsymbol{E} \times \boldsymbol{B}) + B \frac{\partial \boldsymbol{B}}{\partial t} \right) \Big/ \mu_0. \tag{3.23}$$

Therefore, the energy conservation of the electromagnetic field and the kinetic energy of ions are shown in (3.24).

$$\frac{\partial u_m}{\partial t} + \nabla \cdot \boldsymbol{S} = -\boldsymbol{J} \cdot \boldsymbol{E}, \tag{3.24}$$

where $u_m = B^2/2\mu_0$ is the energy density of the magnetic field and $\boldsymbol{S} = \boldsymbol{E} \times \boldsymbol{B}/\mu_0$ is the Poynting vector. From the Darwin's approximation for the hybrid simulation, the energy density of the electric field is negligible. Integrating the (3.24) in all of the simulation

space, we obtain

$$\int_V \left(\frac{\partial u_m}{\partial t} + \nabla \cdot \boldsymbol{S}\right) dv = -\int_V \boldsymbol{J} \cdot \boldsymbol{E} dv. \tag{3.25}$$

where, $V$ is the volume of the simulation space, $dv$ is the element of the volume. Since we assume the periodic boundary, there is no energy flow into or out from the simulation space. Then, the Poynting vector integrated in the surface of $V$ should be naught,

$$\int_V \nabla \cdot \boldsymbol{S} dv = \int_{\partial V} \boldsymbol{S} \cdot d\boldsymbol{a} = 0, \tag{3.26}$$

where $\partial V$ is the surface of the $V$ and $da$ is the element of area. Using $\bar{x}$ as the representation for the mean value of a physical value $x$ $\left(\bar{x} = \frac{1}{V}\int_V x dv\right)$, we obtain

$$\frac{\partial \overline{u_m}}{\partial t} = -\overline{\boldsymbol{J} \cdot \boldsymbol{E}}. \tag{3.27}$$

Taking the time derivative, we finally obtain (3.28)

$$\frac{\partial^2 \overline{u_m}}{\partial t^2} = -\frac{\partial \overline{\boldsymbol{J} \cdot \boldsymbol{E}}}{\partial t}, \tag{3.28}$$

In the hybrid simulation, if we assume the phase speed is much slower than the speed of light $c$, then the electric energy density $u_e = E^2/2c^2$ term can be neglected. Because the net system energy is conserved such as $u_m + K_H = const.$, the second derivative of the kinetic energy $\partial^2 K_H/\partial t^2$ is equal to $-\partial^2 u_m/\partial t^2$. In the growing phase, when the sign of $\partial^2 u_m/\partial t^2$ is positive, the electromagnetic waves grow exponentially, and when it is negative, they suffer from the nonlinear effect. Then, (3.28) indicates we can judge whether linear or nonlinear growth is dominant in the growing phase with the sign of the derivative of $\boldsymbol{J_i} \cdot \boldsymbol{E}/(B_0^2\Omega_H/\mu_0)$. At the minimal point of $\boldsymbol{J_i} \cdot \boldsymbol{E}/(B_0^2\Omega_H/\mu_0)$, there is the point of change from linear growth to nonlinear growth. From Figure 3.14b, showing $\boldsymbol{J_i} \cdot \boldsymbol{E}/(B_0^2\Omega_H/\mu_0)$, we find the time at the minimal point is $t = 23.04/\Omega_H$, and this time agrees with the time when the ion acoustic waves are generated (from the bottom panel of Figure 3.9c).

## 3.6 Summary and Discussion

In this chapter, we discuss the competing processes between the L-mode EMIC and mirror instabilities in the Earth's magnetosheath, which have been a long standing puzzle, via computer simulations. By expanding the simulation system from a 2D model to a 3D model, we find that the mirror instability dominates over the L-mode EMIC instability because the mirror mode waves form torus-like structures in the 3D wavenumber space as shown in Figure 3.5a. We also derived the theoretical condition of the initial thermal

fluctuations for the diminance of the mirror instability. The realistic conditions result in the dominance of the mirror mode wave.

The saturation level of the L-mode EMIC waves in the 3D model becomes smaller than those in the 1D and 2D models because the mirror instability effectively consumes the free energy of the temperature anisotropy. In Figure 5.8, we found the nonlinear heating of the whole proton distribution functions. We cannot find the quasi-linear effect which occurs near the resonance velocity of the fastest growing mode of EMIC waves ($\simeq 0.4V_\mathrm{A}$). We therefore conclude that saturation of the L-mode EMIC waves is caused by the heating by the nonlinear potentials and the nonlinear wave-wave coupling. The existence of the helium also plays an important role on the competing process.

In the nonlinear stage, the kinetic energy is almost the same among the 1D, 2D, and 3D models as shown in Figure 3.13a. From figure 3.6, we find the nonlinear evolution is dominated by the L-mode EMIC instability. In all models, the L-mode EMIC waves transfer of their energy to ions through the heating by the nonlinear potentials and the generated ion acoustic waves. With these nonlinear processes, the L-mode EMIC waves lose their energy quickly. These phenomena take place with the parallel propagating waves, and thus the nonlinear heating occurs almost in the parallel direction. Because of these nonlinear heatings of protons in the parallel direction, the temperature anisotropy decreases to the threshold of the mirror instability, and thus the growth of the mirror mode waves saturates.

Coalescence of the mirror mode structures proceeds after the saturation of the mirror instability in both 2D and 3D models. The topology of the mirror mode structures in the 3D model differs from that in the 2D model because of the difference in degree of freedom in the perpendicular direction. This causes a clear difference in nonlinear evolution of the magnetic field structures. At the end of the nonlinear evolution, these structures still remain. This coalescence occurs on a longer time scale than for inverse cascading of the L-mode EMIC waves. In the magnetosheath, this nonlinear effect on the dominance of mirror instability should occur not near the bowshock but in regions of the deep magnetosheath or magnetopause, where the L-mode EMIC waves have reached nonlinear levels and are decaying. Therefore, it becomes likelier to observe mirror mode waves in inside the magnetosheath rather than near the bowshock.

We note that *Tsurutani et al.* [1982] has measured the scale size at Earth and found it to be much larger than the ion inertial length. As the ion beta and temperature anisotropy becomes lower, the wavelength of the most unstable mode becomes larger [*Hasegawa et al.*, 1969]. This mode, however, cannot grow enough because the maximum growth rate is small, and the temperature anisotropy is mostly consumed by the L-mode EMIC wave.

We found that the scale size becomes larger and comparable to the observed one through the coalescence process as shown in Figure 3.12. The wave amplitude is still large after this nonlinear process takes place, and the observed mirror mode waves also have large amplitude. Therefore, the large mirror mode structure in the magnetosheath should be caused by not only the linear growth but also the nonlinear process. For more precise comparison with the observations, more parametric analyses are needed, and moreover the nonlinear evolution must be followed in an open system with anisotropic ion population injected from the upstream of the magnetosheath. Such simulations are left as a future study.

To our knowledge, this is the first study to analyze the competing process between the L-mode EMIC instability and the mirror instability by the 3D hybrid simulation. Mirror instability becomes dominant by three reasons: the large volume of the mirror mode waves in the 3D wavenumber space, the existence of the alpha particles, and the quick dissipation of the L-mode EMIC waves due to nonlinear evolution. More analysis for the slower nonlinear process is discussed in next chapter.

# Chapter 4

# Nonlinear Evolution of Mirror Instability in Open Boundary Models

## 4.1 Introduction

In Chapter 3, we discussed the competing processes between the L-mode EMIC and the mirror instabilities in the Earth's magnetosphere. We discuss the different nonlinear evolutions of the mirror and the L-mode EMIC instabilities. In this chapter, we focus on the nonlinear evolution of the mirror mode structures which we introduced as the coalescence of the magnetic structures.

As we discussed in Section 1.2, the mirror instability is a well known electromagnetic phenomenon which is excited by the temperature anisotropy ($T_\perp/T_\parallel$ >1) of hot ions in the perpendicular direction to the ambient magnetic field [*Chandrasekhar et al.*, 1958; *Hasegawa*, 1969, 1975]. The associated mirror mode structures are often observed in the magnetosheath of the Earth [e.g. *Tsurutani et al.,* 1982, 1984; *Hubert* 1994; *Phan et al.,* 1994; *Lacombe and Belmont*, 1995], the planets [e.g. *Tsurutani et al.,* 1993; *Violante et al.*, 1995], the comets [*Tsurutani et al.,* 1999; *Russell et al.,* 1989; *Glassmeier et al.*, 2003] and the heliosheath [*Tsurutani et al.,* 2011]. They are formed when the anisotropic hot ions satisfy the condition: $\beta_\perp/\beta_\parallel > 1 + 1/\beta_\perp$ [e.g. *Hasegawa*, 1969; *Price et al.*, 1986; *Lee et al.,* 1988; *Southwood and Kivelson*, 1993; *Kivelson and Southwood* 1996], where $\beta_\perp$ and $\beta_\parallel$ are the ion beta values perpendicular and parallel to the background magnetic field. The mirror instability has the largest linear growth rate with the wavenumbers oblique to the static magnetic field and the frequency $\omega = 0$. Thus the mirror mode structures do not move from the region where they arise.

The temperature anisotropy also drives the L-mode EMIC instability [*Kennel and Petschek*, 1966], which has a larger linear growth rate than that of mirror instability

[*Gary*, 1992; *Lacombe and Belmont*, 1995]. Comparing the L-mode EMIC and mirror instabilities in the multi-dimensional periodic boundary systems, we have shown that the mirror instability dominates over the L-mode EMIC instability in the Earth's magnetosheath [*Shoji et al.*, 2009]. We have found that one of the important points for the dominance of the mirror instability is the 3D spatial distributions of wavenumber spectra. The mirror mode structures have wavenumber vectors mostly in the oblique directions and thus their wavenumber spectra become like a "torus". The difference of nonlinear evolutions of the L-mode EMIC waves and mirror mode structures are also important because the L-mode EMIC waves cause the nonlinear wave-particle interactions, heat ions, and lose energy. As a result of the competition, only the mirror mode structures remain in the space.

Satellite observations [*Soucek et al.*, 2008; *Balikhin et al.*, 2009, 2010] indicate that the mirror mode structures are observed as large amplitude quasi-periodic structures called magnetic peaks (also called humps) and magnetic dips (also called holes) in the terrestrial magnetosheath. *Soucek et al.* [2008] reported observations of magnetic peaks near the bowshock and of the magnetic dips near the magnetopause. Figure 4.1 shows the examples of the observation results of the different magnetic structures. The top panel shows the magnetic peak structures which is observed far from the magnetopause (distance from the magnetopause is 13615.0 km). The bottom panel, which is the observation near the magnetopause (distance is 668.4 km), shows the magnetic dips. They also showed the dependence of magnetic structures on the temperature anisotropy and beta of ions. A one-dimensional hybrid simulation [*Califano et al.*, 2008] and quasi-linear theoretical analyses [*Hellinger el al.*, 2009] were performed. They show contributions of the nonlinear term of the mirror mode structures to the magnetic peaks and dips.

The torus-like wavenumber spectra in the 3D space also make magnetic structures different from those in the 2D space. The purpose of the study in this chapter is to understand how the spatial dimensionality affects the nonlinear mirror mode structures. We also perform parametric analyses on the ion beta to explain the observational results [*Soucek et al.*, 2008]. In this chapter, we discuss the nonlinear evolution of the mirror mode structures. The multi-dimensional open boundary hybrid simulation is used. In Section 4.2, the difference of the magnetic structures in the 2D and 3D models are shown. The analyses on the skewness, which are used in the previous studies [*Soucek et al.*, 2008; *Califano et al.*, 2008] are performed to identify the magnetic structures. In Section 4.3, the simulations in the higher spatial resolution are performed in the 2D and 3D models. The initial conditions for the generation of the magnetic peaks and dips are shown. The process of the coalescence of the mirror mode structures are also discussed. In Section
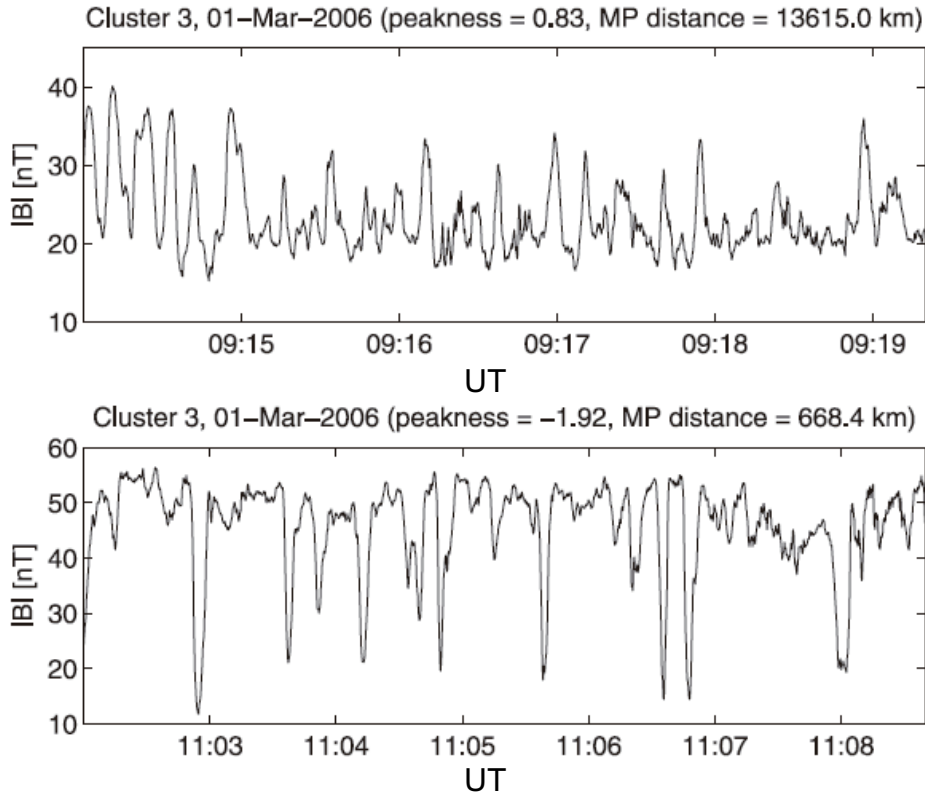
Figure 4.1: Cluster 3 observations of the mirror mode structures. [*after Soucek et al., 2008*]

4.4, we briefly conclude this chapter and compare the results with the observation results.

## 4.2 Nonlinear Structures in Multi-Dimensional Open Boundary Models

A schematic illustrations of the hybrid simulation models for the mirror instability are shown in Figure 4.2. As shown in Figure 4.2a, in a system with the periodic boundaries, the L-mode EMIC waves propagating along the parallel direction stay in the simulation space. We cannot neglect the effect of the L-mode EMIC instability such as formation of the nonlinear potentials by the forward and backward propagating EMIC waves [*Omura et al.*, 1988]. Especially, in the 2D model, the L-mode EMIC instability dominates over the mirror instability [*Shoji et al.*, 2009]. To obtain clear magnetic structures excited by the mirror instability, we perform the hybrid simulations with open boundaries which are introduced in Section 2.4. As shown in Figure 4.2b, in the open boundary models, the L-mode EMIC waves go out from the simulation space. On the other hand, the

frequency of the mirror mode structures is zero, and thus they do not propagate away from the place where they arise. Therefore, only the mirror mode structures remain in the open boundary model. We performed both 2D and 3D hybrid simulations with the open boundaries and compared the mirror mode structures in these models. The grid spacing $\Delta x$ is $1.0 V_A/\Omega_H$. The numbers of grid points are $(n_x, n_y, n_z) = (512, 512, 1)$ and $(512, 512, 512)$ for the 2D and 3D models, respectively. The time step is $\Delta t = 0.04/\Omega_H$. The number of superparticles are $N_p = 2^{31}$ in both models.

We discuss the contribution of the mirror instability to the magnetic peaks or dips in the 2D and 3D models. We use the skewness (or called peakness in *Soucek et al.*, [2008]) to identify the magnetic structures as magnetic peaks or dips, which is introduced in *Califano et al.*, [2008]. The skewness is a statistical value to measure an asymmetry of a distribution of samples. When the skewness is positive, the right tail of the distribution is longer than the left tail. In this case, the mass of the sample is concentrated on the left side. When the skewness is negative, the left tail is longer, the mass of the sample is concentrated on the right side. Applying this statistical analysis to the mirror mode structure, we can find out whether the magnetic field slant on the left or right tails of the distribution. The positive skewness indicates magnetic peaks, while the negative one indicates magnetic dips. The skewness $s$ for a set of sample values $\{x_k\}$ is defined as the normalized third momentum: $s = \mu_3/\sigma^3$, where $\mu_n$ is the $n$th momentum of the sample defined by

$$\mu_n = \frac{1}{N} \sum_{k=1}^{N} (x_k - m)^n, \tag{4.1}$$

where $m$ is the mean of $\{x_k\}$, and $\sigma = \sqrt{\mu_2}$ (standard deviation).

The 2D open boundary results with the temperature anisotropy $T_\perp/T_\parallel = 4$ and the ion beta $\beta_\parallel = 0.5$ are shown in Figure 4.3. The time evolution of the skewness of $B_x$ is shown in Figure 4.3a. The skewness turns from positive to negative. As the time increases, the absolute number of the skewness becomes larger. It indicates that the magnetic dips sustain and grow solitary in the 2D model. We find large and clear magnetic dips in Figure 4.3b, which shows the magnetic field amplitude at $t = 120/\Omega_H$ (shown by the dashed line in Figure 4.3). The depth of the magnetic dips is $\sim 0.5 B_0$. The waveforms in the $x$ and $y$ directions are shown in Figures 4.3d and 4.3c, respectively. The scale of the magnetic dip in the $x$ direction is larger than that in the $y$ direction. At this time, because of the open boundary effect, the L-mode EMIC waves have already disappeared from the simulation space and we obtain clear magnetic structures. The variations of the perpendicular components $B_y$ and $B_z$ are much smaller than that of the parallel component $B_x$. That means the magnetic dips formed by the mirror instability
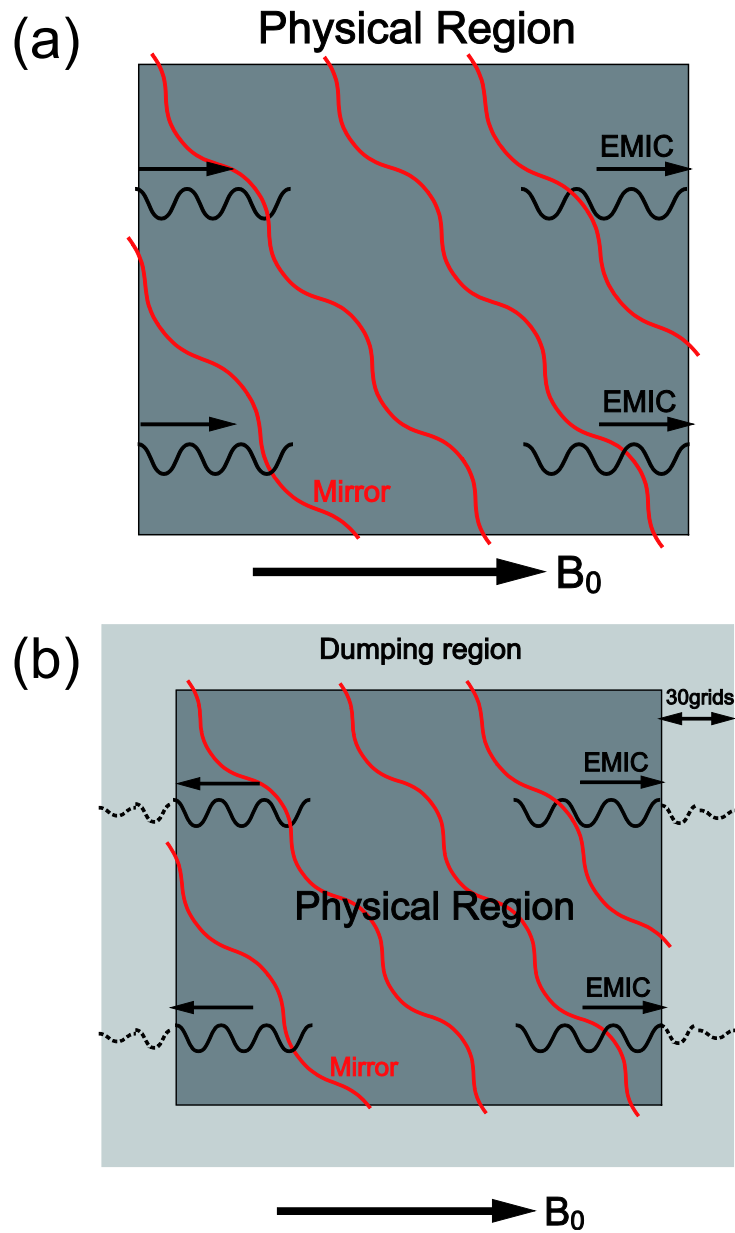
Figure 4.2: Schematic illustrations of EMIC waves and mirror-mode structures in (a) periodic boundary model and (b) open boundary model.

are mostly the parallel component. Because of the condition from the Maxwell's equation, $\nabla \cdot \boldsymbol{B} = 0$, the components of the magnetic field in the $y$ and $z$ directions become smaller. The angular change in the magnetic dip in the 2D model is $\sim 8°$. *Tsurutani et al.* [2011] indicates that the magnetic decreases have larger angular change and the magnetic decreases which have the angular change $< 10°$ are called the linear magnetic decreases [*Winterhalter et al.,* 1994]. Thus, the magnetic dips formed by the mirror instability can correspond to the linear magnetic decreases as mentioned in the previous studies [*Winterhalter et al.,* 1994; *Zhang et al.,* 2009].

The 3D open boundary results with the same temperature anisotropy and ion beta as the 2D simulation are shown in Figure 4.4. The skewness of $B_x$ is always positive as shown in Figure 4.4a. The skewness has the maximum value at $t = 22/\Omega_H$ which is around the time when the mirror instability stops growing [*Shoji et al.,* 2009]. The skewness become smaller after $t = 22/\Omega_H$, resulting in depression of the magnetic peaks. Figures 4.4b and 4.4c show cross sections of the magnetic field in $xy$ and $xz$ planes, respectively. Variations of the $x$, $y$, and $z$ components of the magnetic field vector are plotted as functions of $x$, $y$, and $z$ over the ranges including the magnetic peak structure in Figures 4.4d, 4.4e, and 4.4f, respectively. The magnetic peaks are also found only in the $x$ component (in black) of the magnetic field.

## 4.3   Higher Resolution Simulation for the Mirror Mode Structures

To analyze the magnetic structures more precisely, we performed 2D and 3D simulations in small simulation spaces with higher spatial resolution. The numbers of grids ($n_x$, $n_y$, $n_z$) are (128, 128, 1) and (128, 128, 128) for the 2D and 3D models, respectively. The grid spacing $\Delta x = 0.5\Omega_H/V_A$ and the time step $\Delta t = 0.02/\Omega_H$ are used. The numbers of particle in each grid is assumed as $N_p$/cell=2048 and $N_p$/cell=128 for the 2D and 3D models, respectively.

### 4.3.1   Magnetic structures in the 2D models

Magnetic field structures $((B_0 + \delta B)/B_0)$ generated by a temperature anisotropy $T_\perp/T_\parallel = 2$ with different parallel betas $\beta_\parallel$ =1, 4, and 10 in the 2D model are shown in Figures 4.5a, 4.5b, and 4.5c, respectively. We can find the magnetic dips in Figure 4.5a at $t = 1308.6/\Omega_H$. The scale size in the parallel direction ($\sim 20$ ion inertia length) is larger than that in the perpendicular direction ($\sim 10$ ion inertia length). This result agrees with that in Figure 4.3. On the other hand, in Figures 4.5b and 4.5c, which show the magnetic
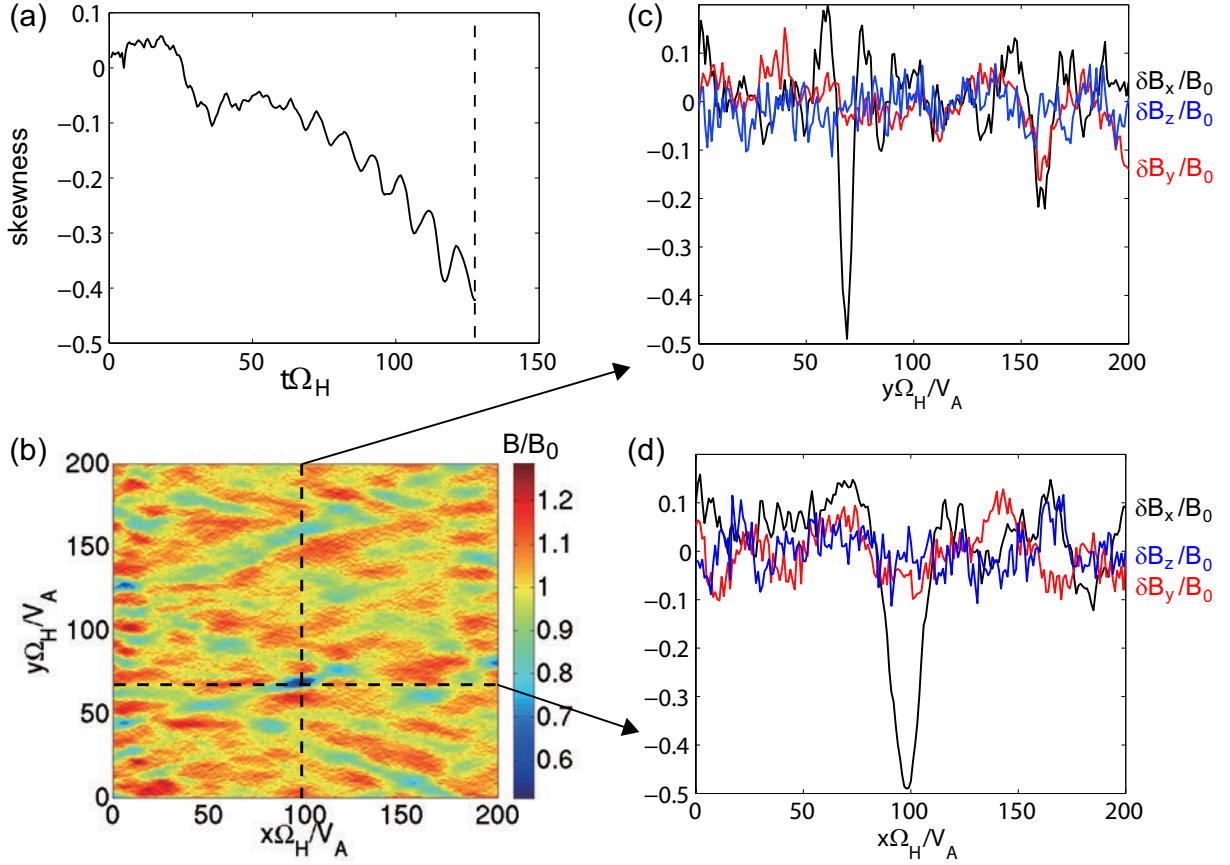
Figure 4.3: The skewness of $\delta B_x$ and the typical magnetic structures in the 2D open boundary models with $T_\perp/T_\parallel = 4$ and $\beta_\parallel = 0.5$. (a) The skewness of $\delta B_x$ calculated with whole grid points. (b) Contour of $|\boldsymbol{B}_0 + \delta \boldsymbol{B}|/B_0$ at $t = 120\Omega_H$ which is indicated by a dashed line in panel (a). (c), (d) Waveforms of the magnetic field components along $y = 70\Omega_H/V_A$ and $x = 100\Omega_H/V_A$, which are shown by dashed lines in panel (b), respectively. In each panel, the black, red, and blue lines show $\delta B_x/B_0$, $\delta B_y/B_0$, and $\delta B_z/B_0$, respectively.
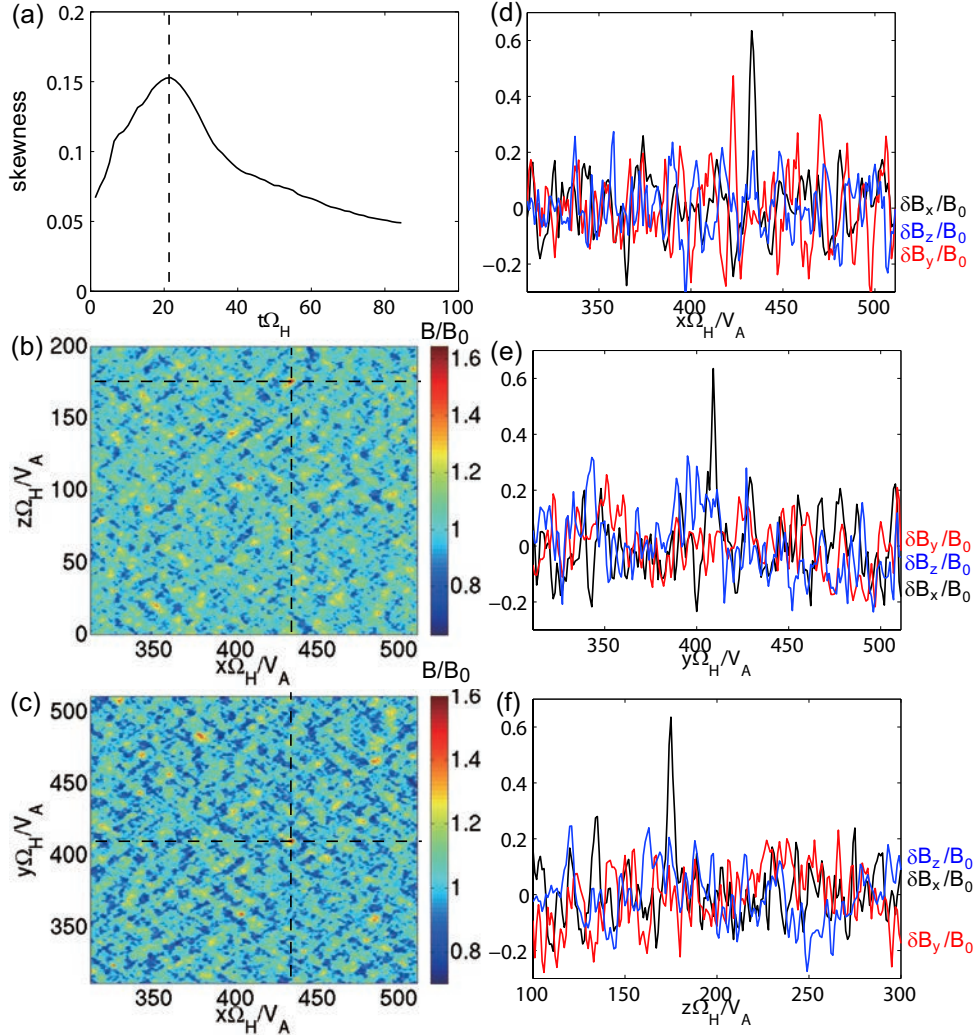
Figure 4.4: The skewness of $\delta B_x$ and the typical magnetic structures in the 3D open boundary model with $T_\perp/T_\parallel = 4$ and $\beta_\parallel = 0.5$. (a) The skewness of $\delta B_x$ calculated with whole grid points. (b),(c) Cross sections of $B/B_0 = |\boldsymbol{B}_0 + \delta\boldsymbol{B}|/B_0$ at $t = 40\Omega_H$ which is indicated by a dashed line in panel (a)in $xy$ and $xz$ plane. (d), (e), (f) Waveforms of the magnetic field components along $y = 20\Omega_H/V_A$ and $x = 200\Omega_H/V_A$, respectively, which are shown by dashed lines in panels (b) and (c). In each panel, the black, red, and blue lines show $\delta B_x/B_0$, $\delta B_y/B_0$, $\delta B_z/B_0$, respectively.

field at $t = 600/\Omega_H$, we find that the magnetic peaks exist dominantly. This trend, that the magnetic peaks appear instead of the magnetic dips as the ion beta becomes larger, shows a good agreement with the observation results [*Soucek et al.*, 2008].

The time history of the generation processes of the magnetic dips with $\beta_\parallel = 1$ is shown in Figures 4.6a, 4.6b, 4.6c, and 4.6d. We also show the ion pressure in the perpendicular direction in Figures 4.6e, 4.6f, 4.6g, and 4.6h, where $p_0 = B_0^2/2$. Because of the pressure balance condition of the mirror instability [*Kivelson and Southwood*, 1991], the ion pressure becomes larger where the magnetic field is weak and vice versa. Because the initial condition of the plasma ($\beta_\parallel = 1$ and $T_\perp/T_\parallel = 2$) is near the threshold of the mirror instability [e.g. *Hasegawa*, 1969]

$$T_\perp/T_\parallel \simeq 1 + 1/\beta_\perp, \tag{4.2}$$

the mirror instability driven by the temperature anisotropy generates the sinusoidal magnetic structures. The mirror mode structures have wavevectors almost in the perpendicular angles as shown in Figure 4.6a due to the linear growth rate. Some particles are trapped inside the region where the magnetic field is weak (magnetic dip), and the ion pressure becomes larger in it as shown in Figure 4.6e. In Figures 4.6b and 4.6c, we find coalescence of some of the magnetic dips, and diffusion of the magnetic peaks. Figures 4.6f and 4.6g also indicate the coalescence. In Figures 4.6d and 4.6h, we can find that some particles are trapped inside the magnetic dips and thus the pressure becomes larger.

The velocity distribution function of the protons in these localized regions are also shown in Figure 4.7. The top panels show the initial distributions. A top-flatted velocity distribution function is found in the lower panel of Figure 4.7b. This is due to the mirror motion of the protons trapped by the magnetic dips. The magnetic structures become like a magnetic mirror device. When a pitch angle $\alpha$ of a proton satisfies

$$\sin^{-1}\sqrt{(B_{\rm dip}/B_{\rm out})} < \alpha < \pi - \sin^{-1}\sqrt{(B_{\rm dip}/B_{\rm out})}, \tag{4.3}$$

where $B_{\rm out}$ and $B_{\rm dip}$ are amplitudes outside and inside of the magnetic dip, respectively, the proton is trapped in the magnetic mirror structure. We plot the angle $\sin^{-1}\sqrt{(B_{\rm dip}/B_{\rm out})}$ and $\pi - \sin^{-1}\sqrt{(B_{\rm dip}/B_{\rm out})}$ in Figure 4.7b and find the top-flat velocity structures inside the region satisfying (4.3). The pitch angle of these particles are well scattered through this motion and thus the distribution becomes top-flat. Therefore the pressure inside the magnetic dips become larger. The proton distribution functions outside the dip shown in the lower panel of the Figure 4.7a, on the other hand, does not have such a top-flat structure. Because the mirror instability starts from the low beta condition near the threshold of the instability, the particles are less heated.
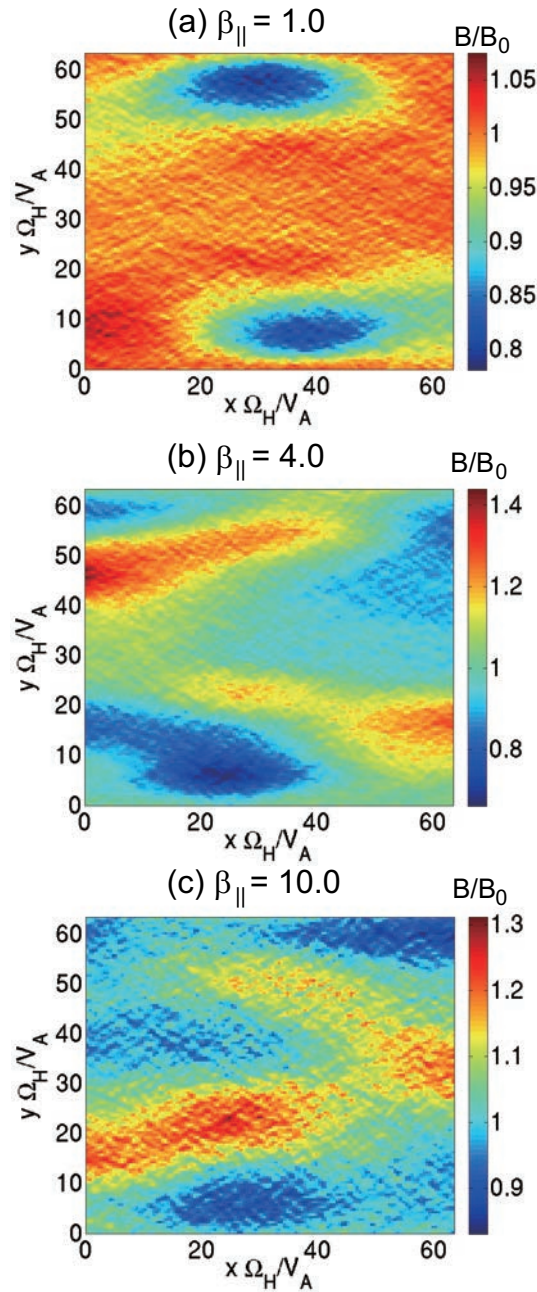
Figure 4.5:  Mirror mode structures in the 2D model with the initial ion parameters $T_\perp/T_\parallel = 2$ and (a)$\beta_\parallel = 1$ at $t = 1308.6/\Omega_H$ (b)$\beta_\parallel = 4$ at $t = 652.8/\Omega_H$ (c)$\beta_\parallel = 10$ at $t = 652.8/\Omega_H$.
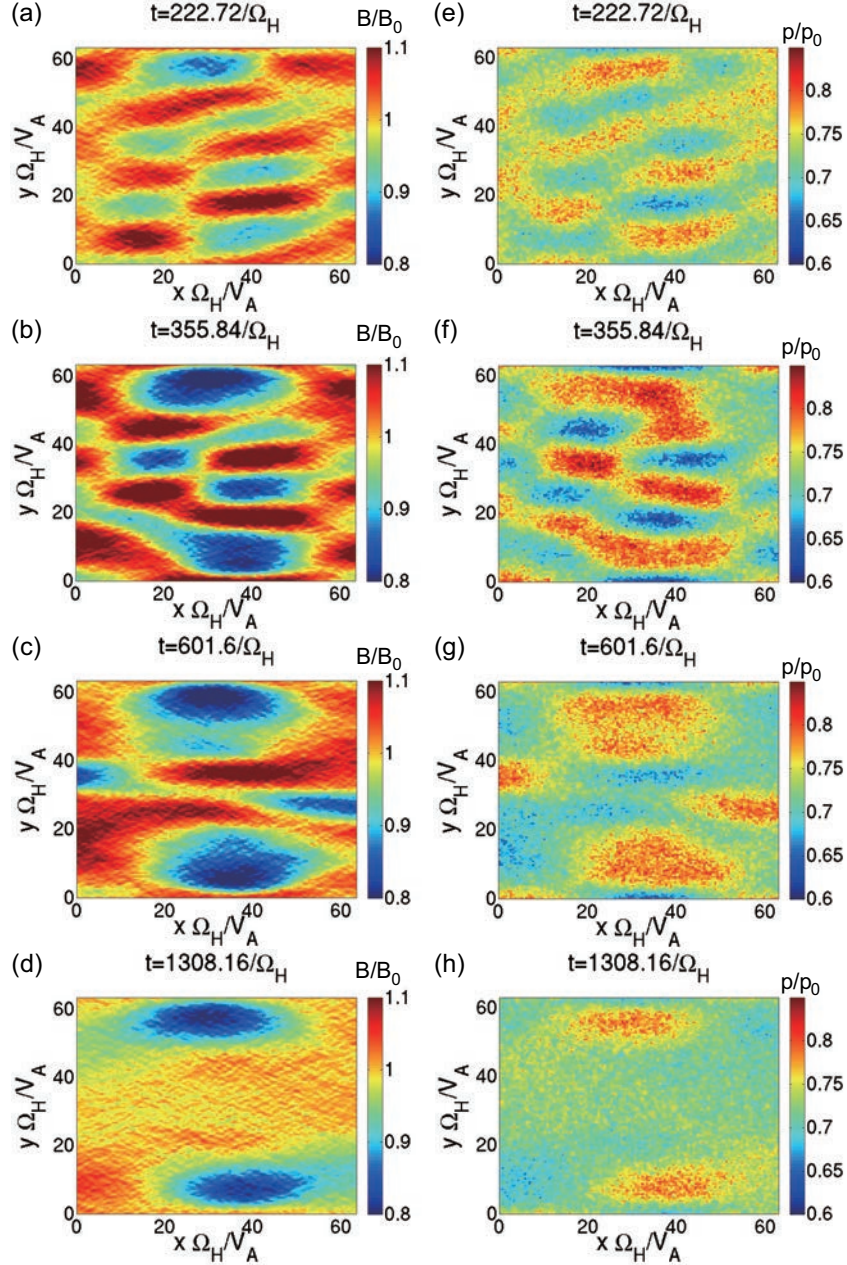
Figure 4.6: Spatial profiles of the magnetic field $B/B_0 = |\boldsymbol{B}_0 + \delta\boldsymbol{B}|/B_0$ at (a) $t = 222.72/\Omega_H$, (b) $t = 355.84/\Omega_H$, (c) $t = 601.6/\Omega_H$, and (d) $t = 1308.16/\Omega_H$ in the 2D model with $\beta_\| = 1$. The time evolution of the ion pressure at (e) $t = 222.72/\Omega_H$, (f) $t = 355.84/\Omega_H$, (g) $t = 601.6/\Omega_H$, and (h) $t = 1308.16/\Omega_H$, where $p_0 = B_0^2/2$.
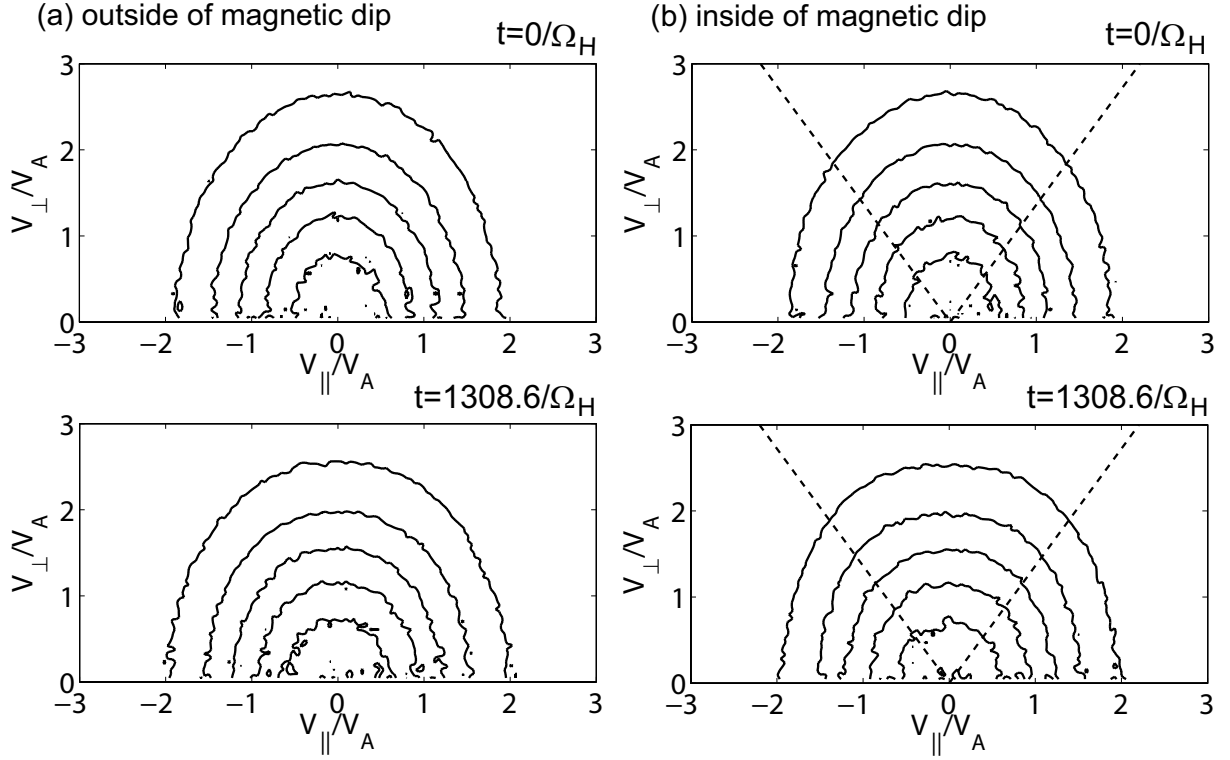
Figure 4.7: Velocity distribution functions of protons in the 2D local regions (a) inside the dip and (b) outside the dip. The black dashed lines in panels (b) show the pitch angle $\sin^{-1}\sqrt{(B_{\mathrm{dip}}/B_{\mathrm{out}})}$, and $\pi - \sin^{-1}\sqrt{(B_{\mathrm{dip}}/B_{\mathrm{out}})}$.

The time evolutions of magnetic structures and ion pressures in the perpendicular direction in the case of $\beta_{\parallel} = 10$ are shown in Figures 4.8a and 4.8b, respectively. The initial condition of the protons ($\beta_{\parallel} = 10$ and $T_{\perp}/T_{\parallel} = 2$) is far from the threshold of the mirror instability

$$T_{\perp}/T_{\parallel} \gg 1 + 1/\beta_{\perp}, \tag{4.4}$$

and thus the mirror mode structures are initially driven with wavevectors in oblique angles as we can see in the top panel of Figure 4.8a. Through Figures 4.8a to 4.8d and Figures 4.8e to 4.8h, we find coalescences of magnetic structures [*Shoji et al.,* 2009] and the associated pressure of ions, respectively.

In Figure 4.9, we show the distribution functions in the case with $\beta_{\parallel} = 10$. There is little difference between the distribution functions inside and outside the magnetic peaks. The upper panel of Figure 4.9 show the initial distribution functions. After the magnetic peak is generated, shown in the lower panel of Figure 4.9, the distribution function becomes larger in the parallel direction. In the growing phase of the mirror instability, the mirror mode structures have the electric field in the parallel direction
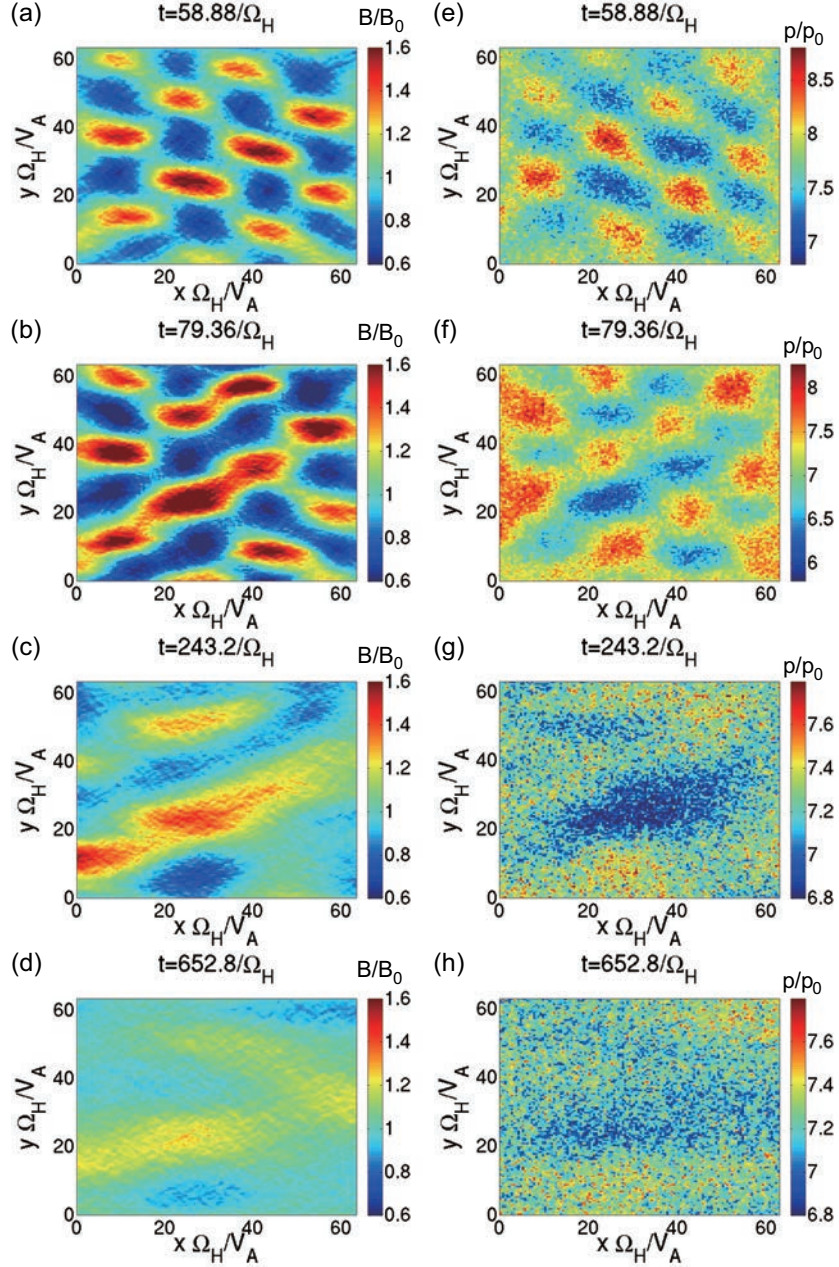
Figure 4.8: Spatial profiles of the magnetic field $|\boldsymbol{B}_0 + \boldsymbol{B}|$ at (a) $t = 58.88/\Omega_H$, (b) $t = 79.36/\Omega_H$, (c) $t = 245.2/\Omega_H$, and (d) $t = 652.8/\Omega_H$ in the 2D model. The time evolution of the ion pressure at (e) $t = 58.88/\Omega_H$, (f) $t = 79.36/\Omega_H$, (g) $t = 245.2/\Omega_H$, and (h) $t = 652.8/\Omega_H$ in the 2D model, where $p_0 = B_0^2/2$.

because they are caused by the oblique wavenumbers. The wave amplitude becomes larger in Figure 4.8a than that in Figure 4.6a. The electric fields of the mirror instability are generated strongly, and thus the perpendicular energy of the protons is transfered into the parallel direction both inside and outside the magnetic peaks as shown in the lower panel of Figure 4.9.
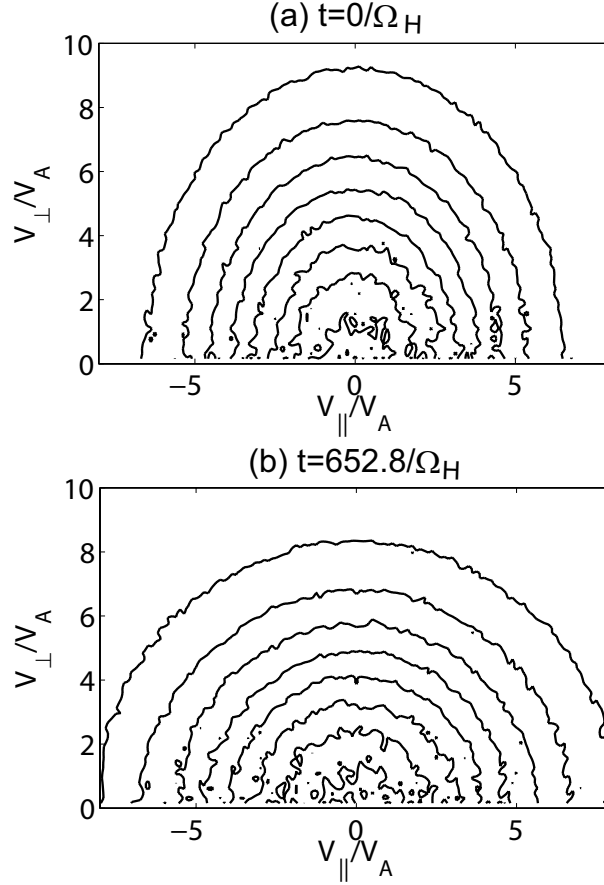


Figure 4.9: Velocity distribution functions of protons in the 2D model in the case with the ion beta $\beta_\parallel = 10$ at (a) $t = 0/\Omega_H$ and (b) $t = 652.8/\Omega_H$.

These results indicate that the magnetic peaks in the 2D models are formed through the following processes. The temperature anisotropy of the protons excites the mirror instability far above the threshold. The generated mirror mode structures form sinusoidal mesh structures as shown in Figure 4.8a. At the same time, the protons have larger parallel velocity due to the growing mirror mode structures. The protons, which initially assumed as high beta, gain higher mobility. The magnetic field lines at this time are shown in Figure 4.10a. In the magnetic dips, there appear "ion bubbles", which consist of the trapped ions inside the magnetic dips as shown in Figure 4.8e. The schematic plots of diamagnetic currents (red lines) inside the magnetic dips are also shown. The neighboring

current loops attract with each other and thus, these currents merge. As a result, the coalescence of the ion bubbles in the magnetic dips takes place. The coalesced magnetic dips form "magnetic troughs" as shown in Figure 4.8b. The magnetic field lines are shown in Figure 4.10b. The magnetic troughs are supported by the merged current lines. As the coalescence proceeds further, the trough become larger. The regions with larger magnetic fields become narrower, appearing as the magnetic peaks as shown in Figures 4.8c and 4.10c. The high mobility of the particles helps the continuous coalescence. These particles also move across the magnetic peaks, and thus the magnetic peaks diffuse as shown in Figure 4.8d.

## 4.3.2 Magnetic structures in the 3D models

Figures 4.11a, 4.11b, and 4.11c show cross sections of $B = |\boldsymbol{B_0} + \delta\boldsymbol{B}|$ in the 3D model with the temperature anisotropy $T_\perp/T_\parallel = 2$ and the ion beta $\beta_\parallel = 1$ (at $t = 164/\Omega_H$), $\beta_\parallel = 4$ (at $t = 164/\Omega_H$) and $\beta_\parallel = 10$ (at $t = 92.25/\Omega_H$), respectively. We find cigar-like magnetic peak structures which have large scale sizes in the parallel direction in each of the 3D model cases. During the nonlinear evolution of the mirror instability, the wavevector of the mirror mode wave changes to have a higher propagation angle [*Shoji et al.*, 2009]. In addition, in the perpendicular direction, the magnetic field has the symmetric property. Therefore, the cigar like structure appears in the 3D space. These results indicate that the magnetic dips are difficult to be generated in the 3D models.

In Figures 4.12a and 4.12b, we show time evolutions of the magnetic field and charge density of the protons, respectively, with the ion beta $\beta_\parallel = 10$ and the temperature anisotropy $T_\perp/T_\parallel = 2$. In the top panel of Figure 4.12a, we find the initial growth of the mirror instability. Through the middle and bottom panels of Figure 4.12a, we clearly find the coalescence of magnetic structures. On the other hand, in the top panel of Figure 4.12b, we find the charge density enhanced due to the diamagnetism in the mirror mode structures. Because of the increase of the degree of freedom in the perpendicular direction, there exists more neighbor magnetic dips (bubbles) than in the 2D model. As a result the merging of the diamagnetic currents takes place in these neighboring dips. As the mirror mode structure coalesces, the magnetic peaks appear similar to those in Figure 4.10. In Figure 4.12b, as the time proceeds, the charge density becomes larger around the magnetic peaks.

Figures 4.13a and 4.13b show the time evolution of the magnetic energy density and the temperature anisotropy of the protons. Times $t_1$, $t_2$, and $t_3$ correspond to the times of the top, middle and bottom panels of Figure 4.12, respectively. The evolution in the range of $0 < t < t_1$ is associated with the fast generation of the EMIC instability with
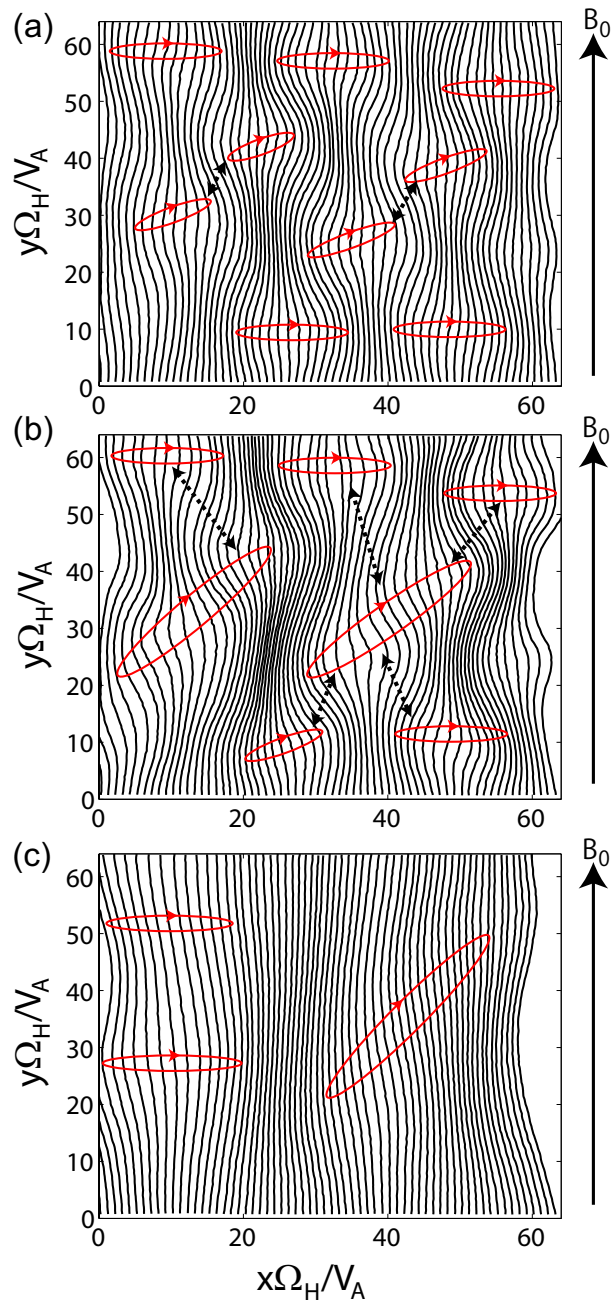
Figure 4.10: Spatial profiles of the magnetic field line (black lines) at (top) $t = 58.88/\Omega_H$, (middle) $t = 79.36/\Omega_H$, and (bottom) $t = 245.2/\Omega_H$, and the schematic plots of the diamagnetic currents which reduces the magnetic field density inside the magnetic dip regions (red lines). The attractive force between the current loops leads to coalescence of neighboring magnetic structures.
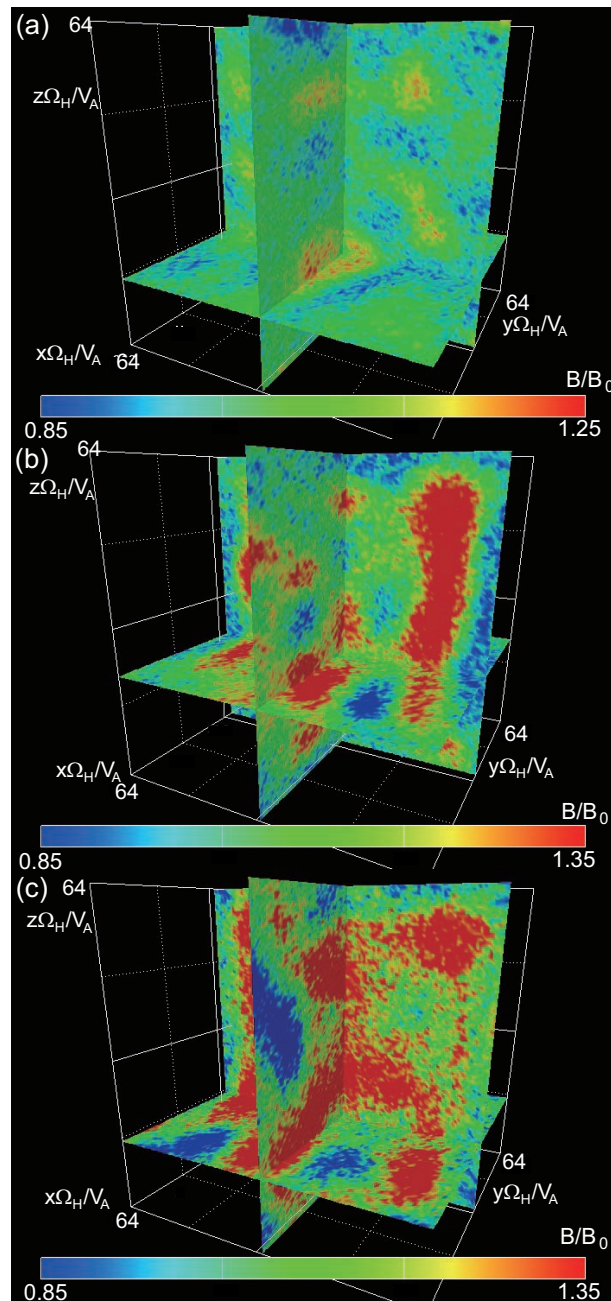
Figure 4.11: Mirror mode structures in the 3D models with the initial ion parameters $T_\perp/T_\parallel = 2$ and (a)$\beta_\parallel = 1$ at $t = 164/\Omega_H$ (b)$\beta_\parallel = 4$ $t = 164/\Omega_H$ (c)$\beta_\parallel = 10$ $t = 92.25/\Omega_H$.
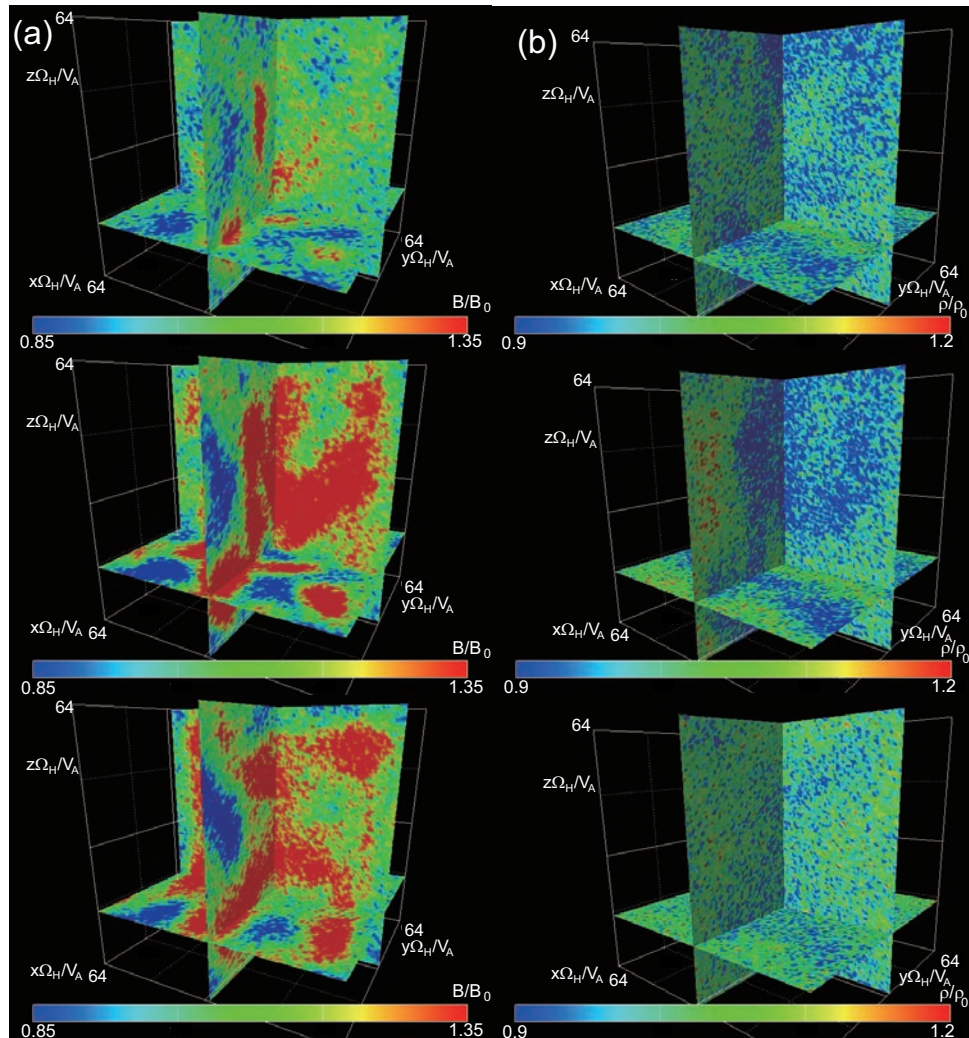
Figure 4.12: Cross sections of the 3D structures of (a) the magnetic field $B$ and (b) the charge density $\rho_i$. The top, middle, and bottom panels show the values at $t = 41/\Omega_H$, $t = 61.5/\Omega_H$, and $t = 92.25/\Omega_H$, respectively.

the larger initial growth rate. The magnetic energy becomes slightly larger while the temperature anisotropies of the particles are relaxed at the same time as shown in Figure 4.13b. In $t_1 < t < t_2$, the mirror instability grows dominantly, because the mirror mode structures stay in the system, while the temperature anisotropy is relaxed rapidly. After the saturation, $t > t_2$, the magnetic energy starts to decrease due to the particle heating during the coalescences of the magnetic structures as shown in Figure 4.8d. Because of the heating, the temperature anisotropy also keeps decreasing. As the magnetic peaks are generated, the magnetic field outside the magnetic peaks become smaller as we can see in Figure 4.12.

## 4.4 Summary and Comparisons with Observations

We compare the magnetic structures generated by the nonlinear evolution of the mirror instability between the 2D and 3D open boundary models. In the 2D model, fine structures of the magnetic dips are locally generated. On the other hand, in the 3D system, the magnetic peaks are found in the local regions. These magnetic structures mainly have parallel component $B_x$. We also performed the small size simulations with higher spatial resolution both in the 2D and 3D models with various ion beta values. We only find the magnetic dips in the 2D model with low ion beta ($\beta_\parallel \lesssim 1$). For other cases, the magnetic peaks appear. In the 3D model, we obtain the cigar-like magnetic peak structures as shown in Figures 4.11.

The mirror instability has the maximum growth rate in the higher wavenumbers (smaller wavelength) with the lower initial ion beta. In the lower ion beta conditions, most particles have small parallel velocities and thus they are trapped by the magnetic structures. Because the magnetic structures are uniform in the $z$ direction in the 2D models, they are easily trapped in the area with decreased magnetic field compared with those in the 3D models. Thus, the magnetic dips appear in the 2D models. In the higher ion beta cases, on the other hand, because of the stronger pitch angle scattering into the parallel direction and the large initial parallel velocities, the number of the particles which can be trapped by the magnetic structures become smaller. The coalescence of the magnetic dips takes place in both low and high beta cases. The coalescence is explained by the attraction of the diamagnetic current loops inside the magnetic dips (bubbles) as shown in Figure 4.10. Since the coalescence rate becomes larger as the mobility of the particles trapped inside the dips becomes larger, the currents merges effectively in the high beta cases.

The magnetic dips are observed near the magnetopause rather than near the bowshock
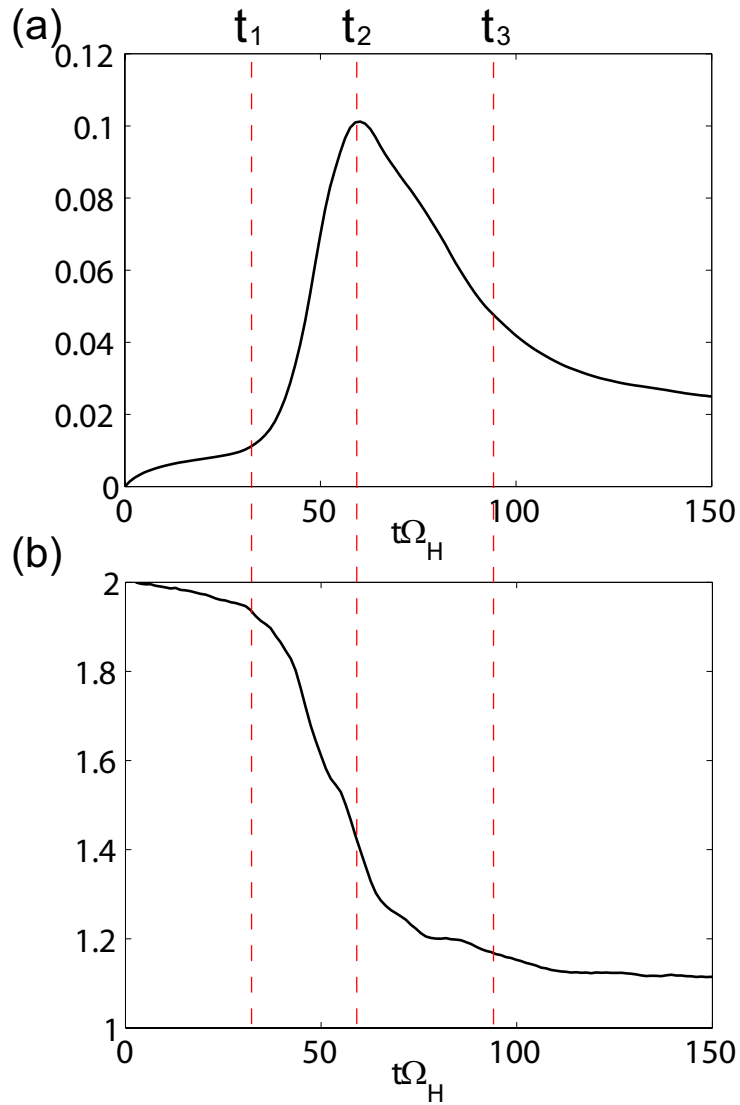
Figure 4.13: Time history of (a) the magnetic energy density and (b) the temperature anisotropy. Times $t_1 = 41/\Omega_H$, $t_2 = 61.5/\Omega_H$, and $t_3 = 92.25/\Omega_H$ correspond to the times of the top, middle, and bottom panels of Figure 4.12.

[*Souceck et al.*, 2008]. The simulation result that the magnetic dips are generated only in the 2D model of the low ion beta condition indicates the possibility that the magnetosheath near the magnetopause has a 2D spatial configuration for the mirror mode structure. Because of the existence of the magnetopause which works as a magnetic obstacle, the wavenumber vector in the normal direction to the magnetopause is restricted. Thus, the mirror instability is excited with the 2D spatial configuration. In the other region of the magnetosheath far away from the magnetopause, on the other hand, the spatial configuration becomes 3D, and the magnetic peaks are observed dominantly.

Whether the magnetic peaks or dips remain in the space is controlled by the local ion motions. When most of the particles are trapped by the mirror mode structures, the magnetic structures become magnetic dips. If the inhomogeneity of the background magnetic field reproducing the magnetosheath is assumed, the protons will become easy to be trapped in the magnetic structures and then the magnetic dips should be generated. The initial magnetic fluctuation also should be important to decide which magnetic structures are generated. In the case that the magnetic fluctuation have enough amplitude to trap most of protons around the region where the mirror instability takes place, the magnetic dips appear even if the protons have the larger ion beta or in the 3D spatial configuration. Such realistic analyses should be performed with the global models, and they remain as a future work.

# Chapter 5

# Electromagnetic Ion Cyclotron Triggered Emission in the Earth's Inner Magnetosphere

## 5.1    Introduction

In the Earth's inner magnetosphere, the inward transportation of the energetic protons takes place because of the magnetic reconnection in the magnetotail. The EMIC waves are usually observed inside the plasmapause (c.f. Figure 1.4). They cause the different nonlinear wave particle interactions from those in the other regions due to the existence of the Earth's eigen dipole magnetic field. Through the wave particle interactions, the nonlinear EMIC waves, which have rising tone spectra, are generated in the equatorial regions. The observed dynamic spectra is similar to that of the whistler-mode chorus emissions [e.g. *Santolik et al.*, 2003]. Recently, for the whistler-mode chorus emissions, the mechanisms of the nonlinear wave growth are studied via theory [e.g. *Omura et al.*, 2008, 2009], and particle-in-cell simulations [e.g. *Katoh and Omura*, 2007; *Omura et al.*, 2008; *Hikishima et al.*, 2009a, 2009b]. According to these investigations of the rising-tone emissions, it is expected that we can find some similar generation mechanisms of the EMIC triggered emissions.

In this chapter, we study the generation process of the rising tone emission of the EMIC waves so-called the EMIC triggered emissions. We perform a hybrid simulation with realistic parameters around the magnetic equator at $L \sim 4.3$, and compare the results with the observations and theory. In this section, we briefly review the previous studies on a spacecraft observation [*Pickett et al.*, 2010] and the nonlinear growth theory [*Omura et al.*, 2010]. We also show the linear dispersion relation of the EMIC waves. In Sections 5.2 to 5.4, we reproduce the EMIC triggered emission by the hybrid simulation with a cylindrical geometry. The drastic change of the velocity distribution function of

the energetic protons is also discussed. In Sections 5.5 and 5.6, we show the simulation results for the EMIC triggered emissions in the He$^+$ branch and the natural EMIC rising emissions which have been not observed yet. The possibility of the existence of these emissions is discussed. Finally, we conclude in Section 5.7.

### 5.1.1   EMIC triggered emissions observed by spacecrafts

ULF waves called Pc1-2 (0.1 Hz - 5 Hz) pulsations consisting of L-mode electromagnetic ion cyclotron (EMIC) waves have been observed on the ground [*Troitskaya*, 1961; *Tepley*, 1961] and in the Earth's magnetosphere at various latitudes by many spacecraft (e.g. GEOS  2 [*Roux et al.*, 1982], AMPTE CCE [*Anderson et al.*, 1992a, 1992b], Viking [*Erlandson et al.*, 1990, 1996; *Mursula et al.*, 1997], Freja [*Mursula et al.*, 1994], Polar [*Mursula et al.*, 2001; *Arnoldy et al.*, 2005], and Cluster [*Engebretson et al.*, 2007]). A recent Cluster observation around the equatorial region of the inner magnetosphere, which is shown in Figure 5.1, discovered coherent ULF rising-tone emissions [*Pickett et al.*, 2010] whose frequency characteristics are very similar to those of whistler-mode VLF chorus emissions [*Nunn et al.,* 1997; *Santolik et al.*, 2003; *Omura et al.*, 2008, 2009]. These ULF emissions arise from almost constant frequency waves lower than the proton cyclotron frequency $\sim$ 3.7 Hz. The observation result indicates that these rising-tone emissions always need the Pc1 (EMIC) pulsations as triggering waves. They call these chorus-like ULF emissions EMIC triggered emissions [*Pickett et al.*, 2010; *Omura et al.*, 2010].

### 5.1.2   Theoretical analyses on the EMIC triggered emissions

The generation mechanism of whistler-mode chorus emissions have been shown by *Omura et al.* [2008, 2009]. They have shown that a nonlinear absolute instability of coherent whistler-mode waves are caused by the formation of an electromagnetic electron hole [*Omura and Summers*, 2006] in the velocity phase space. In this section, we briefly introduce the generation mechanism of them based on the nonlinear wave growth theory that assumes the formation of an electromagnetic proton hole, because the EMIC triggered emissions have certain characteristics similar to whistler-mode chorus emissions.

   *Omura et al.* [2010] have developed a nonlinear wave growth theory which explains the generation of the EMIC triggered emissions. The relation between the frequency sweep rate and the normalized amplitude of the triggered wave at the equator $\Omega_{w0} = e/m_H B_{w0}$ is derived as

$$\frac{\partial \omega}{\partial t} = \frac{0.4 s_0 \omega}{s_1} \Omega_{w0}, \tag{5.1}$$
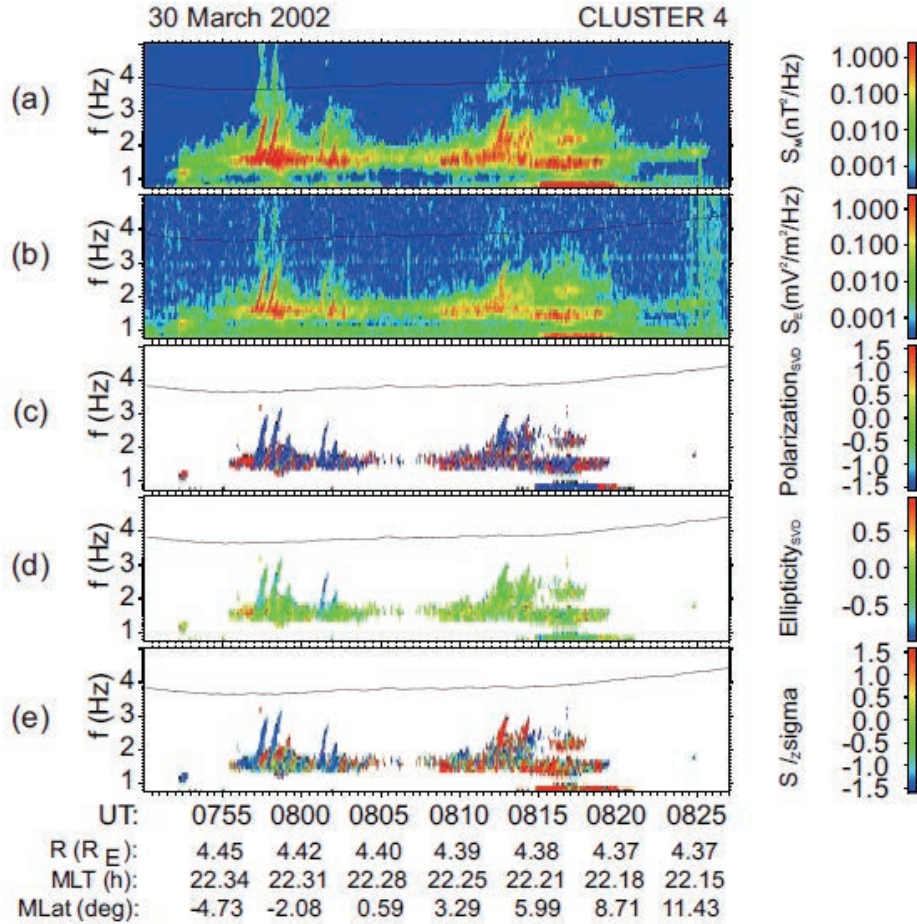
Figure 5.1: STAFF-SC and EFW data from CLUSTER 4 showing the Pc1 waves at $\sim$ 1.5 Hz and the EMIC triggered emission rising from $\sim$ 1.5 Hz to 3 Hz. (a) and (b): Sum of the power spectral densities of the three measured magnetic field components and two measured electric field components, respectively. (c) Sense of polarization using the method of singular value decomposition (SVD) of the magnetic spectral matrix [*Santolik et al.*, 2003], with the color blue indicating left-handed and red right-handed polarization. (d) Ellipticity of the magnetic field of the waves, also using the SVD method, with a value of 0 indicating linear polarization, -1 indicating left-hand circular polarization, and +1 indicating right-hand circular polarization. (e) Component of the Poynting vector parallel to the magnetic field $B_0$ normalized by its standard deviation, a negative value indicating opposite to $B_0$ and positive value in the same direction as $B_0$. The black line in all panels is the proton cyclotron frequency. At the bottom of the figure is a listing of the spacecraft distance, R (in RE), the magnetic local time, MLT (in hours), and the magnetic latitude, MLat (in degrees). [*after Pickett et al.*, 2010]
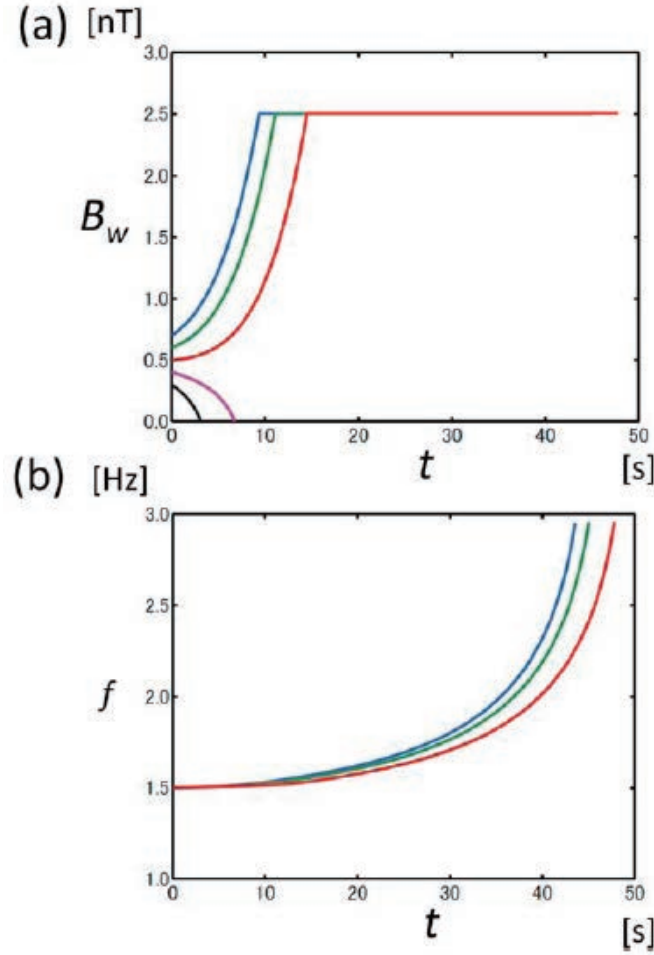
Figure 5.2: Solutions of EMIC chorus equations with the wave amplitude saturation at 2.5 nT for different initial wave amplitudes indicated by different colors: 0.3 (black), 0.4 (magenta), 0.5 (red), 0.6 (green), and 0.7 (blue) nT. (a) Wave amplitudes and (b) frequencies. [*Omura et al., 2010*]

where $s_0 = V_\perp/V_p$, $s_1 = (1 - V_R/V_g)^2$, $V_p = \omega/k$ is the phase velocity, $V_R = (\omega - \Omega_H)/k$ is the resonance velocity, $V_g = \partial\omega/\partial k$ is the group velocity. The normalized wave amplitude $\Omega_{w0}$ at the equator satisfies the following equation:

$$\frac{\partial \Omega_{w0}}{\partial t} = V_g \left[ \frac{Q\omega_{ph}^2}{2V_{t\parallel}} \left(\frac{V_{\perp 0}}{\pi}\right)^{3/2} \left(\frac{V_p \Omega_{w0}}{\omega}\right)^{1/2} \exp\left(-\frac{V_R^2}{2V_{t\parallel}^2}\right) - \frac{5V_p s_2 a}{s_0 \omega} \right] \Omega_H^2, \qquad (5.2)$$

where $s_2 = \left\{ V_\perp^2/(2V_p^2) + V_R^2/(V_p V_g) - V_R^2/(2V_p^2) \right\} \omega/\Omega_H - V_R/V_p$, $a$ is the coefficient in the nonlinear background magnetic field (2.27), $\omega_{ph}$ is the plasma frequency of the energetic protons, and $Q$ is a factor representing the depth of the proton hole which is predicted in *Omura et al.* [2010].

These equations have been solved with different initial wave amplitudes as shown in

Figure 5.1. Figure 5.1 indicates that there exists a threshold of the initial wave amplitude for the nonlinear wave growth. The theoretical threshold is given by

$$\frac{B_w}{B_0} > \frac{100\pi^3 V_p^3}{\omega \omega_{ph}^4 V_\perp^5} \left( \frac{as_2 V_\parallel}{Q} \right)^2 \exp\left( \frac{V_R^2}{V_\parallel^2} \right).$$

(5.3)

If the initial amplitude is lower than this threshold, the frequency do not become larger. Comparing the the solution of these equations with observations in Figure 5.1a, they show a good agreement. The saturation mechanism of the wave growth, however, has not been explained by the theory yet. Therefore, we need the self-consistent simulations to understand the mechanism.

### 5.1.3 Linear dispersion relation of EMIC wave

The linear dispersion relation of the L-mode EMIC wave [*Stix*, 1992] in the cold plasma approximation is given by

$$c^2 k^2 = \omega \left( \sum_s \frac{\omega_{ps}^2}{\Omega_s - \omega} - \frac{\omega_{pe}^2}{\Omega_e} \right),$$

(5.4)

where $c$, $\omega_{ps}$, and $\Omega_s$ are the speed of light, plasma and cyclotron frequencies of ion species $s$, respectively. The plasma and cyclotron frequencies of electrons are $\omega_{pe}$ and $\Omega_e$, respectively. Figure 5.3 shows the linear dispersion relation of the EMIC wave with the parameters used in the hybrid simulation. In this model, we assume three different species of cold ions. The top, middle, and bottom branches in the $\omega$-$k$ diagram correspond to EMIC modes bounded by the cyclotron frequencies of proton, helium and oxygen ions, respectively. The dashed lines show the frequency and wavenumber of the triggering waves. In the observations [*Pickett et al.*, 2010; *Omura et al.*, 2010], the frequency and the wavenumber of the EMIC triggered emissions varied in about 40 s in the ranges of the proton branch shown by the arrows (from dashed lines to dotted lines).

## 5.2 Reproduction of EMIC Triggered Emissions by Hybrid Simulations

To investigate the processes of the nonlinear wave growth including the saturation and associated pitch angle scattering of energetic protons, we need to analyze the time evolution of the interaction between the EMIC triggered emissions and the energetic protons quantitatively. The self-consistent hybrid simulations can treat the nonlinear wave-particle interactions in a real scale model.
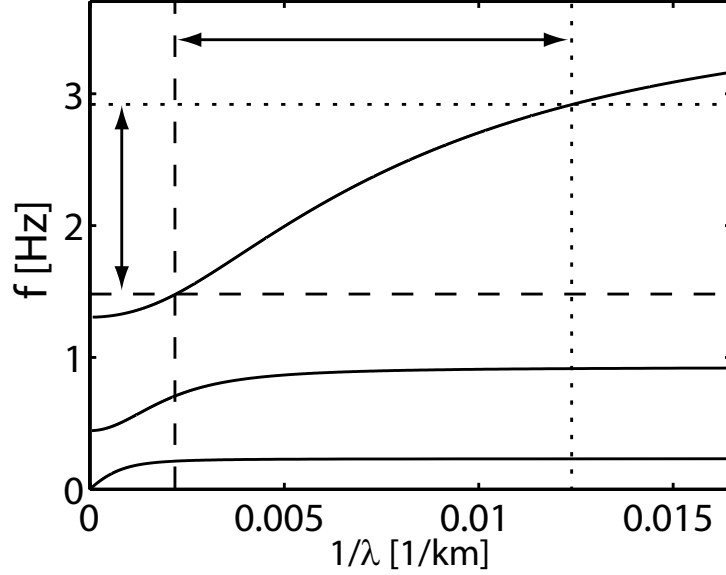
Figure 5.3: Dispersion relation of the L-mode EMIC wave with frequency $f = \omega/(2\pi)$ and wavenumber $1/\lambda = k/(2\pi)$. The dashed lines show the initial frequency and the wavenumber of the triggering wave. The dotted lines indicate the ending frequency and wavenumber of the triggered wave.

## 5.2.1    Simulation parameters

Table 5.1: Parameters of ion species.

| ion species | $V_{th\|\|}/c$ | $V_{th\perp}/c$ | $n_i/n_e$ | $q/m/(e/m_H)$ | $N_p/\text{cell}$ |
|---|---|---|---|---|---|
| $H^+$ | 0 | 0 | 0.7695 | 1.0 | 256 |
| $He^+$ | 0 | 0 | 0.0950 | 1/4 | 256 |
| $O^+$ | 0 | 0 | 0.0950 | 1/16 | 256 |
| energetic $H^+$ | 0.002 | 0.00267 | 0.0405 | 1.0 | 16,384 |

We use the hybrid simulation model with a cylindrical magnetic geometry that has been introduced in Section 2.5. The parameters of ions in the hybrid simulation are shown in Table 5.1, where $c$ is the speed of light in vacuum, $n_e = 178$ /cc is the density of the electron fluid, $e$ is the elementary charge, $m_H$ is the mass of the proton, $q/m$ is the charge-to-mass ratio of ions, and $N_p$ /cell is the average number of superparticles in a cell. Four kinds of ion species are assumed. Of the four, $H^+$, $He^+$ and $O^+$ are assumed as cold plasma components without thermal distributions. Their densities are assumed so that the wave dispersion relation gives the observed cut-off frequency.

According to the observational results [*Omura et al.*, 2010], the cyclotron and the plasma frequency of protons is assumed as 3.7 Hz and 353.4 Hz, respectively, at the

magnetic equator. Thus the amplitude of the ambient magnetic field is $B_{0eq} = 243$ nT, and the Alfven velocity is 443 km/s at the equator. The number of grids of the physical region is $n_x = 4,096$ with the grid spacing $\Delta x = 0.1 V_A/\Omega_H (= 1.9$ km), and the time step is $\Delta t = 0.004/\Omega_H (= 1.72 \times 10^{-4}$ s), where $V_A$ and $\Omega_H$ are the Alfven velocity and the cyclotron frequency of the cold protons at the equator. At each boundary, 1,024 grids are used as the dumping region. The frequency and the wavenumber of the triggering waves are taken from the observation as $(\omega_w, \ k_w) = (0.409\Omega_H, \ 0.27\Omega_H/V_A)$, which is $(f_w, \ k_w/(2\pi)) = (1.5$ Hz, $2.2 \times 10^{-3}$ /km) in the real unit system. The wave amplitude of the triggering wave is $B_w = 0.5$ nT. The theoretical amplitude threshold derived in *Omura et al.* [2010] is 0.41 nT. Thus, the wave amplitude is large enough to drive the nonlinear growth of the EMIC triggered emissions. In this model, we do not calculate the parallel motion of cold ions supporting the propagation of waves. We also note that the parallel components of the electric field and the current density are not solved, because we only have purely transverse waves propagating along the magnetic field line in the present simulation.

## 5.2.2 Simulation results: spatial and temporal evolutions of EMIC triggered emissions

A Fourier transform along the $x$ direction is applied to the transverse EMIC wave magnetic field to obtain $\boldsymbol{B}_\perp(k_x, \ t)$ at each time step. Using forward propagating waves $\boldsymbol{B}_f(k_x, \ t)$ and backward propagating waves $\boldsymbol{B}_b(k_x, \ t)$, which have positive and negative wavenumbers, respectively, we can express $B_z(k_x, \ t) = \overline{B_z}e^{ik_x x}$ as

$$\overline{B_z}e^{ik_x x} = \overline{B_f}e^{-i(\omega t - k_x x)} + \overline{B_b}e^{i(\omega t + k_x x)}. \tag{5.5}$$

Considering the polarization of the EMIC waves, the phase angle of $B_y$ delays $\pi/2$ from that of $B_y$. Thus $B_y(k_x, \ t) = \overline{B_y}e^{ik_x x}$ is described as

$$\overline{B_y}e^{ik_x x} = \overline{B_f}e^{-i(\omega t - k_x x - \frac{\pi}{2})} + \overline{B_b}e^{i(\omega t + k_x x - \frac{\pi}{2})} \tag{5.6}$$

$$= i\overline{B_f}e^{-i(\omega t - k_x x)} - i\overline{B_b}e^{i(\omega t + k_x x)}. \tag{5.7}$$

Setting $t = 0$ and solving for $\overline{B_f}$ and $\overline{B_b}$, we obtain the following equations.

$$\overline{B_f} = \frac{1}{2}(-i\overline{B_y} + \overline{B_z}) \tag{5.8}$$

$$\overline{B_b} = \frac{1}{2}(i\overline{B_y} + \overline{B_z}) \tag{5.9}$$

$$\tag{5.10}$$

Then we apply the inverse Fourier transform for the separated modes and we obtain the EMIC waves propagating with positive or negative wavenumbers. The wave amplitudes

of the forward and the backward waves are plotted as functions of $x$ and $t$ in Figure 5.4. From $t \sim 15$s, both forward and backward triggered waves start to be generated in the regions where there is no triggering wave in the same propagation direction.
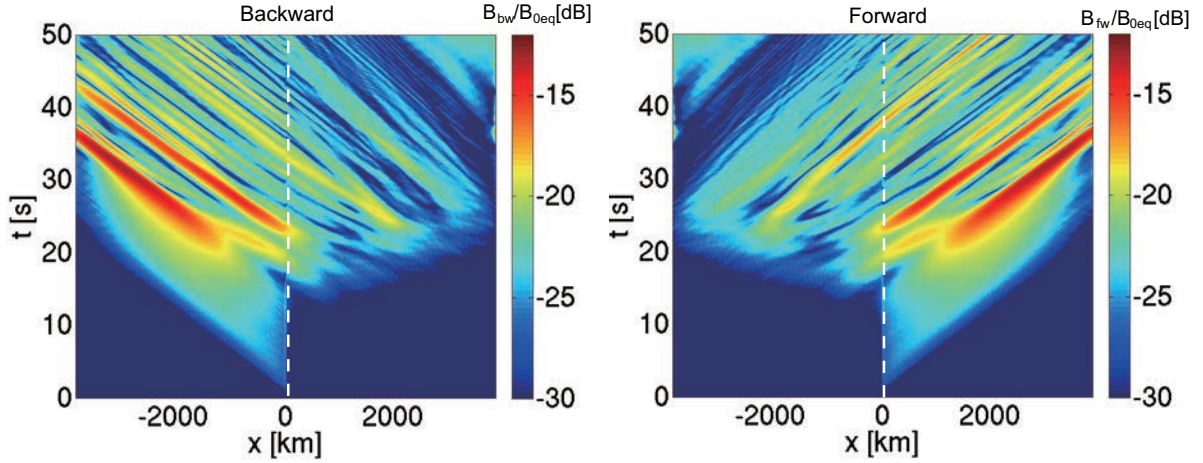


Figure 5.4: Spatial and temporal evolution of the wave amplitudes of the backward and forward propagating EMIC waves.

The distance between the generation region of the triggered waves and the equatorial region becomes larger as the emission proceeds. The forward and backward propagating triggering waves interact with the backward and forward moving energetic protons, respectively. The energetic protons interacting with the triggering waves are phase-organized in the transverse wave plane around the equatorial region. These protons are released at the equator and move into the region where there is no triggering wave. They form the transverse currents and generate seeds of the triggered emissions propagating in the opposite direction. The phase-organized protons move away from the equator and thus the regions where the triggered emissions are generated move with these particles.

The frequency sweep rate of the triggered wave at the equator is theoretically given by (5.1) [*Omura et al.*, 2010]. The time evolution of $B_{w0}$ at the equator is shown in Figure 5.5a. The triggered wave saturates around $t \sim 24$ s. We find a good agreement of the saturated amplitudes between the simulation and the observation results shown in Figure 7 of *Omura et al.* [2010]. We also show the frequency of the triggered wave as shown in Figure 5.5b. The frequency is calculated by integrating (5.1). The frequency starts to increase significantly when the wave amplitude start to grow. Even after the saturation, the frequency still increases.

We apply a Fourier transform in a limited time window for both forward and backward propagating waves at the equatorial region. Sliding the window from the initial time to
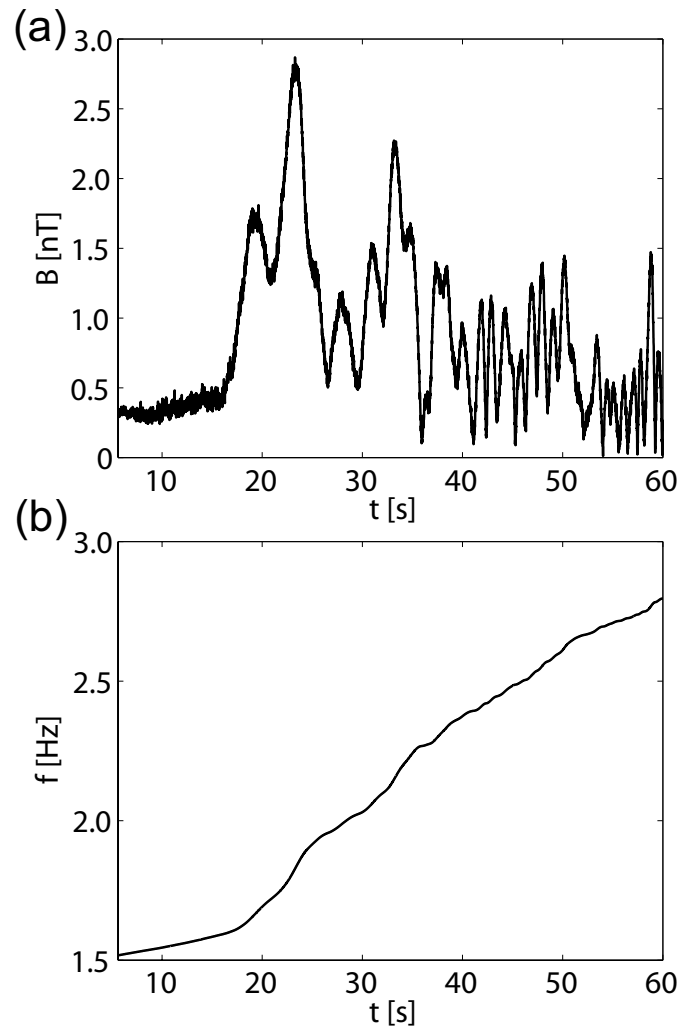
Figure 5.5: Time evolution of (a) the wave amplitude and (b) the theoretical frequency of the triggered wave at the equator.

the end of the simulation period, we obtain the time evolution of the wave spectra. The size of the window is taken as $t \sim 11.2$ s for a sufficient resolution in the frequency domain. Figures 5.6a and 5.6b show dynamic spectra of the forward and backward propagating waves around the equatorial region obtained by this method, respectively. In the case that we do not inject the triggering waves, although the result is not shown in this paper, there occurs no electromagnetic emission. On the other hand, as shown in Figures 5.6a and 5.6b, the EMIC triggered emissions are successfully reproduced both in the forward and backward propagating waves. This means that we need finite amplitude triggering waves to induce the EMIC triggered emissions. The duration of the rising tone emissions from 1.5 Hz to 3.0 Hz is 45 s in this case, showing a good agreement with the observation [*Pickett et al.*, 2010] and the theory [*Omura et al.*, 2010]. The frequency predicted by the

theory is shown by the white line in Figures 5.6a and 5.6b. We find a good agreement with the theory in the initial phase of the triggered emissions. Because this theory does not include the saturation mechanism, the theoretical frequency becomes different from that of the simulation result after $\sim 40$ s.
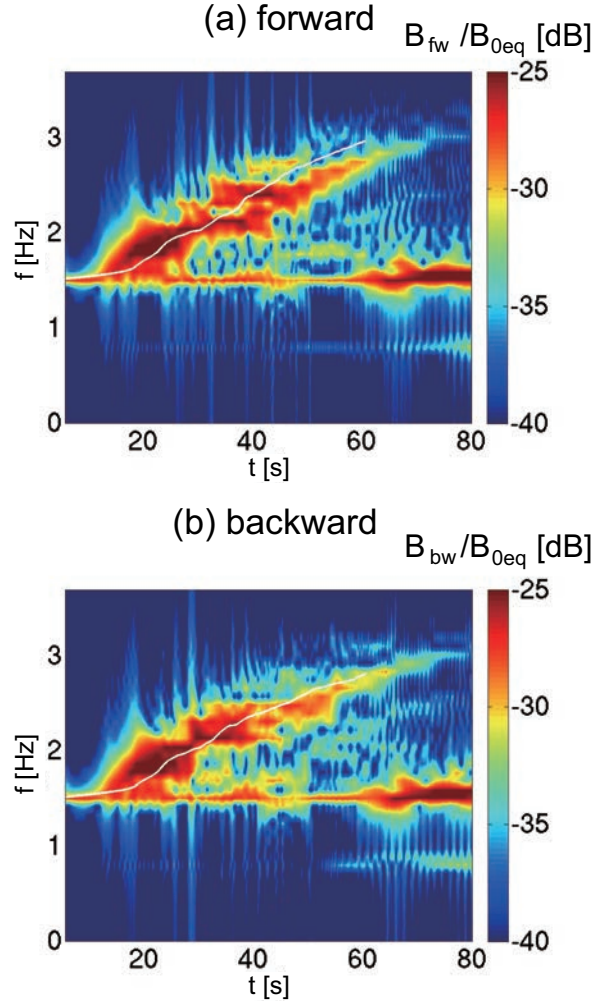


Figure 5.6: Dynamic spectra of the magnetic fields of (a) forward propagating wave with triggering wave and (b) backward propagating wave with triggering wave. The white lines show the theoretical frequency of the triggered waves.

Spatial profiles of wave frequency spectra of the forward propagating waves are plotted at different times in Figure 5.7. A spectrum at time $t$ is calculated in a time range $[t-5.6$ s $t+5.6$ s] which is the same as the time window used in Figure 5.6. In Figure 5.7a ($t = 5.6$ s) we only find the spectrum of the triggering wave. Around $t = 22.1$ s, shown in Figure 5.7b, a triggered emission emerges in the region before reaching the equator, where there is no triggering wave. This suggests that the emission is not generated directly by the

triggering wave. However the resonant current is formed by energetic protons that have
been phase-organized by the triggering wave and it induces the emission. As shown in
Figures 5.7c ($t = 38.8$ s) and 5.7d ($t = 55.3$ s), we can find that the triggered emissions
are generated progressively at different frequencies before reaching the equator, and that
they grow in amplitude as they propagates away from the equator. The critical distance
$h_c$, at which the temporal and spatial derivatives in the inhomogeneity ratio [*Omura et
al.*, 2010] become equal, is estimated as $h_c \simeq 320$ km. In the regions beyond the critical
distance ($|x| > h_c$), the triggered waves undergo convective growth driven by the gradient
of the magnetic field.
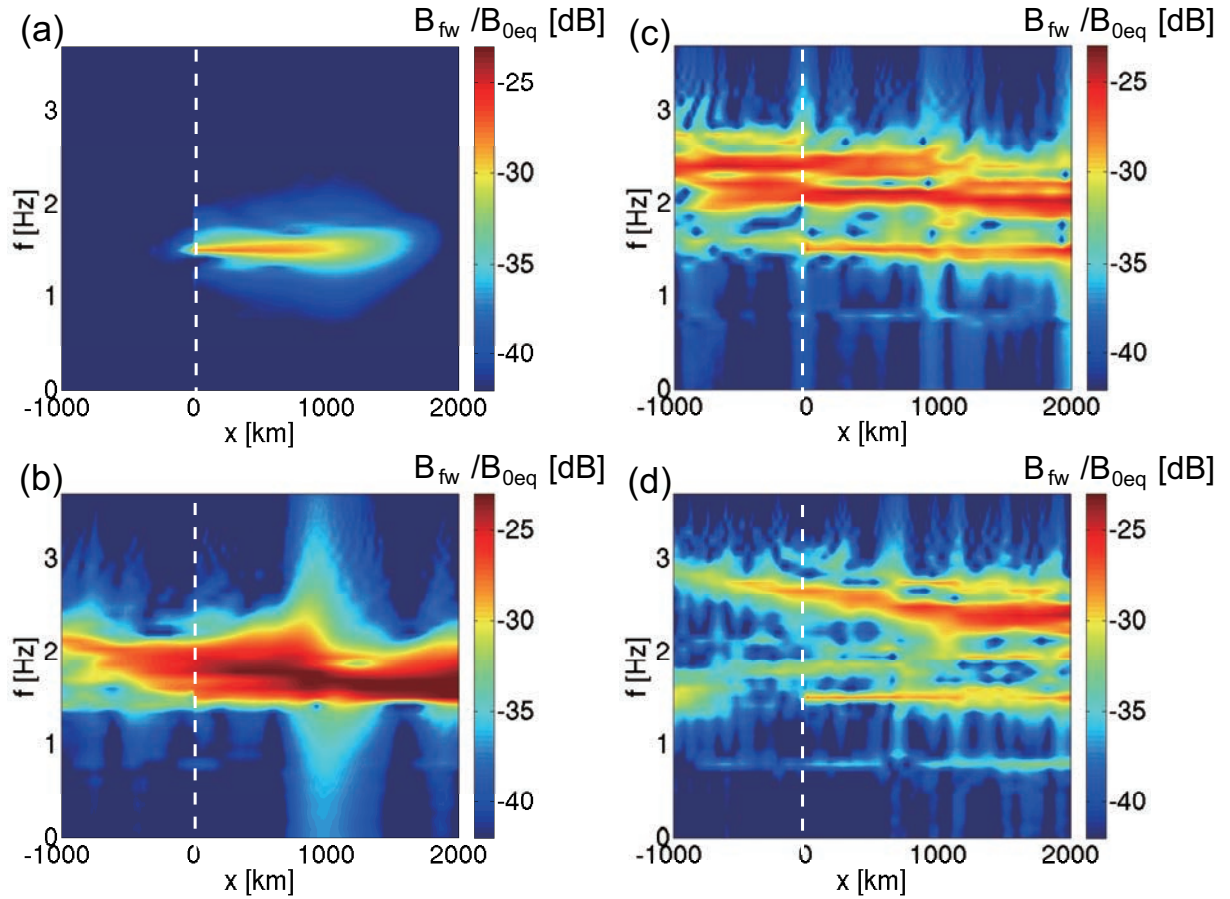


Figure 5.7: Spatial profiles of the wave spectra of the magnetic field at (a) $t = 5.6$ s, (b)
$t = 22.1$ s, (c) $t = 38.8$ s, and (d) $t = 55.3$ s.

## 5.3    Time Evolution of Velocity Distribution Function of Energetic Protons

Figure 5.8 shows the velocity distribution functions of energetic protons around the equatorial region at different times. The values of the velocity distribution functions are normalized by the maximum value of the initial velocity distribution function $f_{0M}$. We show these panels at equal time intervals of 26.4 s. The white solid lines indicate the resonance velocities $V_R$ of the forward ($k > 0$) and backward ($k < 0$) propagating triggered waves. We also show the resonance velocities of the forward and backward triggering waves ($= \pm 970$ km/s) by white dashed lines. The initial distribution function is shown in Figure 5.8a. As the EMIC triggered emissions evolve in time, the resonant velocities become smaller in magnitude because of the increasing frequencies and wavenumbers. Thus the energetic protons with smaller parallel velocities are strongly scattered as shown in Figures 5.8b, 5.8c, and 5.8d. At $t = 26.4$ s (shown in Figure 5.8b) the triggered waves saturate, we can find proton holes around the resonance velocities of the triggered wave. The trapping velocity of the triggered waves $V_{tr} = \sqrt{V_\perp \Omega_w / k}$ approaches to $\sim 80$ km/s in Figure 5.8b. Energetic protons satisfying $V_R - V_{tr} < v_\parallel < V_R + V_{tr}$ are strongly scattered in their pitch angles. As we find in Figure 5.8c, the proton holes are gradually filled out by the scattered resonant protons. The frequencies of the triggered waves still increase and thus the core part of the distribution function of the energetic protons is diffused. Finally, as shown in Figure 5.8d after the triggered waves saturate and disappear, the distribution function becomes stable. At this time, the whole core of the initial distribution disappears. A substantial number of the energetic protons in a wide range of energy are scattered through the generation process of the triggered emissions. Thus the distribution of the energetic protons shows a very different distribution from the initial one, indicating strong pitch angle scattering by the triggered emissions over one cycle of the nonlinear triggering process.

To understand the time evolution of the proton holes, we show fine time evolution of the distribution function during $17.6$ s $\leq t \leq 35.2$ s in Figure 5.9. Figure 5.9a shows the distribution function around the time when the triggered emission starts. At this time, the pitch angles of the energetic protons around the resonance velocities of the forward and backward propagating triggering waves are scattered. We continuously inject the triggering waves at the equator and the particles around the resonance velocities interact with the triggering waves. We also find significant depletion of energetic protons due to the proton holes at the resonance velocities in Figures 5.9b, 5.9c, and 5.9d. Through the inward motion of the proton holes, the core part of the velocity distribution erodes
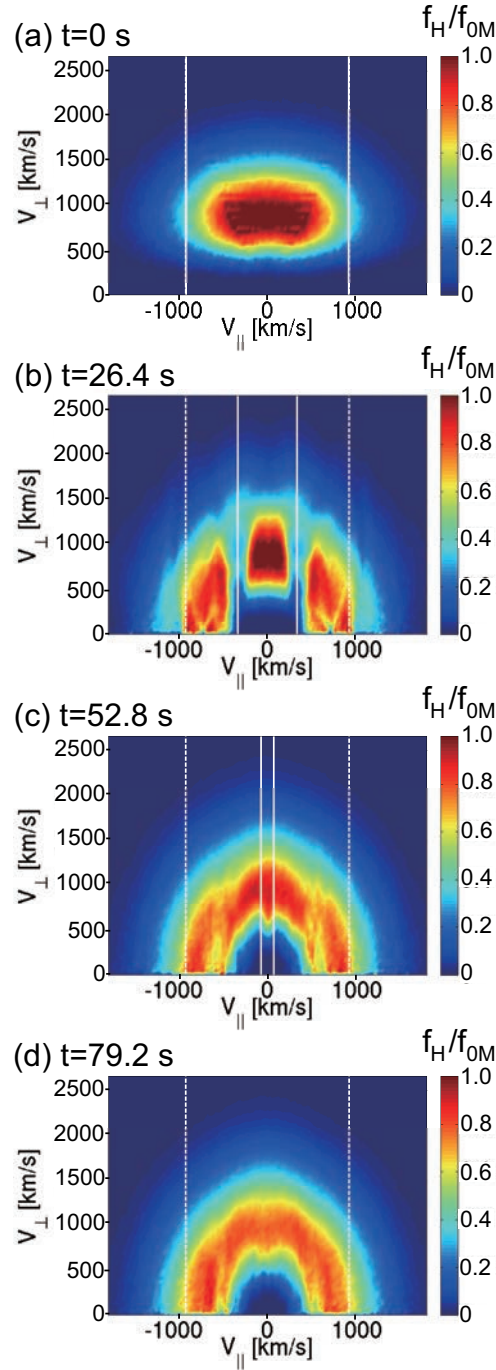
Figure 5.8: Velocity distribution functions $f_H(v_\parallel, v_\perp)$ of energetic protons at (a) $t = 0$ s, (b) $t = 26.4$ s, (c) $t = 52.8$ s, and (d) $t = 79.2$ s normalized by the maximum value of the initial velocity distribution function $f_{0M}$. The white dashed lines show the resonance velocities of forward and backward triggering waves. The white solid lines show those of forward and backward triggered waves.
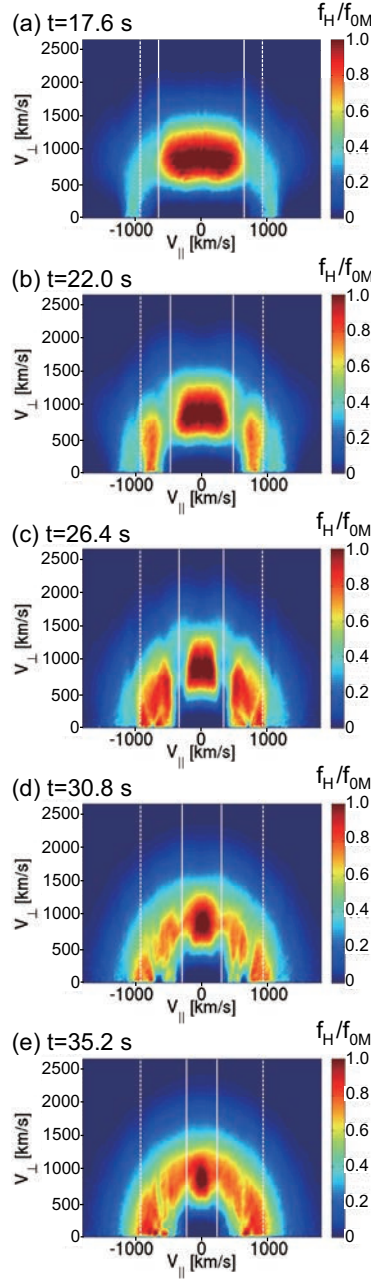
Figure 5.9: Velocity distribution functions $f_H(v_\parallel, v_\perp)$ of energetic protons at (a) $t = 17.6$ s, (b) $t = 22.0$ s, (c) $t = 26.4$ s, (d) $t = 30.8$ s, and (e) $t = 35.2$ s normalized by the maximum value of the initial velocity distribution function $f_{0M}$. The white dashed lines show the resonance velocities of forward and backward triggering waves. The white solid lines show those of forward and backward triggered waves.

gradually in time, resulting in a pancake distribution near a pitch angle $\alpha = 90°$. As
shown in Figures 5.9b - 5.9e, the proton holes become smaller, when the amplitudes of
the triggered waves decrease after the saturation around $t = 24$ s.
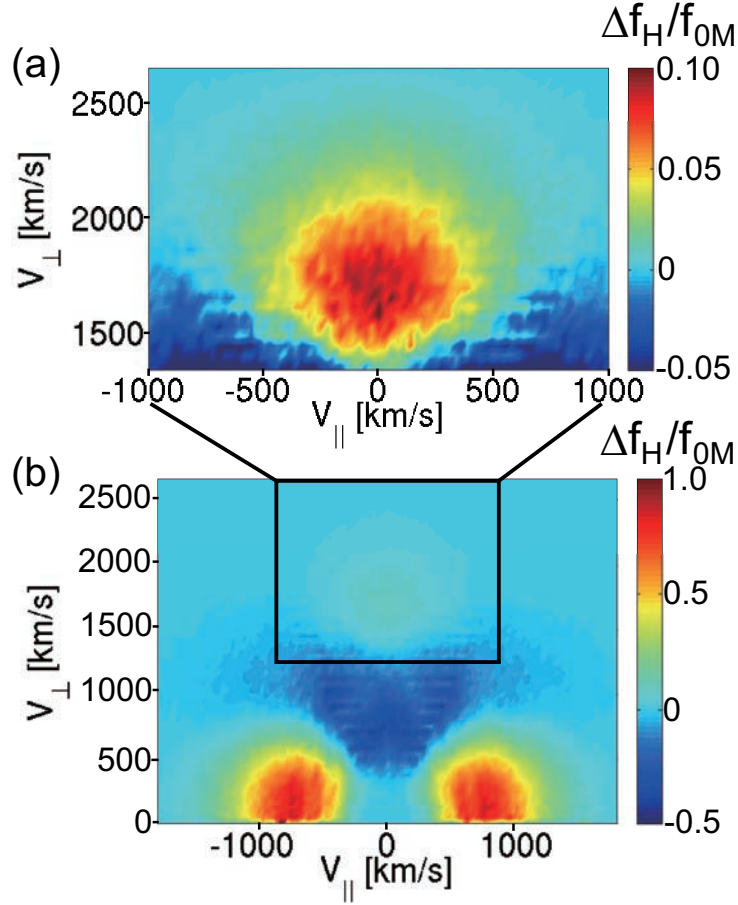


Figure 5.10: Difference of the velocity distribution functions of energetic protons, $\Delta f_H = f_H|_{t=79.2s} - f_H|_{t=0s}$, in regions where (a) 1,600 km/s $< V_\perp <$ 2,600 km/s and $|V_\parallel| < 1,000$ km/s and (b) 0 km/s $< V_\perp <$ 2,600 km/s and $|V_\parallel| < 1,600$ km/s. The values of $\Delta f_H$ are normalized by the maximum values of the initial velocity distribution function $f_{0M}$.

Comparing Figures 5.8a and 5.8d, we find that the majority of energetic protons
are scattered in their pitch angles. However, some of energetic protons are accelerated
toward higher pitch angles. We define the difference of the velocity distributions as
$\Delta f_H = f_H|_{t=79.2s} - f_H|_{t=0s}$ and plot it in Figure 5.10. Figure 5.10a shows the distribution
of the accelerated particles which have $V_\perp > 1,600$ km/s. The negative value in Figure
5.10b indicates the particle loss. Most of the lost particles are strongly scattered to lower
pitch angles losing the energy while some of them are accelerated to higher pitch angles.
From Figure 5.10a, we can find a clear increase of energetic protons around pitch

angles $\sim 90°$. We integrate the increased density of the energetic protons which have $V_\perp > 1,600$ km/s. During the generation process of the triggered emissions, nearly 2.4% of energetic protons in the equatorial region are accelerated. The acceleration is due to phase trapping of resonant protons guided from the upstream regions toward the equator along the resonance velocity, which decreases to the lower value in magnitude. Because of the energy transfer from the waves to the accelerated protons, the nonlinear wave growth near the equator is saturated, and triggered waves are subsequently damped.

A large number of particles are scattered by the triggered emissions and some of them fall into the loss cone as shown in Figure 5.10b. The loss cone angle at the equator $\alpha_l$ [*Baumjohann and Treumann*, 1997] is defined as

$$\sin^2 \alpha_l = \frac{1}{\sqrt{4L^6 - 3L^5}} \quad . \tag{5.11}$$

All of the protons with pitch angles $\alpha < \alpha_l$ precipitate into the atmosphere. Assuming $L = 4.3$, we have $\alpha_l = 4.8°$, and we can estimate the amount of the precipitating protons from Figure 5.10b. We integrate the density difference of the energetic protons over the range of pitch angle $\alpha < \alpha_l$ in the velocity space. Through the EMIC triggered emission, 6.5% of the energetic protons precipitate into the atmosphere. The averaged proton energy at $t = 79.2$ s in the loss cone is 4.54 keV. Precipitation of these energetic particles can cause the proton aurora around the polar region [*Montbriand,* 1971; *Fukunishi,* 1975; *Spasojevic et al.*, 2004].
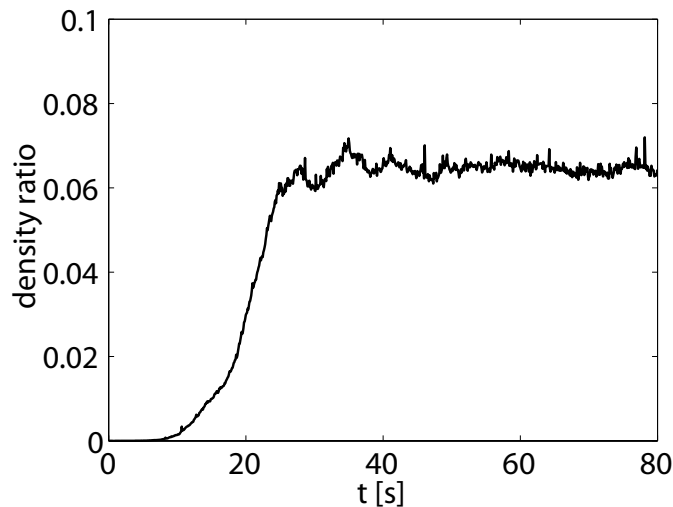


Figure 5.11: Time evolution of the amount of the energetic protons with smaller pitch angles than the loss cone angle.

Figure 5.11 shows the time evolution of the amount of the energetic protons which

have the smaller pitch angles than the loss cone angle 4.8 degree at L=4.3 at the equator. The value is normalized by the number of the total energetic protons around the equatorial region. The number of precipitating protons saturate around $t \sim 25$ s. This time corresponds to the saturation time of the EMIC triggered emission which can be identified in Figure 5.5a and the number does not change after the saturation. Thus, the most of the precipitation is caused before the saturation of the triggered emission. At t=79.2 s, after the triggered emission disappears, 6.5% of the energetic protons become in the loss cone.
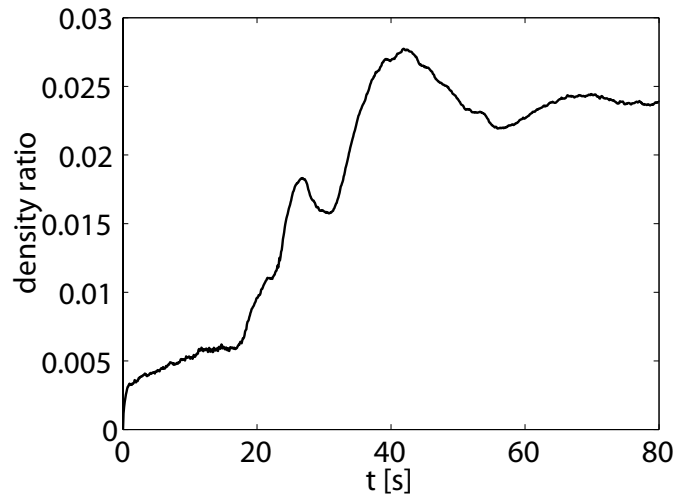


Figure 5.12: The time evolution of increased amount of the energetic protons with the velocity $V_\perp > 1,600$ km/s around the equatorial region.

The time evolution of increased amount of the energetic protons which have $V_\perp > 1,600$ km/s around the equatorial region are shown in Figure 5.12. The value is normalized by the total density of the energetic proton in the same region. The amount of the energetic protons increases significantly from around the saturation of the triggered emissions ($t \sim 25$ s). This is because the acceleration is controlled by the saturation and dissipation mechanism of the EMIC triggered emissions. The value also saturates around $t \sim 60$ s when the EMIC triggered emissions almost disappear as show in Figure 5.6.

## 5.4 Parametric Analyses of EMIC Triggered Emissions

To understand the dependency of the frequency sweep rate and the maximum frequency of the EMIC triggered emissions on the amplitude of the triggering waves and the density

of the energetic protons, we also performed the parametric analyses on the density ratio of the energetic protons to the total proton $n_{hH}/n_H$ and the amplitude of the triggering waves $B_{w0}$. Table 5.2 shows the density ratio of the energetic particles to the protons and the amplitude of the triggering waves for run (a) to run (f). For other parameters, we used the same values as the previous simulation. Run (d) correspond to the parameters of the previous simulation in Sections 5.2.1 and 5.3.

Table 5.2: Parameters for run (a) to run (f).

| run | $n_{hH}/n_H$ | $B_{w0}$ [nT] |
|---|---|---|
| run (a) | 0.050 | 0 |
| run (b) | 0.010 | 0.50 |
| run (c) | 0.025 | 0.50 |
| run (d) | 0.050 | 0.50 |
| run (e) | 0.100 | 0.25 |
| run (f) | 0.050 | 5.00 |

Figures from 5.13a to 5.13f show the dynamic spectra at the equatorial regions of run (a) to run (f), respectively. Figure 5.13d shows the result in run (d), which are the same parameters as in Section 5.2. In Figure 5.13a, we have no triggering waves, and there are no wave emissions. It indicates that the velocity distribution function of the energetic plasmas is stable. The triggering waves are necessary to drive the EMIC triggered emissions. The nonlinear wave growth theory [*Omura et al.*, 2010] indicates the existence of the threshold for the nonlinear growth of the EMIC triggered emissions. Figure 5.13b shows the result near the threshold. We can find the dynamic spectra of the EMIC triggered emission. However, the rising of the frequency stops at smaller level. This is because of the lack of the free energy of the energetic protons. As the density becomes larger, the frequency rises larger as shown in Figure 5.13c. The frequency of the triggered emission reaches to $\sim 3.0$ Hz. Assuming more density of the energetic protons, there arise the multiple EMIC triggered emissions as shown in Figure 5.13e. As we discussed in later chapter, another type of the EMIC wave which have a constant frequency can be found below the proton cyclotron frequency. Assuming large amplitude EMIC triggering waves, as shown in Figure 5.13f, the EMIC triggered emission disappears. From the theoretical analyses on the whistler-mode chorus emissions [*Katoh and Omura*, 2011] indicate that there is the critical range for the initial wave amplitude to start the triggered emissions.
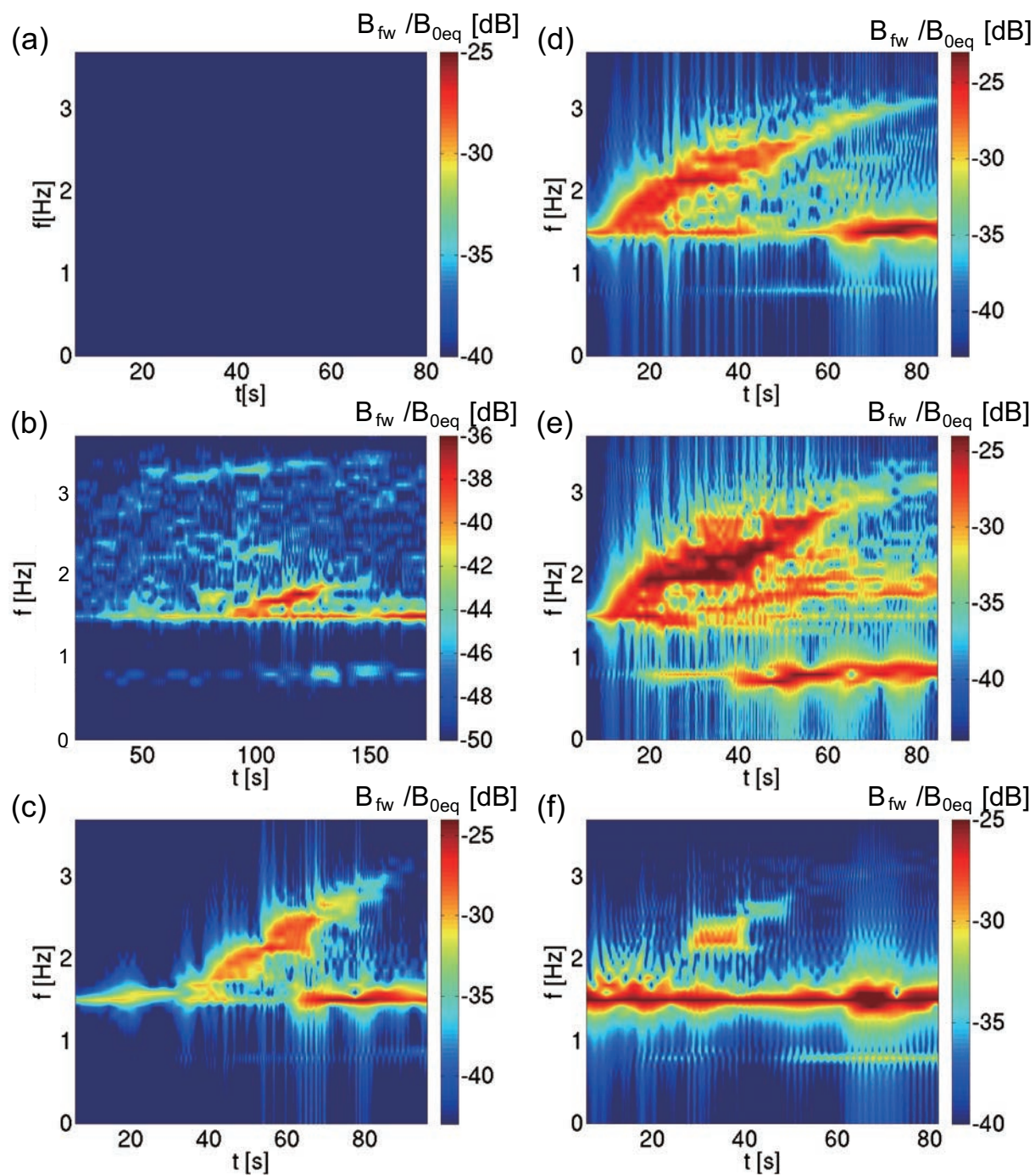
Figure 5.13: Dynamic spectra of the EMIC triggered emissions with different parameters from run (a) to run (f).

## 5.5   EMIC Triggered Emission in the Helium Branch

As we can see in Figure 5.3, there also exists positive gradient of the dispersion relation of EMIC waves in the $He^+$ and $O^+$ branches. It indicates that the possibility of the existence of the EMIC triggered emissions with rising frequency in these branches. The existence of the triggered emissions in the different branches suggests the scattering of the energetic protons in the different energy range because of the difference of the resonance velocity. They will contribute to the proton aurora in different energy ranges. In this section, we perform the hybrid simulation to show the EMIC triggered emission in the $He^+$ branch can be caused in the inner magnetosphere. The spatial parameters of the simulation are the same as those in the previous simulations. The thermal velocities in the parallel and perpendicular directions, the density ratio, the charge-to-mass ratio, the number of the particles of each ion species in a cell are shown in Table 5.3. The frequency and the wavenumbers of the triggering waves are $f_w = 0.56$ Hz and $k_w/(2\pi) = 1.1 \times 10^{-3}$ /km, respectively. The wave amplitude of the initial triggering wave is 0.05 nT. The theoretical threshold of the triggered emission with the parameters shown in Table 5.3 is $B_w = 0.48$ nT.

Table 5.3: Parameters of ion species for the simulation of EMIC triggered emissions in the $He^+$ branch.

| ion species | $V_{th\parallel}/c$ | $V_{th\perp}/c$ | $n_i/n_e$ | $q/m/(e/m_H)$ | $N_p$/cell |
|---|---|---|---|---|---|
| $H^+$ | 0 | 0 | 0.8019 | 1.0 | 256 |
| $He^+$ | 0 | 0 | 0.0950 | 1/4 | 256 |
| $O^+$ | 0 | 0 | 0.0950 | 1/16 | 256 |
| energetic $H^+$ | 0.008 | 0.01068 | 0.0081 | 1.0 | 16,384 |

Figure 5.14 shows the dynamic spectra of the magnetic field of the forward propagating wave in the $He^+$ branch. We can find the rising tone spectra below the $He^+$ cyclotron frequency (white dashed line) after $t \sim 70$ s. The wave amplitude of the forward propagation waves are shown in Figure 5.15. The EMIC triggered emission saturates at around $t \sim 105$ s. Before the nonlinear wave growth with the rising frequency, the linear growth of the EMIC wave (the triggering wave) takes place. Around $t \sim 85$s in Figure 5.16, the wave amplitude reaches at the threshold of the EMIC triggered emission (shown by the dashed line in Figure 5.15) as we can see in Figure 5.15. After that, the frequency start to become larger as shown in Figure 5.14. The frequency saturates at 0.8 Hz at $t \sim 130$ s. The frequency becomes larger from 0.56 Hz to 0.8 Hz in 45 s. The second EMIC triggered emission can be observed from $t \sim 110$ s. We also find the EMIC wave emission below the
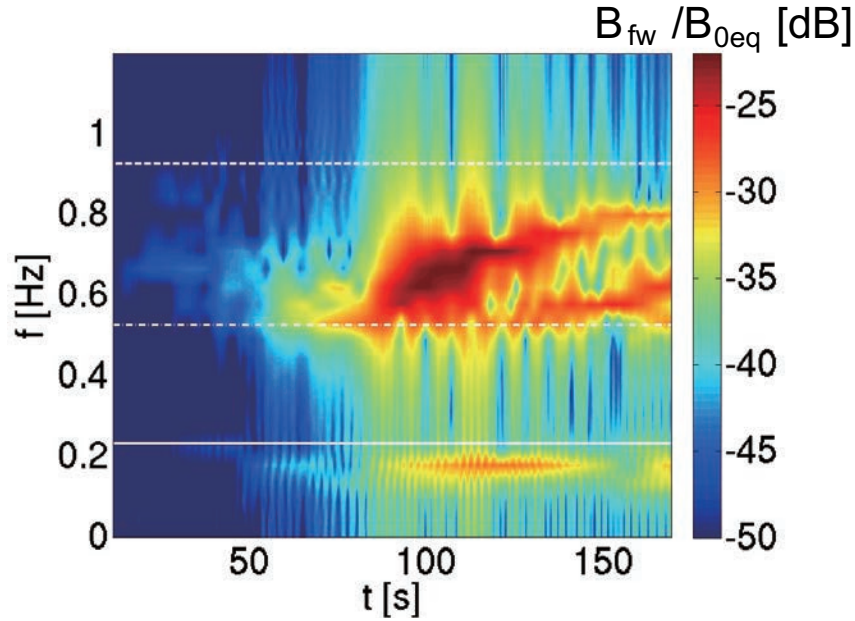
Figure 5.14: Dynamic spectra of the magnetic fields of forward propagating wave with triggering wave. The white solid, dash-dotted, and dashed lines show the cyclotron frequency of $O^+$, the theoretical frequency of the triggered waves, and the cyclotron frequency of $He^+$, respectively.

cyclotron frequency of the $O^+$ branch. This emission is caused by the same mechanism as that shown in Figure 5.13e. The detail of the generation mechanism of this lower branch wave is discussed in the next chapter.

Theoretical analyses [*Omura et al.*, 2010] of the frequency sweep rate and the nonlinear growth are performed by solving (5.1) and (5.2) with the different triggering wave amplitude. We assume the numerical saturation at $B_w = 3.5$ nT, which is obtained from the hybrid simulation result shown in Figure 5.15. The wave amplitude and the frequency sweep rate of the EMIC triggered emissions at the equator for the different amplitude are shown in Figures 5.16a and 5.16b, respectively. In the cases that the initial amplitudes are assumed as lower than the threshold, the triggered emissions do not take place and the frequency cannot become larger. With the larger initial amplitude than the threshold, we can find the nonlinear wave growth in Figure 5.16a, and the rising frequency in Figure 5.16b. Comparing the theory with the simulation result, the frequency sweep rate of the triggered emission from 0.56 Hz to 0.8 Hz shows a good agreement.

The time history of the velocity distribution functions of the energetic protons around the equatorial region are shown in Figure 5.17. In Figure 5.17a, we show the initial velocity distribution function. Because the resonance velocity of the triggering wave
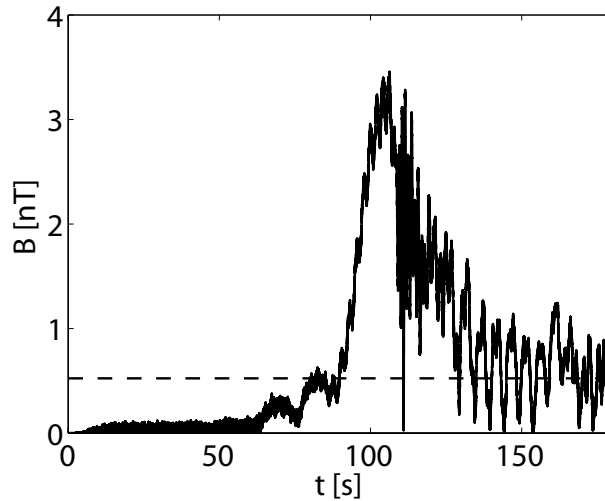
Figure 5.15: Time evolution of the wave amplitude at the equator. The dashed line shows the theoretical threshold of the EMIC triggered emission $B_w = 0.48$ nT.

$V_R = (\omega - \Omega_H)/k = 2,900$ km/s is larger than that of the triggering waves for the EMIC triggered emissions in H$^+$ branch ($V_R = 970$ km/s), the energy range of the scattered protons become larger. In Figure 5.17b, the energetic protons around the resonance velocity of the triggering waves are scattered. The proton holes around the resonance velocity of the triggered emissions are found in Figure 5.17c. The inward motion of the ion holes of the triggered emissions in the He$^+$ branch are also found in the velocity distribution function through Figures 5.17c, 5.17d and 5.17e.

The pitch angle of the energetic protons are scattered by the triggered emission and some of the protons go into the loss cone (4.8 degree). The amount of the protons in the loss cone is estimated by the same way as Section 5.3. The triggered emissions in the He$^+$ branch scatter 6.4 % energetic protons around the equatorial region into the loss cone at $t \sim 150$ s. The averaged energy of the protons which go into the loss cone is 90 keV.

## 5.6 Natural EMIC Rising Emissions

In the previous sections, we reproduced the rising tone emissions triggered by the small amplitude waves. In the inner magnetosphere, there also exist rising tone emissions without triggering waves which come from the other regions. In VLF range, the whistler-mode chorus emissions have been observed in the inner magnetosphere [e.g. *Santorik et al.*, 2003]. They are also generated through the nonlinear interactions between the whistler-mode waves and the energetic electrons [*Omura et al.*, 2008], although the triggering waves do not observed at the same time. They are generated by the anisotropic velocity
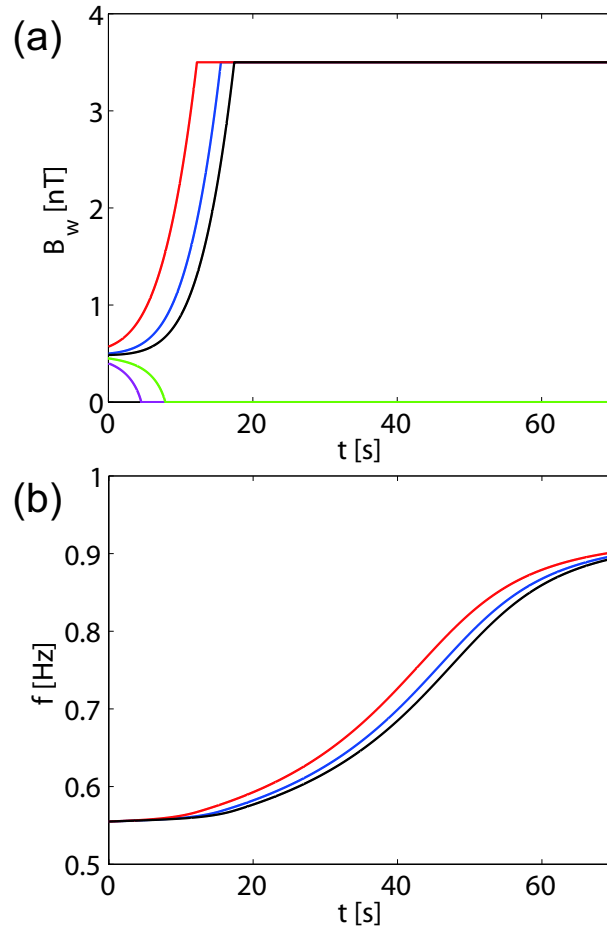
Figure 5.16: Theoretical analyses of (a) the wave amplitude and (b) the frequency sweep rate of the EMIC triggered emissions below the $He^+$ cyclotron frequency at the equator. The magenta, green, black, blue, and red lines show the results with the amplitude of the triggering waves 0.4 nT, 0.45 nT, 0.49 nT, 0.5 nT, and 0.57 nT, respectively.

distributions of the energetic electrons. By the same mechanism, the rising tone EMIC waves, which we call "natural EMIC rising emissions", should be generated by the large temperature anisotropy of the energetic protons. The emissions cause the spontaneous rising frequency of the triggered waves without the triggering waves. In this section, we discuss the possibility of the existence of the natural EMIC rising emissions in the Earth's inner magnetosphere without the external triggering waves.

We use the same geometry as the previous simulations for the triggered emissions. We assume the L value as $L = 8.2$. With this parameter, the cyclotron frequency of the protons at the equator becomes 0.53 Hz according to the following relation[*Baumjohann*
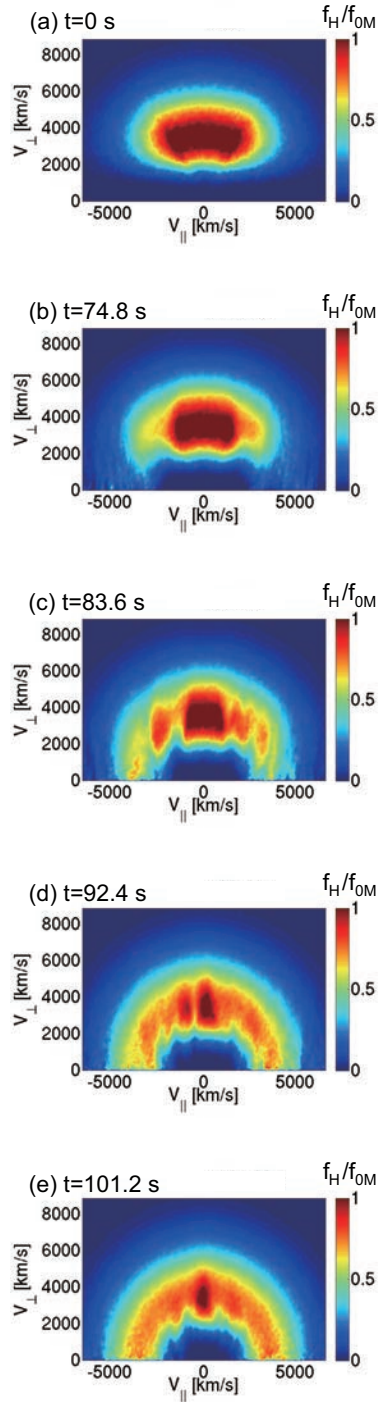
Figure 5.17: Velocity distribution functions $f_H(v_\parallel,\ v_\perp)$ of energetic protons at (a) $t = 0$ s, (b) $t = 22.0$ s, (c) $t = 26.4$ s, (d) $t = 30.8$ s, and (e) $t = 35.2$ s normalized by the maximum value of the initial velocity distribution function $f_{0M}$. The white dashed lines show the resonance velocities of forward and backward triggering waves. The white solid lines show those of forward and backward triggered waves.

*and Treuman*, 1997]

$$\frac{f_{L=8.2}}{f_{L=4.3}} = \left(\frac{B_{0eq}|_{L=4.3}}{B_{0eq}|_{L=8.2}}\right)^3, \tag{5.12}$$

where $f_{L=8.2}$ and $f_{L=4.3}$ are the cyclotron frequency of the protons at the equator in $L = 8.2$ and $L = 4.3$, respectively, and $B_{0eq}|_{L=8.2}$ and $B_{0eq}|_{L=4.3}$ are the background magnetic field at the equator in $L = 8.2$ and $L = 4.3$, respectively. The initial velocity distribution function of the energetic protons has an anisotropy $T_\perp/T_\parallel = 4.0$. The initial thermal velocities in parallel and perpendicular directions are $V_{th\parallel}/c = 0.002$, $V_{th\parallel}/c = 0.004$, respectively. The density of the cold protons, helium, oxygen, and energetic protons are $0.800n_e$, $0.095n_e$, $0.095n_e$, and $0.010n_e$, respectively.
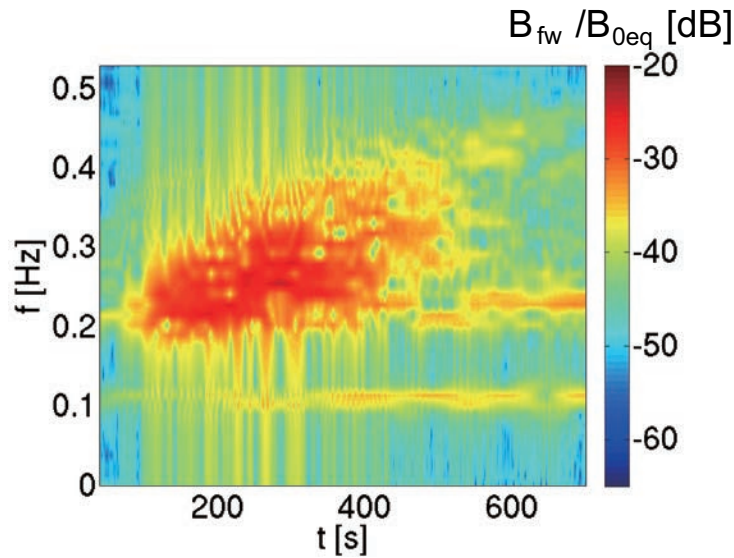


Figure 5.18: Dynamic spectra of the magnetic fields of the forward propagating waves.

Figure 5.18 shows the dynamic spectra of the forward propagating waves around the equatorial region. We can find the rising tone emissions, which we call natural EMIC rising emission, in Figure 5.18. Because the initial velocity distribution function of the energetic protons in this case have large temperature anisotropy $T_\perp/T_\parallel = 4$, the L-mode EMIC instability takes place. The EMIC waves are generated through the linear growth. When the naturally generated EMIC waves grow to enough amplitude for the threshold that is predicted by (5.3) [*Omura et al.*, 2010], the nonlinear wave growth starts and the wave frequency becomes larger. The duration of the emission is much larger than those in Figures 5.6, 5.13, and 5.14, due to the difference of the cyclotron frequency.

Figure 5.19 shows the spatial and temporal evolution of the wave amplitudes of the forward and backward propagating waves. Because the resonance velocity of the energetic
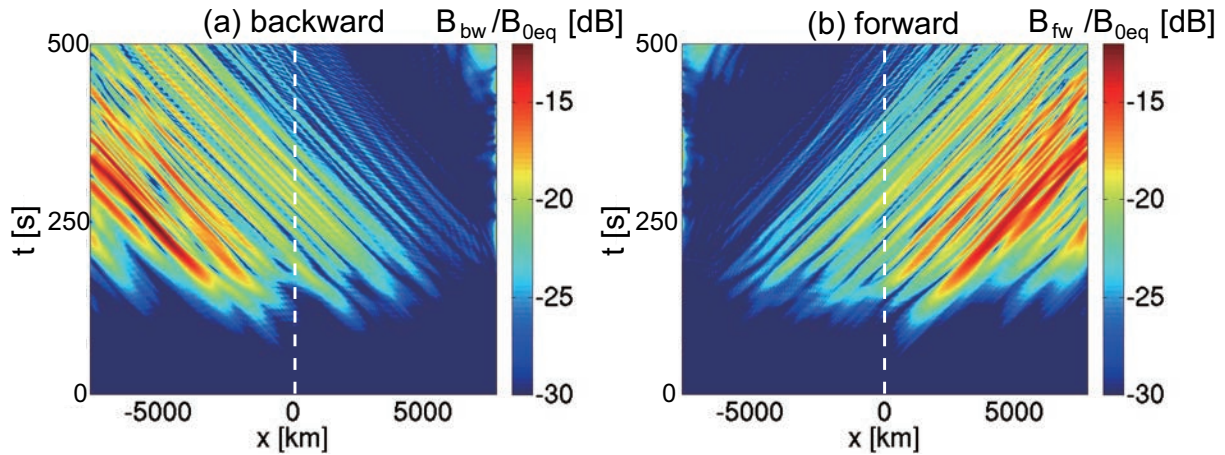
Figure 5.19: Spatial and temporal evolution of the wave amplitudes of the backward and forward propagating EMIC waves. The white dashed lines show the equator.

protons becomes the smallest at the equator, at first, the EMIC instability takes place around the equatorial region. The energetic particles which interact with the EMIC waves are phase organized and released around the equatorial region. Thus, because of the same mechanism as the EMIC triggered emissions as we discussed in section 5.2.2, the region of the wave emission moves backward of the wave propagation.

## 5.7   Summary

The nonlinear wave particle interactions between ULF waves and the energetic protons play an important role for the energy transportations in the Earth's inner magnetosphere. Especially, the rising tone emissions of the EMIC waves can effectively scatter the energetic protons around the equatorial regions. In this chapter, we performed hybrid simulations with a dipole cylindrical magnetic geometry to analyze the nonlinear characteristics of the EMIC emissions in the Earth's inner magnetosphere. This is the first study that the EMIC triggered emissions are successfully reproduced in realistic parameters. We conclude this chapter with the following six points.

1. We have developed a 1D hybrid code with a cylindrical magnetic field model to analyze the nonlinear wave growth of EMIC triggered emissions in dipole geometry, reproducing the rising-tone emissions from injected EMIC triggering waves around the equatorial region with realistic parameters. The duration and the frequency sweep rate of the triggered emissions show a good agreement with observations and nonlinear wave growth theory.

2. Parametric analyses indicate the existence of the critical range of the initial triggering wave amplitude to generate the EMIC triggered emissions. Although it is not predicted in the nonlinear wave growth theory for triggered emissions [*Omura et al.*, 2010], the triggering waves with too large wave amplitude cannot drive the triggered emissions. In the hybrid simulations, even though the amplitude of the triggering waves does not reach at the theoretical threshold given by (5.3), the triggering waves cause the linear growth and finally they obtain the amplitude enough to start the nonlinear wave growth.

3. The proton velocity distribution is strongly modulated by formation of large proton holes due to the triggered emissions. The rising tone emissions drive the proton holes to a lower parallel velocity because of the decreasing resonance velocities.

4. A substantial amount of energetic protons as large as 6.5% of the trapped protons are scattered into the loss cone in 45 s during which the triggered emissions are generated inside the plasmapause. These particles move away from the equator along the ambient magnetic field, and precipitate into the atmosphere, resulting in the proton aurora in the polar regions.

5. As predictions for the future spacecraft observations, we performed the simulations for the EMIC triggered emission in the $He^+$ branch. The EMIC triggered emission in the $He^+$ branch can scatter the energetic protons which have larger energy range than those scattered by the triggered emission in the $H^+$ branch.

6. The existence of the natural EMIC rising emission, which are also predicted by the hybrid simulation, indicates that the rising tone emission of the EMIC waves are easily caused by only the existence of the inward transportation of the energetic protons resulting in the anisotropic distributions.

For the further investigations of the EMIC triggered emissions, we mention the following three topics.

1. *Pickett et al.* [2010] reported that more than two triggered emissions took place in a few minutes. As demonstrated in the present simulation, however, the free energy of energetic protons is completely consumed by a single emission process of an EMIC triggered emission. We only introduce the energetic protons initially and thus we obtain only one pair of triggered emissions in the simulation. The observed multiple triggered emissions require continuous injection of fresh energetic protons. Continuous generation of the triggering EMIC waves, which can be excited by the cyclotron instability driven by the temperature anisotropy of protons, is also needed.

2. For the development of more precise nonlinear wave growth theory, the model of the evolution of the depth of the proton holes $Q$ is required. In the present theory, the depth is treated as a constant value [*Omura et al.,* 2010]. With this modeling, the saturation of the triggered waves can be included. The motion of the wave emission region should also be included in the theory. These are left as a future study.

3. The spacecraft observations with higher frequency resolutions in the Earth's inner magnetospere, more EMIC triggered emissions in the $H^+$ or lower branches will be found. Through the statistical analyses, we can find the contribution of the EMIC triggered emissions on the proton aurora in different energy ranges. It is also important for justifying the nonlinear growth theory to find the proton holes with high resolution particle observations.

# Chapter 6

# EMIC wave in the Helium Branch induced by EMIC Triggered Emission

## 6.1 Introduction

In Chapter 5, the EMIC triggered emissions in the Earth's inner magnetosphere have been studied by the hybrid simulations. We have introduced the investigations via Cluster observations [*Pickett et al.*, 2010; *Omura et al.,* 2010], theory [*Omura et al.,* 2010], and simulation [*Shoji and Omura,* 2011]. The observations [*Pickett et al.,* 2010] show that emissions have left-hand-polarized rising tone spectra in the ULF frequency range. They are triggered by Pc1 (EMIC) pulsations [e.g. *Troitskaya*, 1961; *Tepley*, 1961; *Roux et al.*, 1982; *Anderson et al.*, 1992a, 1992b; *Engebretson et al.*, 2007] around the equatorial region. The nonlinear growth theory derived by *Omura et al.* [2010] shows a good agreement with the observations in the frequency sweep rate of the rising tones. Moreover, the EMIC waves which propagate at a frequency below the $H^+$ cyclotron frequency play an important role for the cyclotron resonance interaction with the relativistic electrons of the radiation belts. *Meredith et al.* [2003] have performed statistical analyses on these interactions. The resonant quasi-linear scattering of energetic electrons by EMIC waves in the $H^+$ and $He^+$ branches have been theoretically analyzed by *Summers and Thorne* [2003] and *Summers et al.* [2007].

A hybrid simulation [*Shoji and Omura,* 2011] has successfully reproduced the EMIC triggered emissions in a cylindrical magnetic flux model assumed as the equatorial region of the Earth's inner magnetosphere. The duration, frequency sweep rate, and saturation level of the triggered emissions show a good agreement with the observations. In the simulation, the velocity distribution of the energetic protons is strongly modulated by formation of large proton holes due to the triggered emissions. Because of the inward

motion of the proton holes due to the rising frequency of the triggered emissions, the energetic protons are scattered over a wide range of velocities parallel to the background magnetic field.

In some cases of the observations and the simulations, we can find EMIC waves below the $He^+$ cyclotron frequency after generation of the EMIC triggered emissions in the $H^+$ branch as shown in Figure 5.13. We also find EMIC waves below the $O^+$ cyclotron frequency after the triggered emissions in $He^+$ branch. We present a Cluster observation of the multiple triggered emissions and the EMIC waves in the $He^+$ branch in Section 6.2. In Section 6.3, we reproduce the multiple EMIC triggered emissions by a hybrid code simulation to clarify how the associated EMIC waves in the $He^+$ branch are excited by the triggered emissions. Section 6.4 gives a summary and discussion.

## 6.2   Cluster Observation Results

### 6.2.1   Dynamic spectra of the helium branch wave

The full description of the wave properties of the observed triggered emissions is found in *Pickett et al.* [2010]. In Figure 6.1, we focus on a shorter time interval when the spacecraft is in the Northern Hemisphere. Flux Gate Magnetometer data are used in order to have a frequency range starting from DC, which includes a part of the spectrum below 0.8 Hz that was not displayed in Figure 2 of *Pickett et al.* [2010]. In the spectrogram (top panel of Figure 6.1), triggered emissions are detected between 08:05 and 08:15 UT (c.f. *Pickett et al.* [2010] for general wave properties). The first riser (at 08:12) is the most intense. It is followed by several other less powerful risers. The two risers detected immediately after the first one have a shorter frequency extent (up to 2.4 Hz). The last one ends at 08:16, and despite its weak power, the emission rises to 3 Hz. Triggered emissions display a high level of coherence indicative of a high degree of polarization [*Santolik et al.*, 2003]. This observed coherence is much larger than that of the EMIC waves observed in the same time frame. The second part of the event, starting from 08:15, is dominated by strong monochromatic emissions (at 0.7 Hz) just below the local helium gyrofrequency (black solid line). Weaker monochromatic emissions are also detected above the helium gyrofrequency around 1.4 and 2.2 Hz.

### 6.2.2   Time evolution of the observed distribution function

The time evolution of the velocity distribution function of the energetic protons at 08:12:04, 08:14:48, 08:15:04, and 08:17:08 UT is shown in Figures 6.2a, 6.2b, 6.2c, and 6.2d, respectively. Comparing Figures 6.2a with 6.2b, we find the pitch angle scattering of particles in
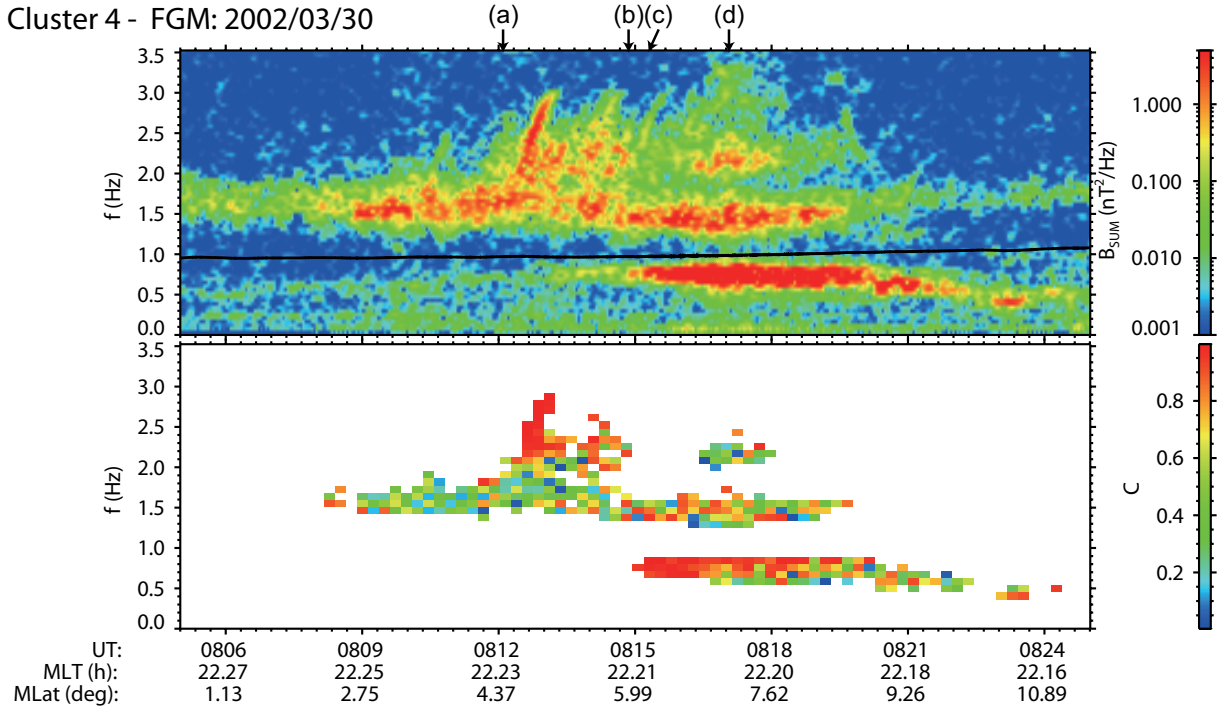
Figure 6.1: Dynamic power spectrum of the magnetic field (top panel) from DC to 3.5 Hz between 0805 and 0825 on March 30th, 2002 (data from the Flux Gate Magnetometer (FGM) onboard Cluster 4). The coherence level (bottom panel) is estimated for the most energetic part of the spectrogram. Spacecraft Magnetic Local Time and Magnetic Latitude are given for each time mark. The arrows indicate the times corresponding to Figures 6.2a, 6.2b, 6.2c, and 6.2d.

a wide velocity range due to the drastic change of the resonance velocity of the triggered emission with rising frequencies (decreasing resonance velocity from the white dashed lines in Figure 6.2a to the white dash-dotted lines in Figure 6.2b). This wide pitch angle scattering shows good agreement with the simulation result in *Shoji and Omura* [2011]. The distributions shown in Figure 6.2c and 6.2d are characteristic of the period, following the triggered emissions, when monochromatic emissions are seen in Figure 6.1a for the $H^+$ ($f \sim 1.4$ Hz) and $He^+$ ($f \sim 0.7$ Hz) branches. The resonance velocities of the $H^+$ branch waves are shown as black dashed lines in Figure 6.2c. The EMIC waves in the $He^+$ branch are observed around the time in Figure 6.2d. The resonance velocities of the $He^+$ branch wave are shown as black dash-dotted lines in Figure 6.2d. The energetic protons around these resonance velocities are scattered along the diffusion curves of these waves [*Gendrin* 1968]. The markers in magenta indicate velocities at which pronounced variations of the distribution are found.
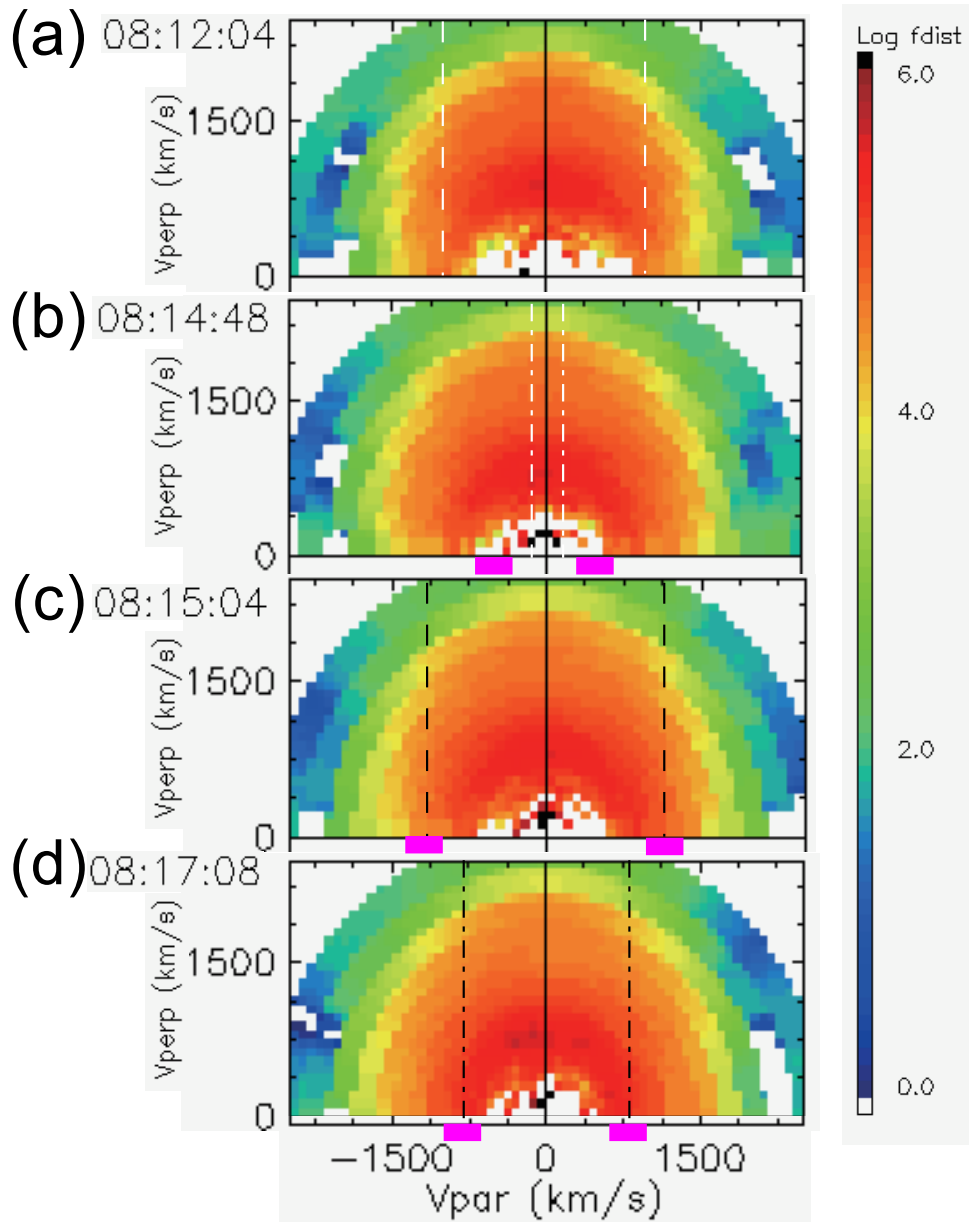
Figure 6.2: Velocity distribution functions of the high  energy component (40 eV to 40 keV) of protons in the $V_\parallel - V_\perp$ plane observed by the CIS-CODIF instrument of Cluster 4 [*Reme et al.*, 2001] at (a) 08:12:04, (b) 08:14:48, (c) 08:15:04, and (d) 08:17:08 UT on 30 March 2002. The white regions indicate the outside of the detectable region (90 km/s to 2770 km/s) or the region where no particles have been detected. The white dashed lines in panel (a), the white dash-dotted lines in panel (b), the black dashed lines in panel (c), and the black dash-dotted lines in panel (d) show the resonance velocities of the triggering waves, the triggered waves reaching the maximum frequency ($\sim$3 Hz), the H$^+$ branch waves with slightly lower frequency ($\sim$ 1.4 Hz), and the He$^+$ branch waves, respectively. The magenta markers show the regions where the distribution functions are changed.

# 6.3 Generation Mechanism of EMIC waves in Helium branch: Simulation Analyses

## 6.3.1 Simulation parameters

As we discussed in Chapter 2, we have developed a 1D hybrid code with a cylindrical magnetic flux model [*Shoji et al.,* 2011; *Shoji and Omura,* 2011]. We use the same model configuration as Chapter 5. According to the observational results [*Omura et al.,* 2010], the cyclotron and the plasma frequencies of protons are assumed as 3.7 Hz and 353.4 Hz, respectively, at the magnetic equator. Thus the amplitude of the ambient magnetic field is $B_{0eq}$ =243 nT, and the Alfven velocity is 443 km/s at the equator. The number of grids of the physical region taken along the $x$ axis is $N_x = 4,096$ with the grid spacing $\Delta x = 0.1 V_A / \Omega_H (= 1.9$ km), and the time step is $\Delta t = 0.004 / \Omega_H (= 1.72 \times 10^{-4}$ s), where $V_A$ and $\Omega_H$ are the Alfven velocity and the cyclotron frequency of the cold protons at the equator, respectively. The frequency and the wavenumber of the triggering waves, which are excited by the left handed polarized external current source, are taken from the observations as $(\omega_w, k_w) = (0.409 \Omega_H, 0.27 \Omega_H / V_A)$, which correspond to a frequency 1.5 Hz and a wavelength $(2\pi / k_w)$ 450 km. The wave amplitude of the triggering wave is $B_w = 0.25$ nT.

We assume four ion species. Cold plasma components of $H^+$, $He^+$ and $O^+$ are assumed, and the thermal distributions of them are neglected. The thermal velocities of energetic protons in the parallel and perpendicular directions are $0.002c$ and $0.00267c$, respectively, where $c$ is the speed of light. The density of these ions are $0.729n_e$ $0.095n_e$, $0.095n_e$, and $0.081n_e$, respectively, where $n_e$ (=178 /cc) is the density of the electron fluid. The charge-to-mass ratios of the protons, helium, oxygen are $1.0e/m_H$, $0.25e/m_H$, and $0.0625e/m_H$, respectively, where $e$ and $m_H$ are the elementary charge and mass of the proton, respectively. The average numbers of superparticles of cold $H^+$, $He^+$, $O^+$, and energetic $H^+$ in a cell are 256, 256, 256, and 16384, respectively. Their densities are assumed so that the wave dispersion relation gives the observed cut-off frequencies. Energetic $H^+$ ions with temperature anisotropy are introduced as resonant particles with EMIC waves, forming a loss cone distribution function [*Shoji and Omura,* 2011]. The quiet start [*Birdsall and Langdon,* 1985] is used to reduce the initial thermal fluctuations. The energetic protons are initialized to form a spatial distribution that is stable in time with adiabatic motion in the parabolic magnetic field.

## 6.3.2   Simulation results

We separate the wave magnetic fields into forward and backward propagating wave components using the same method as used by *Shoji and Omura* [2011]. To obtain the dynamic spectra around the equatorial region, we apply a Fourier transform in a limited time window and slide it from the initial time to the end of the simulation period. The size of the window is chosen as $t \sim 11.2$ s for a sufficient resolution in the frequency domain. Figures 6.3a and 6.3b show the dynamic spectra of the magnetic field of the forward and backward propagating waves around the equatorial region, respectively. Because we introduced a higher density of energetic protons than that assumed in *Shoji and Omura* [2011], there still remains enough free energy to generate another triggered emission in the simulation space. We obtain multiple rising tone EMIC triggered emissions in the $H^+$ branch both in the forward and backward propagating waves as shown in Figure 6.3. A substantial part of the distribution function of the protons is scattered by the first triggered emission [*Shoji and Omura*, 2011], and thus the second triggered wave saturates faster than the first one. The multiple chorus emissions are discussed by *Katoh and Omura* [2011], and the same dependency of the multiple emissions on the energetic particle density is also found in the case of EMIC triggered emissions. From $t \sim 30$ s, after the second triggered emission starts, another branch of EMIC waves below the $He^+$ cyclotron frequency (0.925 Hz, shown by the white dashed lines) is generated both in forward and backward propagating wave spectra. These spectra show a good agreement with the observation shown in Figure 6.1.

Figures 6.4a to 6.4f show the velocity distribution functions of the energetic protons around the equatorial region at different times. We focus on the negative velocity range of the distribution function interacting with the forward propagating waves. In Figure 6.4g, we calculate a value $\Delta E$ which is defined as (energy density in the velocity phase space) $\times$ (density gradient along the diffusion curve of the EMIC wave in the $He^+$ branch). When $\Delta E$ is positive, the energetic protons around the resonance velocity are scattered losing their energy, and thus the $He^+$ branch EMIC waves can be generated. We also plot the resonance velocities $V_{R0}$ of the triggering wave, $V_{He}$ of EMIC waves in the $He^+$ branch, and $V_R$ of the triggered waves in Figures 6.4a to 6.4f. Here, we note that these velocities satisfy

$$|V_{Rf}| < |V_{He}| < |V_{R0}| \quad , \tag{6.1}$$

where $V_{Rf}$ indicates the resonance velocity of the triggered waves at the highest frequency. Through the nonlinear wave growth, a proton hole is generated around the resonance velocity $V_R$ [*Shoji and Omura*, 2011] and it moves inward to the core part of the distribution
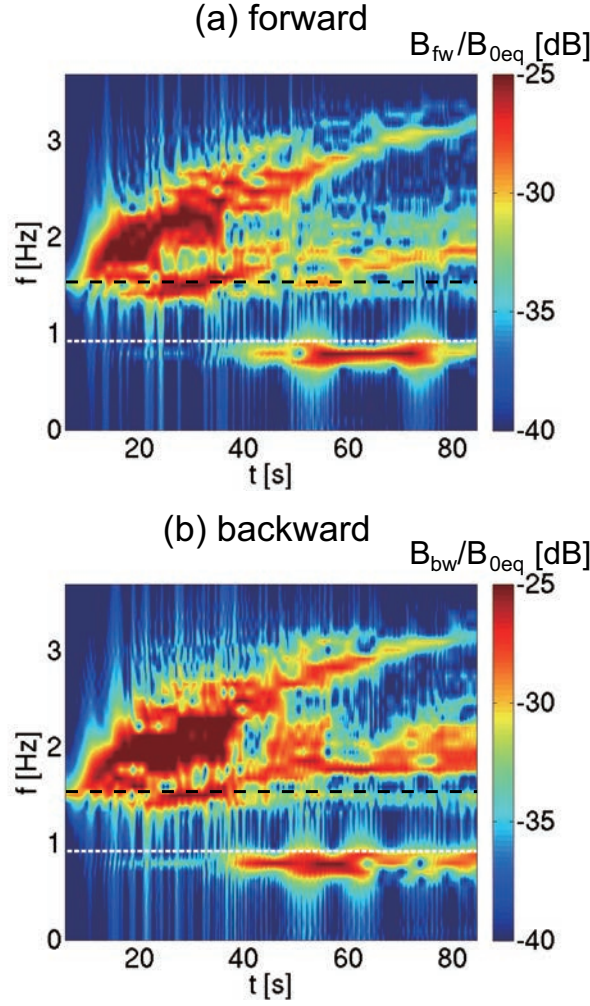
Figure 6.3: Dynamic spectra of the magnetic fields of (a) forward propagating waves with triggering wave and (b) backward propagating waves with triggering wave. The black and white dashed lines show the frequency of the triggering waves and the cyclotron frequency of He$^+$, respectively.

functions. The resonance velocity of triggered waves $V_R$ changes from $V_{R0}$ and approaches to $V_{Rf}$ due to the nonlinear process.

Figure 6.4a shows the initial distribution function. From the initial time to around $t \simeq 16$ s, because the resonance velocity of the first triggered wave $|V_R|$ is greater than $|V_{He}|$, the density gradient along the diffusion curve of the He$^+$ branch wave is enhanced at a higher pitch angle of the distribution function and thus the value of $\Delta E$ takes a positive value. As the frequency of the triggered emission increases, $|V_R|$ becomes smaller and moves across $V_{He}$ as shown in Figure 6.4b. As shown in Figure 6.4b, a proton hole is formed around the resonance velocity of the first triggered emission (white solid line), which is near $V_{He}$ (black dashed line), the density increases in the lower pitch angles,

and thus the value of $\Delta E$ starts to decrease. After that, as the depth of the proton hole becomes larger, there appears a negative $\Delta E$ region as shown in Figure 6.4c. Through the inward motion of the proton holes, the core part of the distribution function is scattered [*Shoji and Omura*, 2011]. Because a substantial number of protons are scattered in the region $|v| < |V_{He}|$, the density gradients are enhanced around $V_{He}$ along the diffusion curve of the He$^+$ branch wave as shown in Figure 6.4c. At $t = 20.1$ s in Figure 6.4g, we find a positive value region of $\Delta E$. However, there still remains a negative region and thus the He$^+$ branch waves are not generated. The same process also takes place with the second triggered emission.

The resonance velocity of the second emission, shown by a purple line, also moves across $V_{He}$ as shown in Figure 6.4d. As a result of this scattering due to the multiple triggered emissions, a broad positive $\Delta E$ appears around $t = 30.1$ s in Figure 6.4g. The corresponding unstable distribution function is shown in Figure 6.4e. The EMIC waves in the He$^+$ branch start to be generated at this time as shown in Figure 6.3. Energetic protons near the resonance velocity of the wave in the He$^+$ branch lose their energy. Therefore, the EMIC waves in the He$^+$ branch are generated through the cyclotron resonance with the energetic protons. After the generation of the He$^+$ branch waves, due to the scattering of the distribution functions by the He$^+$ branch EMIC waves, the velocity distribution becomes flat along the diffusion curve of the wave as shown in Figure 6.4f.

## 6.4   Summary

We performed a hybrid simulation for multiple EMIC triggered emissions, and found that EMIC waves in the He$^+$ branch are induced by the triggered emissions. With a sufficient flux of energetic protons in the simulation space, the multiple EMIC triggered emissions are generated through nonlinear wave growth from the triggering waves [*Omura et al.*, 2010; *Shoji and Omura*, 2011]. With the rising tone EMIC triggered emissions, the resonance velocities of the triggered emissions move across that of the He$^+$ branch waves. The distribution function is modulated so as to enhance the density gradient along the diffusion curve of the He$^+$ branch waves. Thus, the He$^+$ branch EMIC waves are generated after the multiple EMIC triggered emissions in the H$^+$ branch. EMIC waves with slightly lower frequency in the H$^+$ branch are also found in the simulation result. The H$^+$ branch waves have a resonance velocity greater than that of the triggering wave. Thus, the H$^+$ branch waves are generated through cyclotron resonance with the energetic protons scattered from the phase space volume interacting with the triggered emissions in the distribution function. These EMIC waves in the H$^+$ and He$^+$ branches are generated
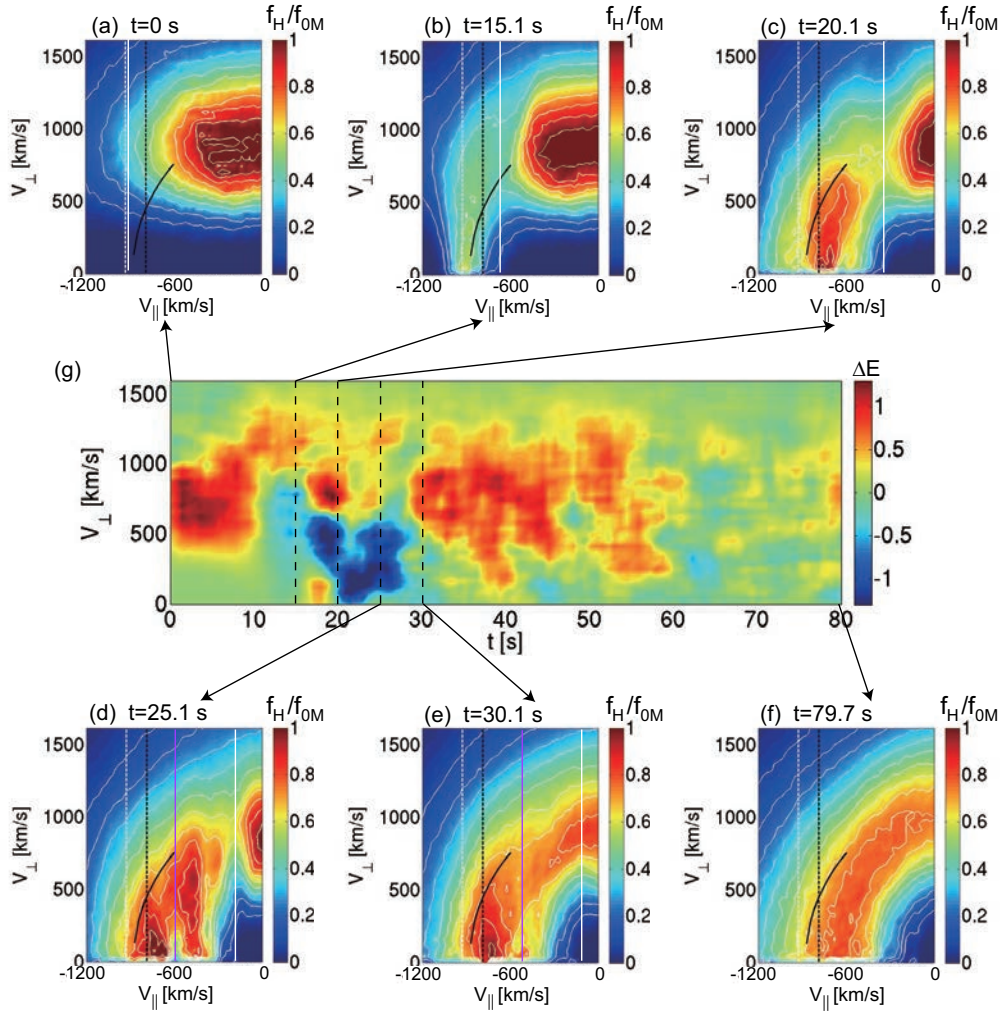
Figure 6.4: Velocity distribution functions of energetic protons at (a) $t = 0$ s, (b) $t = 15.1$ s, (c) $t = 20.1$ s, (d) $t = 25.1$ s, (e) $t = 30.1$ s, and (f) $t = 79.7$ s normalized by the maximum value of the initial velocity distribution function $f_{0M}$. The black dashed line, white dashed line, white solid line, and purple solid line show the resonance velocities of EMIC wave in the He$^+$ branch, the triggering wave, the first EMIC triggered wave, and the second triggered wave, respectively. The black solid curves show the diffusion curves [*Gendrin* 1968] of the EMIC waves in the He$^+$ branch. (g) The kinetic energy density gradient in phase space $\Delta E$ along the diffusion curve at the resonance velocity $V_{\text{He}}$ in arbitrary units.

through the linear growth processes independently. The generation of these waves shows a good agreement with the observations shown in Figure 6.1.

Based on the simulation results shown in Figure 6.4, we can interpret the time evolution of the distribution functions observed by the Cluster spacecraft shown in Figure 6.2. Comparing Figures 6.2b with 6.2a, we find the pitch angle scattering of the core part of the distribution function. The particles in the lower parallel velocities are scattered through the inward motion of the proton holes due to the rising frequencies. Some of the energetic protons are scattered to a velocity greater than the resonance velocity of the triggering wave, and the EMIC waves in the $H^+$ branch are generated at a slightly lower frequency $\sim$ 1.4 Hz. The energetic protons are precipitated into the loss cone around the resonance velocities of the $H^+$ branch waves as we can see in Figure 6.2c. A density gradient also appears along the diffusion curve of the $He^+$ branch waves. The $He^+$ branch waves are generated and the phase space in the lower pitch angle and lower parallel velocity is filled by the scattered protons as shown in Figure 6.2d.

In the observations shown in Figure 6.1, we find more EMIC triggered emissions than in the simulation. These multiple triggered emissions should be caused by injections of energetic protons into the inner magnetosphere. As a result, the amplitude of the $He^+$ branch waves becomes larger. In the observation shown in Figure 6.1, we find the lower $H^+$ branch wave is 1.4 Hz, while $He^+$ branch wave is 0.8 Hz. The three wave coupling process induces a wave at 2.2 Hz (=1.4 Hz + 0.8 Hz), which is not a simple harmonic of the $He^+$ branch wave. A hybrid simulation with continuous injection of fresh energetic protons is left as a future study.

As shown in Figure 5.14, we can also find the EMIC waves in the $O^+$ branch after the multiple EMIC triggered emissions in the $He^+$ branch. This is also because of the density gradient which appears along the diffusion curve of the $O^+$ branch wave through the inward motion of the resonance velocity of the triggered emissions. The result indicates that the multiple triggered emissions in any branch can generate the EMIC wave in the lower branch. More precise and generalized analyses for these EMIC wave emissions in the lower branch are also left as a future study.

# Chapter 7

# Concluding Remarks

## 7.1  Summary and Conclusion

To understand the electromagnetic environment surrounding the Earth, we have investigated microscopic nonlinear wave particle interactions. In this thesis, we have focused on the mirror and EMIC instabilities excited by the ion temperature anisotropies in the perpendicular direction to the ambient magnetic field in the different regions of the magnetosphere. Especially, we have raised the following four questions in space plasmas. (1) How does the mirror instability dominate over the L-mode EMIC instability in the magnetosheath? (2) How are the magnetic peaks and dips generated through the nonlinear evolutions of the mirror mode structures in the magnetosheath? (3) How are the nonlinear wave-particle interactions caused by the EMIC triggered emissions in the inner magnetsphere? and (4) What is the generation mechanism of the EMIC waves below the helium cyclotron frequency after the multiple EMIC triggered emissions? These topics have been discussed in Chapters 3, 4, 5, and 6, respectively.

In Chapter 1, the overview of the macroscopic electromagnetic environment surrounding the Earth has been explained. We have also discussed the ion plasma instabilities driven by the temperature anisotropy. Especially, the linear theoretical analyses of the L-mode EMIC and mirror instabilities have been performed.

In Chapter 2, we have explained the numerical techniques of the multi-dimensional hybrid simulations. We have shown the basic explanation of numerical techniques. The multi-dimensional hybrid simulation code with the open boundary employing the damping region have been developed. We have also described the simulations with the cylindrical geometry of the parabolic background magnetic field to model the Earth's inner magnetosphere.

In Chapter 3, we have investigated the competing process between the L-mode EMIC and mirror instabilities in the magnetosheath. We used the multi-dimensional periodic

models. Comparing between the results of the 2D and 3D models, we have shown that there are four reasons for dominance of the mirror instability in the magnetosheaths.

First (Section 3.3.2), we have shown that the mirror mode waves gain more energy than the L-mode EMIC instability because the degree of freedom in the perpendicular direction increases. The mirror instability affects the saturation levels of the L-mode EMIC waves and the temperature anisotropy of ions. In the 3D model, because the mirror mode waves consume more free energy, the EMIC waves cannot gain enough energy to grow. The temperature anisotropy is relaxed faster in the 3D model than those in other models. Second (Section 3.3.3), the theoretical condition of the initial thermal fluctuations for the dominance of the mirror instability is derived. The realistic conditions for the thermal fluctuations result in the dominance of the mirror mode wave. Third (Section 3.3.4), the effect of the alpha particles, which are included in the solar wind, has been shown. The alpha particles are heated effectively by the EMIC waves [*Omura et al.,* 1988], resulting in the earlier stop of the EMIC wave growth.

Fourth (Sections 3.4.1 and 3.4.2), we have shown the different nonlinear evolutions of the L-mode and mirror instabilities. The L-mode EMIC waves cause the heating of protons. Because of the existence of the forward and backward propagating waves, the nonlinear electrostatic potentials are generated in the parallel direction. Therefore, the L-mode EMIC waves lose their energy and disappear from the simulation space. The mirror mode structures, on the other hand, coalesce and become larger structures. Because the time scale of the coalescence is much longer than that of the inverse cascading, protons are less affected by the nonlinear evolution of the mirror mode waves. Therefore, only the mirror mode waves remain and are well observed in the magnetosheath.

In Chapter 4, the nonlinear evolution of the mirror mode structures, of which the detailed analyses have been left in Chapter 3, have been investigated. We performed the multi-dimensional hybrid simulations with open boundary models. We showed the generation conditions and processes magnetic peaks and dips through the coalescence of the mirror mode structures. In Section 4.2, we obtained the fine structures of the mirror mode structures in the 2D and 3D open systems, since only the mirror mode structures do not move. By the parametric analyses on the initial ion beta in the higher spatial resolutions (Section 4.3), we found that the magnetic peaks appear only in the 2D models with low ion beta cases. The magnetic peaks, on the other hand, are formed in 2D high ion beta models and all 3D models. The mirror instability grows in the higher wavenumbers (smaller wavelength), as the initial ion beta is assumed lower. Most protons have small parallel velocities in the lower ion beta conditions. They are trapped by the magnetic structures. Since the magnetic structures are uniform in the $z$ direction in the 2D models,

they are easily trapped in the area with decreased magnetic field compared with those in the 3D models. Thus, the magnetic dips appear in the 2D models. In the higher ion beta cases, on the other hand, because of the stronger pitch angle scattering into the parallel direction and the large initial parallel velocities, the number of the particles which can be trapped by the magnetic structures become smaller.

The coalescence of the magnetic dips takes place in both low and high beta cases. The coalescence is explained by the attraction of the diamagnetic current loops inside the magnetic dips (bubbles) as shown in Figure 4.10. Since the coalescence rate becomes larger as the mobility of the particles trapped inside the dips becomes larger, the current loops merge effectively in the high beta cases.

In Chapter 5, we performed hybrid simulations with a dipole cylindrical magnetic geometry to analyze the nonlinear characteristics of the EMIC emissions in the Earth's inner magnetosphere. In Section 5.2, we have successfully reproduced the EMIC triggered emissions in realistic parameters from injected EMIC triggering waves around the equatorial region with realistic parameters. The duration and the frequency sweep rate of the triggered emissions show a good agreement with observations [*Pickett et al.*, 2010] and nonlinear wave growth theory [*Omura et al.*, 2010]. Parametric analyses for the triggered emissions in Section 5.4 predicted that the critical range of the initial triggering wave amplitude for generation of the EMIC triggered emissions exist. Although it is not shown in the nonlinear wave growth theory for triggered emissions, the triggering waves with too large wave amplitude cannot drive the triggered emissions.

As we showed in Section 5.3, the velocity distribution of the protons is strongly modulated by formation of large proton holes due to the triggered emissions. The rising tone emissions drive the proton holes to a lower parallel velocity because of the decreasing resonance velocities. A substantial amount of energetic protons as large as 6.5% of the trapped protons are scattered into the loss cone in 45 s during which the triggered emissions are generated inside the plasmapause. These particles move away from the equator along the ambient magnetic field, and precipitate into the atmosphere, resulting in the proton aurora in the polar regions.

We also performed the simulations for the EMIC triggered emission in the $He^+$ branch and the EMIC chorus emission as predictions for the future spacecraft observations. We have generated the EMIC triggered emissions and natural EMIC triggered emissions in the simulation model. The $He^+$ branch triggered emission scatters the energetic protons which have larger energy range than those scattered by the $H^+$ branch triggered emission. The existence of the natural EMIC triggered emission indicates that the rising emissions of the EMIC waves easily take place only with the anisotropic velocity distribution functions

of the energetic protons without the external triggering waves.

In Chapter 6, we performed a hybrid simulation for multiple EMIC triggered emissions, and found that EMIC waves in the He$^+$ branch are induced by the triggered emissions. The multiple EMIC triggered emissions are generated through nonlinear wave growth from the triggering waves [*Omura et al.*, 2010; *Shoji and Omura*, 2011] because of existence of a sufficient flux of energetic protons in the simulation space. We found the EMIC wave emissions in He$^+$ branch both in the observations in Section 6.2 and the simulations in Section 6.3. With the rising tone EMIC triggered emissions, the resonance velocities of the triggered emissions move across that of the He$^+$ branch waves modulating the velocity distribution functions. Consequently, the density gradient is enhanced along the diffusion curve of the He$^+$ branch waves, resulting in the generation of the He$^+$ branch EMIC waves after the multiple EMIC triggered emissions in the H$^+$ branch. EMIC waves with slightly lower frequency in the H$^+$ branch are also found in the simulation result. The H$^+$ branch waves have a resonance velocity greater than that of the triggering wave. Thus, the H$^+$ branch waves are generated through cyclotron resonance with the energetic protons scattered from the phase space volume interacting with the triggered emissions in the distribution function. These EMIC waves in the H$^+$ and He$^+$ branches are generated through the linear growth processes independently. The generation of these waves shows a good agreement with the observations shown in Figure 6.1. The scattering by these EMIC waves are also found in the observations in Figure 6.2.

We also found the generation of the EMIC waves in the O$^+$ branch after the multiple EMIC triggered emissions in the He$^+$ branch as shown in Figure 5.14. This is also due to the density gradient which appears along the diffusion curve of the O$^+$ branch wave through the inward motion of the resonance velocity of the He$^+$ branch triggered emissions. As a general argument for the triggered emissions, the multiple triggered emissions in any branch generate the EMIC wave in the lower branch.

The present thesis contributes to understanding of the basic processes of the plasma instabilities driven by the ion temperature anisotropy around the Earth, via the large scale computer simulations with the hybrid models. The change of the space electromagnetic and plasma environment due to the nonlinear wave particle interactions has been evaluated. Moreover, according to these results, we can suggest the observation targets for the future spacecraft missions.

## 7.2 Suggestions for Future Studies

For the future investigations on the mirror and the L-mode EMIC instabilities, the further development of the 3D models are needed. Especially, the nonuniform models of the magnetosheath regions including the bowshock are essential for the precise analyses on the competing process and the nonlinear evolutions of these instabilities. The effect of the instabilities on the bowshock structures and the fluctuation in the magnetosheath can be also analyzed with these models. Moreover, through the interactions, ions are accelerated or heated. The wave-particle interactions, which generate localized large amplitude magnetic structures, are possible to be related with the transportation of the high energy solar wind plasmas into the Earth's magnetosphere. Such interactions between the ion scale electromagnetic phenomena and the larger electromagnetic structures or environment around the Earth are left as unsolved questions. Moreover, the impacts of the human activities in space are important in the interactions between the different scale electromagnetic structures. In particular, artificial ion beams formed by the ion engines excite the ion beam instabilities [c.f. *Gary et al.*, 1981]. The instabilities cause the diffusion of ions [*Winske and Leroy*, 1984] around the ion engines, and then, will affect the electromagnetic environment around the ion engines. As a result, the plasma configuration and the electromagnetic environment in some regions surrounding the Earth can be affected. Therefore, we need to study not only independent the plasma instability but also the interactions of these ion scale instabilities with much larger scale electromagnetic structures such as bowshock, and magnetopause.

For the statistical analyses by the spacecraft observations on the EMIC triggered emissions, we need more observation reports. With higher frequency resolutions, more observations for the EMIC triggered emissions should be appeared. New spacecraft missions such as ERG (Energization and Radiation in Geospace) mission by Japan are going to focus on the particle dynamics in the radiation belt. The contribution of the EMIC triggered emissions on the geospace ion plasmas can be estimated though the data analyses of the new spacecrafts. Moreover, to control the precipitation of the energetic particles in the radiation belt, artificial whistler-mode wave emissions from antennas of spacecrafts are investigated [*Inan et al.*, 2003]. The EMIC waves also affect the energetic ions and relativistic electrons in the radiation belt. The EMIC triggered emissions scatter the pitch angle of the protons, significantly. The method for artificial EMIC triggered emissions and the particle scattering should be studied. The most effective parameters of the EMIC wave emissions can be indicated by the large scale computer simulations.

# Bibliography

[1] Anderson, B. J., R. E. Erlandson, and L. J. Zanetti (1992a), A statistical study of Pc 1-2 magnetic pulsations in the equatorial magnetosphere: 1. Equatorial occurrence distributions, *J. Geophys. Res., 97*, 3075.

[2] Anderson, B. J., R. E. Erlandson, and L. J. Zanetti (1992b), A statistical study of Pc 1-2 magnetic pulsations in the equatorial magnetosphere: 2. Wave properties, *J. Geophys. Res., 97*, 3089.

[3] Arnoldy, R. L., et al. (2005), Pc 1 waves and associated unstable distributions of magnetospheric protons observed during a solar wind pressure pulse, *J. Geophys. Res., 110*, A07229.

[4] Balikhin, M. A., O. A. Pokhotelov, S. N. Walker, R. J. Boynton, and N. Beloff (2010), Mirror mode peaks: THEMIS observations versus theories, *Geophys. Res. Lett., 37*, L05104.

[5] Balikhin, M. A., R. Z. Sagdeev, S. N. Walker, O. A. Pokhotelov, D. G. Sibeck, N. Beloff, and G. Dudnikova (2009), THEMIS observations of mirror structures: Magnetic holes and instability threshold, *Geophys. Res. Lett., 36*, L03105.

[6] Baumjohann, W., and R. A. Treumann (1997), Basic Space Plasma Physics, *Imperial College Press.*

[7] Bavassano, B., E. Pietropaolo, and R. Bruno (1998), Cross-helicity and residual energy in solar wind turbulence: Radial evolution and latitudinal dependence in the region from 1 to 5 AU, *J. Geophys. Res., 103(A4)*, 6521.

[8] Birdsall, C. K., and A. B. Langdon (1985), Plasma physics via computer simulation, *McGraw-Hill.*

[9] Brinca, A. L., and B. T. Tsurutani (1989), Influence of multiple ion species on low-frequency electromagnetic wave instabilities, *J. Geophys. Res., 94*, 13,565.

[10] Califano, F., P. Hellinger, T. Passot, P. L. Sulem, and P. Travnicek (2008), Nonlinear Mirror Mode Dynamics: Simulations and Modeling, *J. Geophys. Res., 113*, A08219.

[11] Chandrasekhar, S. A., A. N. Kaufman, and K. M. Watson (1958), The stability of the pinch, *Proc. R. Soc. London Ser. A, 245*, 435.

[12] Chappell, C., K. Harris, ang G. Sharp (1970), A study of the influence of magnetic activity on the location of the plasmapause as measured by OGO 5, *J. Geophys. Res., 72*, 50.

[13] Chodura, R. (1975), A hybrid fluid-particle model of ion heating in high-Mach-number shock waves, *Nucl. Fusion, 15*, 55.

[14] Dawson, J. M. (1983), Particle simulation of plasmas, *Rev. Modern Phys., 55*, 403.

[15] Eastman, T. E., and L. A. Frank (1984), The plasma sheet boundary layer, *J. Geophys. Res., 89*, 1553.

[16] Engebretson, M. J., et al. (2007), Cluster observations of Pc 1-2 waves and associated ion distributions during the October and November 2003 magnetic storms, *Planet. Space Sci., 55*, 829.

[17] Erdos, G., and A. Balogh (1996), Statistical properties of mirror mode structures observed by Ulysses in the magnetosheath of Jupiter, *J. Geophys. Res., 101*, 1.

[18] Erlandson, R. E., L. J. Zanetti, T. A. Potemra, L. P. Block, and G. Holmgren (1990), Viking magnetic and electric field observations of Pc 1 waves at high latitudes, *J. Geophys. Res., 95*, 5941.

[19] Erlandson, R. E., K. Mursula, and T. Bosinger (1996), Simultaneous ground-satellite observations of structured Pc 1 pulsations, *J. Geophys. Res., 101*, 27,149.

[20] Fukunishi, H., (1975) Dynamic Relationship Between Proton and Electron Auroral Substorms, *J. Geophys. Res., 80*, 553.

[21] Fuselier S. A., B. J. Anderson, S. P. Gary, and R. E. Denton (1994), Inverse correlations between the ion temperature anisotropy and plasma beta in the Earth's quasi-parallel magnetosheath, *J. Geophys. Res., 99*, 14,931.

[22] Gary, S. P., R. M. Skoug, J. T. Steinberg, and C. W. Smith (2001), Proton temperature anisotropy constraint in the solar wind: ACE observations, *Geophys. Res. Lett., 28(14)*, 2759.

[23] Gary, S. P., H. Li, S. O'Rourke, and D. Winske (1998), Proton resonant firehose instability: Temperature anisotropy and fluctuating field constaints *J. Geophys. Res., 103*, 14,567.

[24] Gary, S. P., M. E. McKean, D. Winske, B. J. Anderson, R. E. Denton, and S. A. Fuselief (1994a), The proton cyclotron instability and the anisotropy/$\beta$ inverse correlation, *J. Geophys. Res., 99*, 5903.

[25] Gary, S. P., P. D. Convery, R. E. Denton, S. A. Fuselief, and B. J. Anderson (1994b), Proton and helium cyclotron anisotropy instability thresholds in the magnetosheath, *J. Geophys. Res., 99*, 5915.

[26] Gary, S. P., S. A. Fuselier, and B.J. Anderson (1993), Ion anisotropy instabilities in the magnetosheath, *J. Geophys. Res., 98*, 1481.

[27] Gary, S. P. (1992), The mirror and ion cyclotron anisotropy instabilities, *J. Geophys. Res., 97*, 8519.

[28] Gary, S. P., J. T. Gosling, D. W. Forslund (1981), The electromagnetic ion beam instability upstream of the earth's bow shock, *J. Geophys. Res., 86*, 6691.

[29] Gendrin, R. (1968), Pitch angle diffusion of low energy protons due to gyroresonant interaction with hydromagnetic waves, *J. Atmos. Terr. Phys. 30*, 1313.

[30] Glassmeier, K. H, P. N. Mager, and D. Y. Klimushkin (2003), Concerning ULF pulsations in Mercury's magnetosphere, *Geophys. Res. Lett., 30*, 1928.

[31] Gold, T. (1959), Motions in the Magnetosphere of the Earth, *J. Geophys. Res., 64(9)*, 1219.

[32] Hamasaki, S., N. A. Krall, C. E. Wagner, and R. N. Byrne (1977), Effect of turbulence on theta pinch modeling by hybrid numerical models, *Phys. Fluids, 20*, 65.

[33] Hasegawa, A. (1975), Plasma instabilities and nonlinear effects, *Phys. and Chem. In Space 8*, Springer-Verlag, NY, 94.

[34] Hasegawa, A. (1969), Drift mirror instability in the magnetosphere, *Phys. Fluids, 12*, 2642.

[35] Hau, L. N., B. J. Wang, and W. L. Teh (2005), Slow mode waves and mirror instability in gyrotropic Hall magnetohydrodynamic model, *Phys. Plasmas, 12*, 122904.

[36] Hellinger, P., E. A. Kuznetsov, T. Passot, P. L. Sulem, and P. M. Travnicek (2009), Mirror instability: From quasi-linear diffusion to coherent structures, *Geophys. Res. Lett., 36*, L06103.

[37] Hellinger, P., P. Travnicek, J. C. Kasper, and A. J. Lazarus (2006a), Solar wind proton temperature anisotropy: Linear theory and WIND/SWE observations, *Geophys. Res. Lett., 33*, L09101.

[38] Hellinger, P., and P. Travnicek (2006b), Parallel and oblique proton fire hose instabilities in the presence of alpha/proton drift: Hybrid simulations, *J. Geophys. Res., 111*, A01107.

[39] Hellinger, P., and H. Matsumoto (2001), Nonlinear competition between the whistler and Alfven fire hoses, *J. Geophys. Res., 106*, 13,215.

[40] Hikishima, M., Y. Omura, and D. Summers (2010), Microburst precipitation of energetic electrons associated with chorus wave generation, *Geophys. Res. Lett., 37*, L07103.

[41] Hikishima, M., S. Yagitani, Y. Omura, and I. Nagano (2009a), Full particle simulation of whistler-mode rising chorus emissions in the magnetosphere, *J. Geophys. Res., 114*, A01203.

[42] Hikishima, M., S. Yagitani, Y. Omura, and I. Nagano (2009b), Coherent nonlinear scattering of energetic electrons in the process of whistler mode chorus generation, *J. Geophys. Res., 114*, A10205.

[43] Hubert, D. (1994), Nature and origin of wave modes in the dayside Earth magnetosheath, *Adv. Space Res., 14(7)*, 55.

[44] Hubert, D., C. Lacombe, C. C. Harvey, and M. Moncuquet, Nature properties and origin of low-frequency waves from an oblique shock to the inner magnetosheath, *J. Geophys. Res., 103*, 26,783.

[45] Inan, U. S., T. F. Bell, J. Bortnik, and J. M. Albert (2003), Controlled precipitation of radiation belt electrons, *J. Geophys. Res., 108(A5)*, 1186.

[46] Jordanova, V. K., J. Albert, and Y. Miyoshi (2008), Relativistic electron precipitation by EMIC waves from self-consistent global simulations, *J. Geophys. Res., 113*, A00A10.

[47] Joy, S. P., M. G. Kivelson, R. J. Walker, K. K. Khurana, C. T. Russell, and W. R. Paterson (2006), Mirror mode structures in the Jovian magnetosheath, *J. Geophys. Res., 111*, A12212.

[48] Kasper, J. C., A. J. Lazarus, and S. P. Gary (2002), Wind/SWE observations of firehose constraint on solar wind proton temperature anisotropy, *Geophys. Res. Lett., 29(17)*, 1839.

[49] Katoh, Y., and Y. Omura (2011), Amplitude dependence of frequency sweep rates of whistler mode chorus emissions, *J. Geophys. Res., 116*, A07201.

[50] Katoh, Y., and Y. Omura (2007), Computer simulation of chorus wave generation in the Earth's inner magnetosphere, *Geophys. Res. Lett., 34*, L03102.

[51] Kennel, C. F., and H. E. Petschek (1966), Limit of stably trapped particle fluxes, *J. Geophys. Res., 71*, 1.

[52] Kennel, C. F., F. Coroniti, J. Arons, R. Blandford, and M. Israel (1985), Perspectives on space and astrophysical plasma physics, *IAU SYMPOSIA*, 537.

[53] Kivelson, M. G., and D. J. Southwood (1996), Mirror instability II: The mechanism of nonlinear saturation, *J. Geophys. Res., 101(A8)*, 17,365.

[54] Lacombe, C., and G. Belmont (1995), Waves in the Earth's magnetosheath: observations and interpretations, *Adv. Space Res., 15(8/9)*, 329.

[55] Langmuir, I. (1928), Oscillations in ionized gases, *Proceedings of the National Academy of Sciences of the United States of America, 14*, 627.

[56] Lee, L., C. Price, C. Wu, and M. Mandt (1988), A Study of Mirror Waves Generated Downstream of a Quasi-Perpendicular Shock, *J. Geophys. Res., 93(A1)*, 247.

[57] Matsumoto, H., H. Kojima, T. Miyatake, Y. Omura, M. Okada, I. Nagano, and M. Tsutsui (1994), Electrostatic solitary waves (ESW) in the magnetotail: BEN wave forms observed by GEOTAIL, *Geophys. Res. Lett., 21 (25)*, 2915.

[58] Matsumoto, H., and Y. Omura (1993), Computer space plasma physics, *Terra Scientific Publishing Company*.

[59] Meredith, N. P., R. M. Thorne, R. B. Horne, D. Summers, B. J. Fraser, and R. R. Anderson (2003), Statistical analysis of relativistic electron energies for cyclotron resonance with EMIC waves observed on CRRES, *J. Geophys. Res., 108*, 1250.

[60] Midgeley, J. E., and L. Davis Jr. (1963), Calculation by a moment technique of the perturbation of the geomagnetic field by the solar wind, *J. Geophys. Res., 68*, 5111.

[61] Mursula, K., T. Braysy, K. Niskala, and C. T. Russell (2001), Pc1 pearls revisited: Structured electromagnetic ion cyclotron waves on Polar satellite and on the ground, *J. Geophys. Res., 106*, 29,543.

[62] Mursula, K., R. Rasinkangas, and T. Bosinger (1997), Nonbouncing Pc 1 wave bursts, *J. Geophys. Res., 102*, 17,611.

[63] Mursula, K., L. G. Blomberg, P. A. Lindqvist, G. T. Marklund, T. Braysy, R. Rasinkangas, and P. Tanskanen (1994), Dispersive Pc1 bursts observed by Freja, *Geophys. Res. Lett., 21*, 1851.

[64] Montbriand, L. E. (1971) The proton aurora and auroral substorm in *The Radiating Atmosphere*, edited by B. M. McCormac p. 366, D. Reidel, Dordrecht, Netherlands.

[65] Nunn, D., Y. Omura, H. Matsumoto, I. Nagano, and S. Yagitani (1997), The numerical simulation of VLF chorus and discrete emissions observed on the Geotail satellite using a Vlasov code, *J. Geophys. Res., 102(A12)*, 27083.

[66] Omura, Y., J. Pickett, B. Grison, O. Santolik, I. Dandouras, M. Engebretson, P. M. E Decreau, and A. Masson (2010), Theory and observation of electromagnetic ion cyclotron chorus emissions in the magnetosphere, *J. Geophys. Res., 115*, A07234.

[67] Omura, Y., M. Hikishima, Y. Katoh, D. Summers, and S. Yagitani (2009), Nonlinear mechanisms of lower-band and upper-band VLF chorus emissions in the magnetosphere, *J. Geophys. Res., 114*, A07217.

[68] Omura, Y., Y. Katoh, and D. Summers (2008), Theory and simulation of the generation of whistler-mode chorus, *J. Geophys. Res., 113*, A04223.

[69] Omura, Y. (1991), Comment on "Particle Simulation of Ion Heating in the Ring Current" by S. Qian, M. K. Hudson, and I. Roth, *J. Geophys. Res., 96*, 7929.

[70] Omura, Y., H. Usui, and H. Matsumoto (1988), Parallel heating associated with interaction of forward and backward electromagnetic cyclotron waves, *J. Geomag. Geoelectr., 40*, 949.

[71] Parker, E. N. (1958), Dynamics of the interplanetary gas and magnetic fields, *Astrophys. J., 128*, 664.

[72] Phan, T. D., G. Paschmann, W. Baumjohann, N. Sckopke, and H. Luhr (1994), The magnetosheath region adjacent to the dayside magnetopause: AMPTE/IRM observations, *J. Geophys. Res., 99*, 121.

[73] Pickett, J. S., B. Grison, Y. Omura, M. J. Engebretson, I. Dandouras, A. Masson, M. L. Adrian, O. Santolik, P. M. E. Decreau, N. Cornilleau-Wehrlin, and D. Constantinescu (2010), Cluster observations of EMIC triggered emissions in association with Pc1 waves near Earth's plasmapause, *Geophys. Res. Lett., 37*, L09104.

[74] Price, C. P., D. W. Swift, and L. C. Lee (1986), Numerical simulation of nonoscillatory mirror waves at the Earth's magnetosheath, *J. Geophys. Res., 91(A1)*, 101.

[75] Quest, K., and V. Shapiro (1996), Evolution of the fire-hose instability: Linear theory and wave-wave coupling, *J. Geophys. Res., 101(A11)*, 24457.

[76] Reme, H., et al. (2001), First multispacecraft ion measurements in and near the Earth's magnetosphere with the identical Cluster ion spectrometry (CIS) experiment, *Ann. Geophys., 19*, 1303.

[77] Roux, A., S. Perraut, J. Rauch, C. de Villedary, G. Kremser, A. Korth, and D. Young (1982), Wave-particle interactions near $\Omega_{He}$ observed on board GEOS 1 and 2: 2. Generation of ion cyclotron waves and heating of He+ ions, *J. Geophys. Res., 87*, 8174.

[78] Russell, C. T., P. Song, and R. P. Lepping (1989), The Uranian magnetopause: Lessons from Earth, *Geophys. Res. Lett., 16*, 1485.

[79] Sagdeev, R. Z., and A. A. Galeev (1969), Nonlinear Plasma Theory, *W. A. Benjamin, New York*, 8.

[80] Sagdeev, R. Z., and A. A. Vedenov (1959), About certain properties of plasma with the anisotropic velocity distribution in a magnetic field, in *Plasma Physics and the Problems of Controlled Thermonuclear Reactions, 3*, 32.

[81] Santolik, O., D. A. Gurnett, J. S. Pickett, M. Parrot, and N. Cornilleau-Wehrlin (2003), Spatio-temporal structure of storm-time chorus, *J. Geophys. Res., 108(A7)*, 1278.

[82] Sgro, A. G., and C. W. Nielson (1976), Hybrid model studies of ion dynamics and magnetic field diffusion during pinch implosions, *Phys. Fluids, 19*, 126.

[83] Shoji, M., Y. Omura, and L. C. Lee (2011a), Multi Dimensional Nonlinear Mirror-mode Structures in the Earth's Magnetosheath, *submitted to J. Geophys. Res.*

[84] Shoji, M., Y. Omura, B. Grison, J. Pickett, and I. Dandouras (2011b), Electromagnetic Ion Cyclotron Waves in Helium Branch Induced by Multiple Electromagnetic Ion Cyclotron Triggered Emissions, *Geophys. Res. Lett., 38*, L17102.

[85] Shoji, M., and Y. Omura (2011c), Simulation of electromagnetic ion cyclotron triggered emissions in the Earth's inner magnetosphere, *J. Geophys. Res., 116*, A05212.

[86] Shoji, M., Y. Omura, B. T. Tsurutani, O. P. Verkhoglyadova, and B. Lembege (2009), Mirror instability and L-mode electromagnetic ion cyclotron instability: Competition in the Earth's magnetosheath, *J. Geophys. Res., 114*, A10203.

[87] Soucek, J., E. Lucek, and I. Dandouras (2008), Properties of magnetosheath mirror modes observed by Cluster and their response to changes in plasma parameters, *J. Geophys. Res., 113*, A04203.

[88] Southwood D. J., and M. G. Kivelson (1993), Mirror Instability: 1. Physical Mechanism of Linear Instability, *J. Geophys. Res., 98*, 9181.

[89] Spasojevic, M., H. U. Frey, M. F. Thomsen, S. A. Fuselier, S. P. Gary, B. R. Sandel, and U. S. Inan (2004), The link between a detached subauroral proton arc and a plasmaspheric plume, *Geophys. Res. Lett., 31*, L04803.

[90] Stix, T. H. (1992), Waves in Plasmas, *American Institute of Physics.*

[91] Summers, D., B. Ni, and N. P. Meredith (2007), Timescales for radiation belt electron acceleration and loss due to resonant wave-particle interactions: 2. Evaluation for VLF chorus, ELF hiss, and electromagnetic ion cyclotron waves, *J. Geophys. Res., 112*, A04207.

[92] Summers, D., and R. M. Thorne (2003), Relativistic electron pitch-angle scattering by electromagnetic ion cyclotron waves during geomagnetic storms, *J. Geophys. Res., 108 (A4)*, 1143.

[93] Taflove, A. (1995), *Computational Electrodynamics: The Finite-DiRerence-Time-Domain Method*, Artech House, Norwood, MA.

[94] Tajima, T., and Y. C. Lee (1981), Absorbing boundary condition and Budden turning point technique for electromagnetic plasma simulation, *J. Comput. Phys 42*, 406.

[95] Tepley, L. R. (1961), Observations of hydromagnetic emissions, *J. Geophys. Res., 66*, 1651.

[96] Terasawa, T., and M. Hoshino (1986), Decay Instability of Finite-Amplitude Circularly Polarized Alfven Waves: A Numerical Simulation of Stimulated Brillouin Scattering, *J. Geophys. Res., 91*, 4171.

[97] Thorne, R. M. (2010), Radiation belt dynamics: The importance of wave-particle interactions, *Geophys. Res. Lett., 37*, L22107.

[98] Troitskaya, V. A. (1961), Pulsations of the earth's electromagnetic field with periods of 1 to 1.5 seconds and their connection with phenomena in the high atmosphere, *J. Geophys. Res., 66*, 5.

[99] Tsurutani, B. T., G. S. Lakhina, O. P. Verkhoglyadova, E. Echer, F. L. Guarnieri, Y. Narita, and D. O. Constantinescu (2011), Magnetosheath and heliosheath mirror mode structures, interplanetary magnetic decreases, and linear magnetic decreases: Differences and distinguishing features, *J. Geophys. Res., 116*, A02103.

[100] Tsurutani, B. T., G. S. Lakhina, E. J. Smith, B. Buti, S. L. Moses, F. V. Coroniti, A. L. Brinca, J. A. Slavin, and R. D. Zwickl (1999), Mirror mode structures and ELF plasma waves in the Giacobini-Zinner magnetosheath, *Nonl. Proc. Geophys., 6*, 229.

[101] Tsurutani, B. T., D. J. Southwood, E. J. Smith, and A. Balogh (1993), A survey of low-frequency (LF) waves at Jupiter: The Ulysses encounter, *J. Geophys. Res., 98*, 21,203.

[102] Tsurutani, B. T., D. J. Southwood, E. J. Smith, and A. Balogh (1992), Nonlinear magnetosonic waves and mirror mode structures in the March 1991 Ulysses interplanetary event, *Geophys. Res. Lett., 19*, 1267.

[103] Tsurutani, B. T., I. G. Richaradson, R. P. Lepping, R. D. Zwickl, D. E. Jones, E. J. Smith, and S. J. Bame (1984), Drift mirror mode waves in the distant (x $\sim$ 200 RE) magnetosheath, *J. Geophys. Res., 11*, 11,102.

[104] Tsurutani, B. T., E. J. Smith, R. R. Anderson, K. W. Ogilvie, J. D. Scudder, D. N. Baker, and S. J. Bame (1982), Lion roars and nonoscillatory drift mirror waves in the magnetosheath, *J. Geophys. Res., 87*, 6060.

[105] Tsurutani, B. T., and P. Rodriguez (1981), Upstream Waves and Particles: An Overview of ISEE Results, *J. Geophys. Res., 86(A6)*, 4317.

[106] Umeda, T. (2008), A conservative and non-oscillatory scheme for Vlasov code simulations, *Earth, Planets and Space, 60*, 773.

[107] Umeda, T., Y. Omura, and H. Matsumoto (2001), An improved masking method for absorbing boundaries in electromagnetic particle simulations, *Comput. Phys. Commun., 137*, 286.

[108] Violante, L., B. Cattaneo, G. Moreno, and J. D. Richardson (1995), Observations of mirror mode and plasma depletion layer upstream of Saturn's magnetopause, *J. Geophys. Res., 100*, 12,047.

[109] Wilcox, J. M., and N. F. Ness (1965), Quasi-stationary corotating structure in the interpranetary medium, *J. Geophys. Res., 70*, 5793.

[110] Winske, D., and M. M. Leroy (1984), Diffuse Ions Produced by Electromagnetic Ion Beam Instabilities, *J. Geophys. Res., 89*, 2673.

[111] Winterhalter, D., M. Neugebauer, B. Goldstein, E. Smith, S. Bame, and A. Balogh (1994), Ulysses Field and Plasma Observations of Magnetic Holes in the Solar Wind and their Relation to Mirror-Mode Structures, *J. Geophys. Res., 99(A12)*, 23371.

[112] Xiao, F., Q. Zhou, H. He, H. Zheng, and S. Wang (2007), Electromagnetic ion cyclotron waves instability threshold condition of suprathermal protons by kappa distribution, *J. Geophys. Res., 112*, A07219.

[113] Yabe, T. F. Xiao, and T. Utsumi (2001), The constrained interpolation profile method for multiphase analysis, *J. Comput. Phys., 169*, 556.

[114] Yoon, P. H. (1990), Electromagnetic fire-hose instability in a fully relativistic bi-maxwellian plasma, *Phys. Fluids (B), 2*, 842.

[115] Zhang, T. L. et al. (2009), Mirror mode structures in the solar wind at 0.72 AU, *J. Geophys. Res., 114*, A10107.

[116] Zwan, B. J., and R. A. Wolf (1976), Depletion of the solar wind plasma near a planetary boundary, *J. Geophys. Res., 81*, 1636.

# Publication List

## Major Publications

1. <u>Shoji, M.</u>, Y. Omura, B. T. Tsurutani, O. P. Verkhoglyadova, and B. Lembege, Mirror Instability and L-mode Electromagnetic Ion Cyclotron Instability: Competition in the Earth's Magnetosheath, *J. Geophys. Res.*, *114*, A10203., 2009.

2. <u>Shoji, M.</u>, and Y. Omura, Simulation of Electromagnetic Ion Cyclotron Triggered Emissions in the Inner Magnetosphere, *J. Geophys. Res.*, *116*, A05212., 2011.

3. <u>Shoji, M.</u>, Y. Omura, B. Grison, J. Pickett, and I. Dandouras, Electromagnetic Ion Cyclotron Waves in Helium Branch Induced by Multiple Electromagnetic Ion Cyclotron Triggered Emissions, *Geophys. Res. Lett.*, *38*, L17102., 2011.

4. <u>Shoji, M.</u>, Y. Omura, and L. C. Lee, Multi Dimensional Nonlinear Mirror-mode Structures in the Earth's Magnetosheath, *submitted to J. Geophys. Res.*

5. <u>Shoji, M.</u>, and Y. Omura, Precipitation of Highly Energetic Protons by Helium Branch Electromagnetic Ion Cyclotron Triggered Emissions, *to be submitted.*

## Refereed Symposium Proceeding

1. <u>Shoji, M.</u>, and Y. Omura, Pitch Angle Scattering by Electromagnetic Ion Cyclotron Triggered Emissions in the Inner Magnetosphere: Hybrid Simulations, *XXXth URSI General Assembly and Scientific Symposium (GASS)*, accepted for publication, 2011.

## Presentations in International Meetings

1. <u>Shoji, M.</u>, Y. Omura, and L. C. Lee, Nonlinear Mirror Mode Structures in Multi-dimensional Models, *URSI General Assembly and Scientific Symposium*, Istanbul., Aug. 2011, (*INVITED*).

2. <u>Shoji, M.</u>, and Y. Omura, Mirror-mode Structures in the Magnetosheath : 3D Hybrid Results, *Asia Oceania Geosciences Society Annual Meeting*, India., Aug. 2010, (*INVITED*).

3. Shoji, M., and Y. Omura, Nonlinear Evolutions of the Mirror-mode and the L-mode Electromagnetic Ion Cyclotron Instabilities, *Asia Oceania Geosciences Society Annual Meeting*, Singapore., Aug. 2009, (*INVITED*).

4. Shoji, M., and Y. Omura, Simulation of Electromagnetic Ion Cyclotron Triggered Emissions in the Inner Earth's Magnetosphere, *International Symposium of Japan Geoscience Union*, Japan., May. 2011.

5. Shoji, M., and Y. Omura, Electromagnetic Ion Cyclotron Triggered Emissions in a Dipole Geometry: Hybrid Simulation Results, *AP-RASC*, Japan., Sep. 2010.

6. Shoji, M., Y. Omura, B. T. Tsurutani, O. P. Verkhoglyadova, and B. Lembege, Competition Between the Mirror-Mode Instability and the L-Mode Electromagnetic Ion Cyclotron Instability: Results from Comparison of 2-D and 3-D Simulations, *URSI General Assembly*, America., Aug. 2008.

7. Shoji, M., Y. Omura, B. T. Tsurutani, O. P. Verkhoglyadova, and B. Lembege, Competition Between the Mirror-Mode Instability and the L-Mode Electromagnetic Ion Cyclotron Instability, *International Symposium of Japan Geoscience Union*, Japan., May. 2008.

8. Shoji, M., Y. Omura, B. Grison, J. Pickett, and I. Dandouras, Electromagnetic Ion Cyclotron Waves in Helium Branch Induced by Multiple Electromagnetic Ion Cyclotron Triggered Emissions, *American Geophysical Union Fall meeting*, America., Dec. 2011.

9. Shoji, M., Y. Omura, and L. C. Lee, Nonlinear Mirror Mode Structures in the magnetosheath: Two- and Three- dimensional Hybrid Simulations, *American Geophysical Union Fall meeting*, America., Dec. 2010.

10. Shoji, M., and Y. Omura, Hybrid simulations of electromagnetic ion cyclotron triggered emissions in a dipole geometry, *COSPAR*, Germany., Jul. 2010.

11. Shoji, M., and Y. Omura, Three-Dimensional Mirror Mode Structures: Comparison with the Magnetic Peaks and Decreases, *American Geophysical Union Fall meeting*, America., Dec. 2009.

12. Shoji, M., and Y. Omura, Coalescence of Mirror Mode Structures: Nonlinear Particle Motion in the Magnetic Structures, *The 9th International School for Space Simulations*, France., Jul. 2009.

13. Shoji, M., Y. Omura, B. T. Tsurutani, O. P. Verkhoglyadova, and B. Lembege, Mirror-Mode Instability versus L-Mode Electromagnetic Ion Cyclotron Instability: Comparison of 2-D and 3-D Simulations, *American Geophysical Union Fall meeting*, America., Dec. 2008.

14. Shoji, M., Y. Omura, B. T. Tsurutani, and O. P. Verkhoglyadova, Competition Between the Mirror- and L-mode Electromagnetic Ion Cyclotron Instabilities in the

Earth's Magnetosheath: Comparison Between 2-D and 3-D Simulations, *American Geophysical Union Fall meeting*, America., Dec. 2007.

# Awards

1. URSI Young Scientist Award, Pitch Angle Scattering by Electromagnetic Ion Cyclotron Triggered Emissions in the Inner Magnetosphere: Hybrid Simulations, *XXXth URSI General Assembly*, 2011.

2. Best Poster Award, 1st prize, Coalescence of Mirror Mode Structures: Nonlinear Particle Motion in the Magnetic Structures, *The 9th International School for Space Simulations*, 2009.

3. SGEPSS Student Presentation Award (Aurora Medal), Competition between the mirror instability and the L-mode electromagnetic ion cyclotron instability (in Japanese), *124th Society of Geomagnetism and Earth, Planetary and Space Sciences (SGEPSS) Fall Meeting*, 2008.